공학박사학위논문

# Engineering Design of High-Efficiency Multi-Purpose Nuclear Electric Power Systems

고효율 다목적 원자력전동기
계통 공학 설계

2013년 2월

서울대학교 대학원

에너지시스템공학부

버 하 누 딘

# Engineering Design of High-Efficiency Multi-Purpose Nuclear Electric Power Systems

# 고효율 다목적 원자력전동기 계통 공학 설계

지도교수  서 균 렬

이 논문을 공학박사학위 논문으로 제출함

2012년 10월

서 울 대 학 교 대 학 원
에 너 지 시 스 템 공 학 부
버 하 누 딘

버하누딘의 박사학위 논문을 인준함

2012년 12월

위 원 장 ____심 형 진____(인)

부위원장 ____서 균 렬____(인)

위　　원 ____김 응 수____(인)

위　　원 ____배 윤 영____(인)

위　　원 ____차 재 은____(인)

# ABSTRACT

# Engineering Design of High-Efficiency Multi-Purpose Nuclear Electric Power Systems

**Burhanuddin Halimi**

School of Energy Systems Engineering

Seoul National University

This research focuses on analysis of power conversion system Modular Optimal Brayton Island System (MOBIS) for versatile purposes. The system adopts a supercritical $CO_2$ (S-$CO_2$) as working fluid to get benefit in term of thermal efficiency from its thermodynamic property characteristics. Design of MOBIS is basically based on Battery Omnibus Reactor Initiative System (BORIS) being developed at the Seoul National University as a multipurpose integral fast reactor, as the powering reactor. In addition to key components such as heat exchangers and turbomachinery, the piping system is taken into account to obtain more reasonable result in this study. Without taking any turbine valves into analysis consideration, a thermal efficiency of 42.50% can be attained.

Moreover, due to its imperative role on regulating output power, the turbine valve is further studied as well to improve the system performance. Unfortunately,

however, the valve has inherently nonlinearity characteristic. First of all, a combined stop valve and control valve is introduced to replace the roles of the conventional separated one. The combined valve flow coefficient data were newly generated by the Combined Airflow Regulation Analysis (CARA) and Combined Airflow Regulation Operation (CARO) experiment. Based on the CARA/CARO outcome, the cycle efficiencies were investigated for both the $S\text{-}CO_2$ recompressing Brayton cycle and common steam turbine system as well. By adopting the combined valve, the thermal efficiency can be improved by 0.43% and 1.27% in $S\text{-}CO_2$ recompressing Brayton cycle and steam turbine system, respectively. The improvement will be much more significant in the higher power applications.

Engineering analysis is also made of the compensation of nonlinear valve characteristic. As a standard analysis code in nuclear engineering, the MARS code is utilized for the analysis to obtain more accurate results from the thermalhydraulic point of view without sacrificing the control engineering aspects. Various scenarios are analyzed to show the effectiveness of nonlinearity characteristic compensation mechanism to improve the performance of power conversion system and its applications as well.

Last, but not least, the concept of analyzed power conversion system is applied to a typical fusion reactor and a marine propulsion system to explore other applications of the $S\text{-}CO_2$ power conversion system. The DEMO model AB is selected as the reference fusion reactor. The computational analysis of this case gives a thermal efficiency of 42.44%. By adding a reheating layout, its efficiency can be enhanced to 43.1%.

Engineering design of Naval Applied Vessel Island System (NAVIS) is briefly discussed as an example of the next generation concept of marine nuclear propulsion system. NAVIS is designed to suit the requirement of a compact, simple, safe and innovative integral fast reactor system. It is mainly powered by BORIS.

To allow for significant size reduction and efficiency improvement, NAVIS adopted MOBIS and Nuclear Electric Propulsion Apparatus (NEPA) for its power conversion and propulsion system, respectively.

Keywords: Power Conversion System, Supercritical $CO_2$, Combined Valve, Nonlinearity Characteristic Compensation, Fusion Reactor, Marine Propulsion System

Dedicated:

To my beloved parents who passed away before I reward them with my best.

To my lovely wife 'Elin Julianti' and my greatest and

most beneficial blessing 'Adelia and Rafie'

"My Lord! Forgive me and my parents, have mercy upon them, as they raised me up (when I was) little. Our Lord! Grant unto us wives and offspring who will be the comfort of our eyes, and give us (the grace) to lead the righteous."

# ACKNOWLEDMENTS

Last, but not least, I would like to thank my family in Indonesia, my parents in law, my sisters and brothers, for their pray and loving support for successfully finishing my study.

# CONTENTS

viii

# LIST OF TABLES

# LIST OF FIGURES

# 1. INTRODUCTION

## 1.1. Background

A number of investigations have recently been carried out on a variety of power conversion system (PCS) for the next generation power generation plants (Johnson, 2011). Studies on PCS will examine some basic questions such as type of PCS (Rankine or Brayton cycle), how it should be coupled to the reactor (direct or indirect method), and what kind of working fluid will be utilized etc.

The development effort of Generation IV (Gen IV) reactor aims to replace the current Gen III reactors with highly economical aspect, enhanced safety, minimal waste and also proliferation resistance as main considerations. The Gen IV reactor concepts mostly have higher operating temperatures than the current reactors. Thus it is possible to attain a higher thermal efficiency for Gen IV reactors as their distinguishing feature (Trinh, 2009).

In the PCS point of view, one prospective PCS for Gen IV reactor is Supercritical $CO_2$ (S-$CO_2$) Brayton cycle. This cycle takes the great benefit of $CO_2$ physical properties change near its critical point (304.13K, 7.38 MPa) to increase the thermal efficiency. In this region, the properties of $CO_2$ change significantly as illustrated in Figure 1-1 through 1-5. Figure 1-2 through 1-5 describe the heat transfer capacity, density, enthalpy an viscosity of $CO_2$ for various pressure values, respectively. As shown in Figure 1-3, the fluid has a high density near its critical point, which results in an advantage of compressor work reduction.
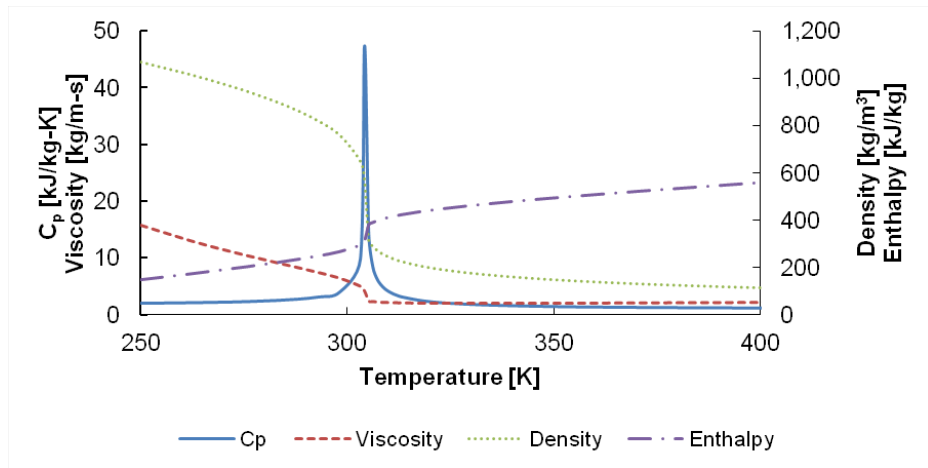
**Figure 1-1. Properties change around the critical point**
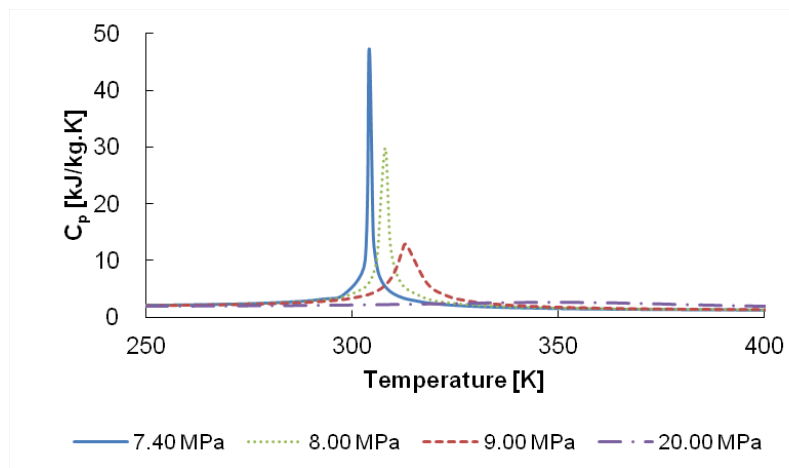


**Figure 1-2. Heat transfer capacity**
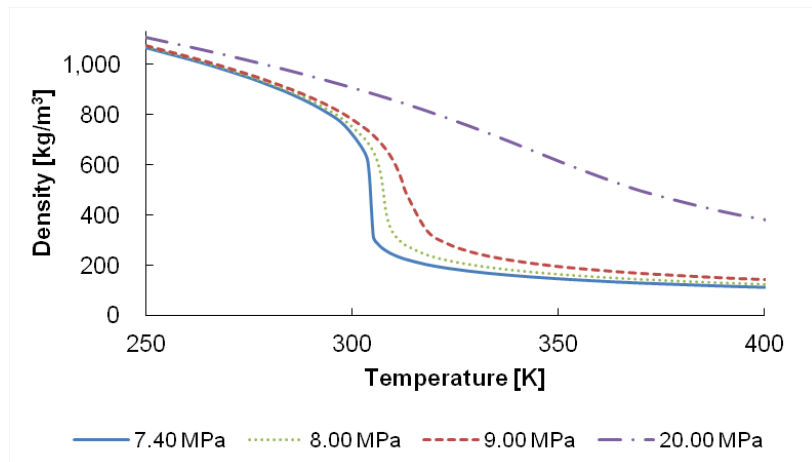
**Figure 1-3. Density**
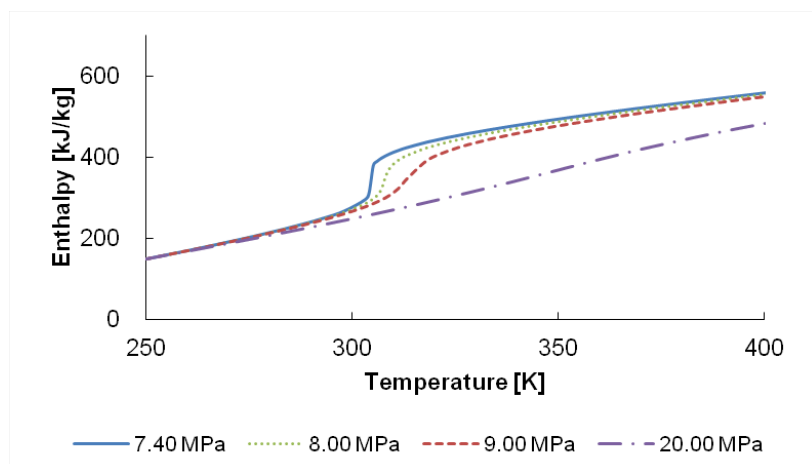


**Figure 1-4. Enthalpy**

3
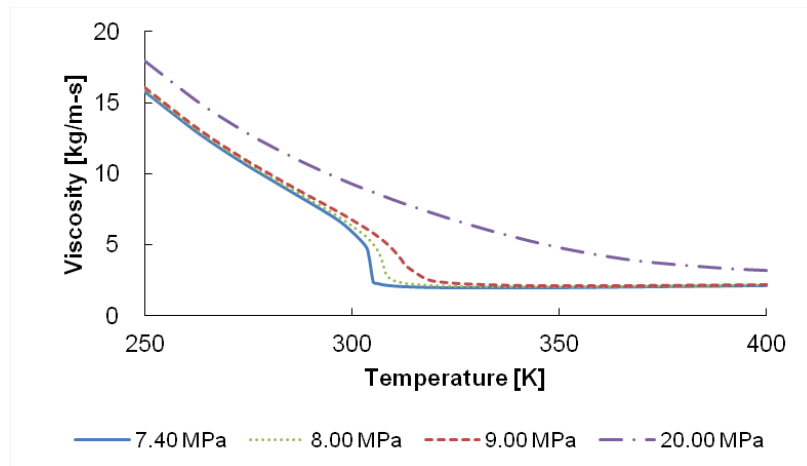
**Figure 1-5. Viscosity**

## 1.2. State of the Art

### 1.2.1. Rankine and Brayton Cycles

The Rankine cycle such as supercritical water power generation has well-documented the history of performance from coal-fired plant, while the Brayton cycle options were not sufficiently mature (Holcomb et al., 2011). But in the previous studies, it was found that the Brayton cycle is very promising and warrants further development especially in higher temperature operations (Johnson, 2011). As the next generation nuclear reactors are designed for high temperature operation capability, many researchers have been working seriously to look deeper into the Brayton cycle for future nuclear reactor. Figure 1-6 summarizes the comparison of Rankine and Brayton cycles in term of efficiency based on previous studies (Dostal et al., 2006b; Johnson, 2011). This summary illustrates the superiority of the Brayton cycle to the Rankine cycle in high temperature operation. Also, note that $S\text{-}CO_2$ can be operated at much lower turbine inlet temperatures than in the helium cycle to obtain the same efficiency.

4
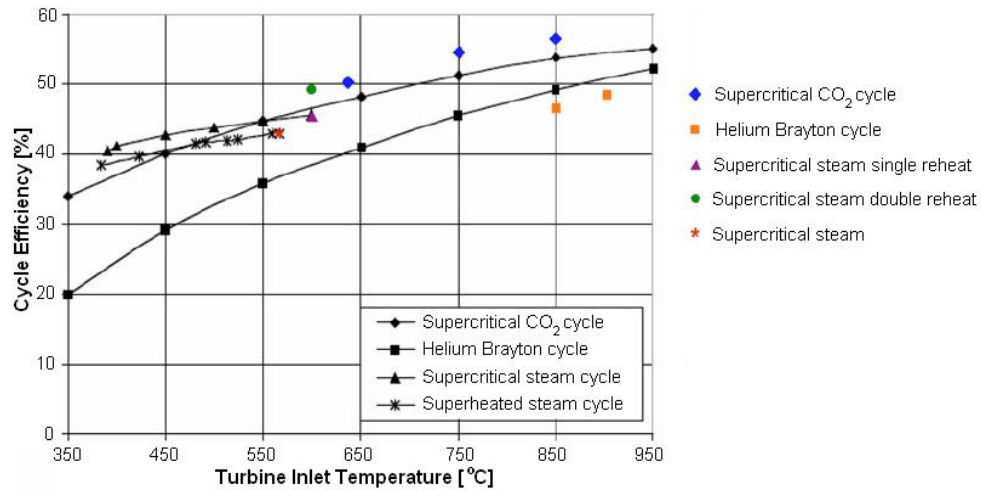
**Figure 1-6. Cycle performance**

### 1.2.2. Helium and Supercritical CO$_2$ (S-CO$_2$)

As a PCS working fluid of the Brayton cycle, helium and S-CO$_2$ became the most attractive subject of investigation for many researchers. Helium is a well-understood fluid and has been adopted in the numerous studies pertaining to the high temperature reactors. Compared to helium, S-CO$_2$ does possess some advantages such as a higher density, allowing smaller velocity for the same pressure drop and smaller volumetric flow rates for generating equivalent power (Oh et al., 2006). Also, by adopting the S-CO$_2$ Brayton cycle, extra major benefits can be obtained such as (1) high thermal efficiency (2) compactness of the turbomachineries and heat exchangers and (3) simpler cycle layout (Yoon et al., 2012).

Oh (2005) investigated the efficiency of helium Brayton cycle for the power conversion side of high-temperature gas-cooled reactor (HTGR) power plant. The reference case based on the 250 MWt pebble bed HTGR was developed using

helium as a working fluid in both the primary and power conversion sides.

As illustrated in the previous sub-chapter, the comparison of helium and S-$CO_2$ Brayton cycle was investigated by Dostal et al. (2006b). The results showed that the S-$CO_2$ recompressing Brayton cycle is well suited to any types of nuclear reactors with outlet temperature above ~773.15 K and offers an extra potential cost reduction when compared to helium Brayton cycle. Also this cycle was recommended to be considered as power cycle of future reactors.

### 1.2.3. Direct and Indirect Cycles

In a direct Brayton cycle, the working fluid is circulated through the reactor core for picking up the heat and expanding through turbine to the produce output power (Johnson, 2011). This cycle has achieved quite a mature state and its typical cycle layout is illustrated in Figure 1-7 (Dostal et al., 2006b). The cycle has one intercooler and two compressors. In term of electricity production, the direct cycle is the most efficient cycle (Dostal et al., 2006b). It has no additional losses from the circulating primary coolant. Also there are no temperature differences between the primary and secondary working fluids. These attractive features have been considered for designing power conversion system concept for next generation reactors (Bentivoglio et al., 2008; Koster et al., 2003). The main concern of a direct Brayton cycle directly coupled to reactor is radioactive contamination throughout the power conversion system. It will make significant difficulties especially when the power conversion system has to be opened for maintenance purposes (Johnson, 2011).
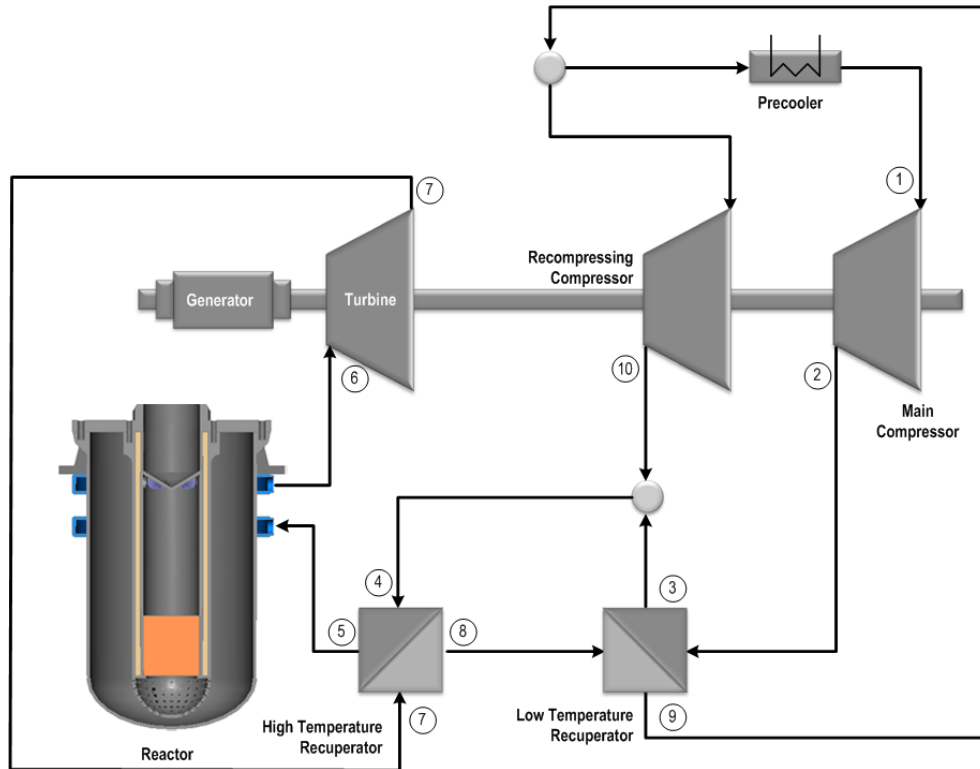
**Figure 1-7. Typical direct Brayton cycle layout**

The indirect Brayton cycle is basically like the direct one (Johnson, 2011). But in this cycle, the working fluid that circulated through reactor is sent to an intermediate heat exchanger (IHX) where the thermal energy is then transferred to the power conversion system as illustrated in Figure 1-8. Although the gas cooled fast reactor (GFR) with direct helium Brayton cycle is considered as reference design for Gen IV due to its simplicity and high efficiency, various investigation on indirect cycle are highly interesting for many researchers recently (Hejzlar et al., 2006a; Moisseytsev and Sienicki, 2008; Seong et al., 2009). Also, due to its physically independent secondary system to reactor and primary system, the overall plant safety of indirect cycle can be improved and the radiological issues

can be minimized as well (Dostal et al., 2006b).
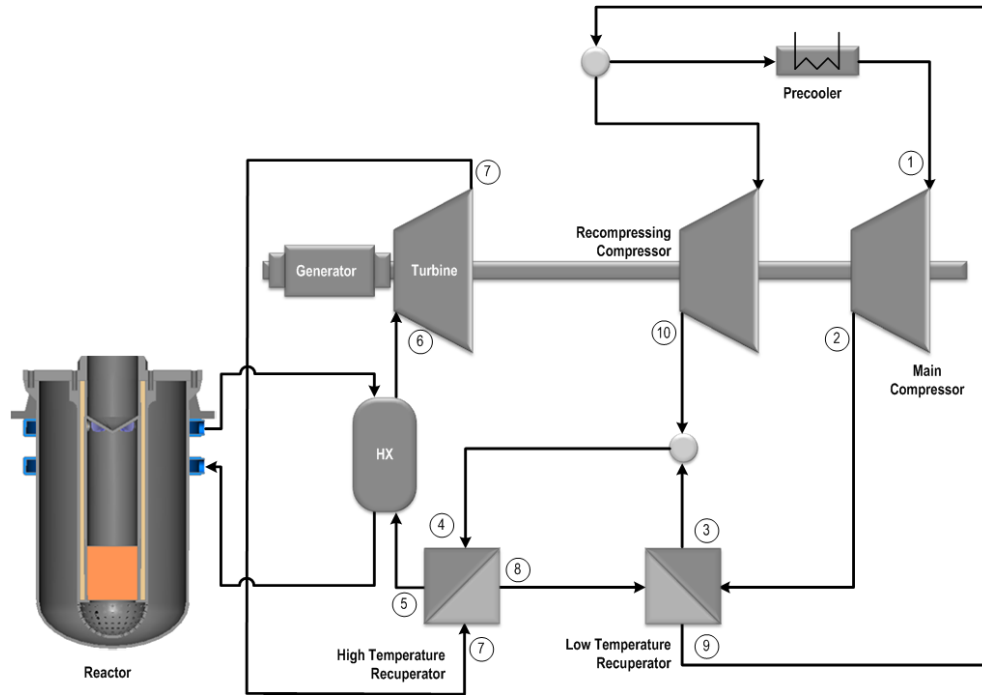


**Figure 1-8. Typical indirect Brayton cycle layout**

### 1.2.4. Fusion Reactor and Renewable Energy Power Source

The feasibility of S-CO$_2$ PCS was also studied for another kind of power sources, such as fusion reactor (Ishiyama et al., 2008; Linares et al., 2011; Medrano et al., 2007; Wu, 2008) or renewable energy resource such as solar energy (Yamaguchi et al., 2006; Zhang et al., 2006). The studies looked into advanced thermodynamic cycles to improve the thermal efficiency of power conversion. One of the prospective cycles is the S-CO$_2$ Brayton cycle. This cycle adopts an energy converter consisting of a gas turbine Brayton cycle using S-CO$_2$ as working fluid providing significantly enhanced cycle efficiencies at low temperatures relative to the conventional Rankine steam cycle. In this power conversion system, the

electric output of the generator is proportional to the flow rate of high pressure gas produced from the divertor and blanket heat exchanger.

In China the fusion design study (FDS) team has been developing the fusion power reactor FDS-II as one of the series of fusion system design concept (Wu, 2008). A direct helium Brayton cycle was selected for its He/LiPb dual-cooled lithium lead (DLL) blanket power conversion system with a maximum gas temperature of 953 K. Ishiyama et al. (2008) did a study on steam, helium and S-$CO_2$ turbine power generation systems for a prototype fusion power. The temperatures of blanket fluid and secondary coolant were assumed as 783 K and 753 K, respectively. The S-$CO_2$ turbine cycle ended up the most prospective system for the fusion reactor in terms of efficiency. Linaresa et al. (2011) investigated the He-Brayton and $CO_2$-Feher cycle for fusion energy source application. The plain configuration Feher cycle resulted in slightly better efficiency of 41% compared to the He-Brayton cycles with 40.8% of thermal efficiency aided by rather more complex layout of a dual cycles. To improve the thermal efficiency, several advanced power conversion cycles have also been studied in the framework of the demonstration fusion power plant (DEMO) scoping studies by Medrano et al. (2007). The ultimate goal of DEMO is to demonstrate the electricity production feasibility based on fusion power.

An extended direct Brayton cycle layout was considered for fusion DEMO power plant by Wong et al. (1995). The cycle adopted three-stage compressor with two intercoolers instead of two-stage compressor with one intercooler to maintain the high helium pressure as shown in Figure 1-9. The blanket coolant was coupled to this cycle for its power production. At helium outlet maximum temperature of 650 $^{\circ}$C, maximum pressure 18 MPa and effective recuperator of 96%, the gross efficiency of the fusion demo plant was claimed as 46%. This efficiency is same as an advanced Rankine cycle employing two steam reheaters to 565 $^{\circ}$C and pressure of 31 MPa (Malang et al., 1998). A similar direct helium Brayton cycle power

conversion system with a maximum gas temperature of 680 °C, which has a gross efficiency of about 47%, was selected for the He/LiPb Dual-cooled Lithium Lead (DLL) breeder blanket of the fusion power reactor (FDS-II) (Wu, 2008).
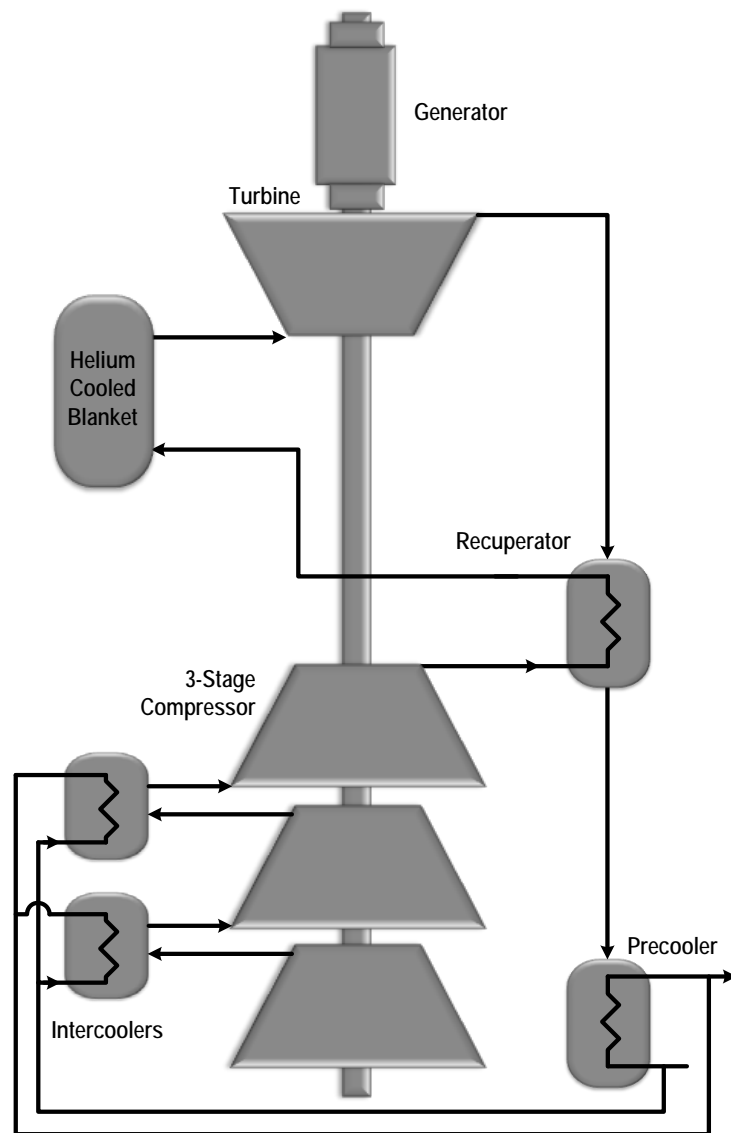


**Figure 1-9. Fusion DEMO plant direct He Brayton cycle**

For solar energy application, Zhang et al. (2006) adopted $CO_2$ system based on Rankine cycle. The system consists of an solar collector system, a turbine, high and low grade heat recovery systems and a feed pump as shown in Figure 1-10. The heat power efficiency was 36.2% (Zhang et al., 2006).

A different PCS was proposed by US National Renewable Energy Laboratory (Ma and Turchi, 2011; Turchi, 2009). The design used $S\text{-}CO_2$ as both heat transfer fluid (HTF) and thermal power cycle to simplify the power system configuration as depicted in Figure 1-11. Also it was designed to be compatible with sensible-heat thermal energy storage.
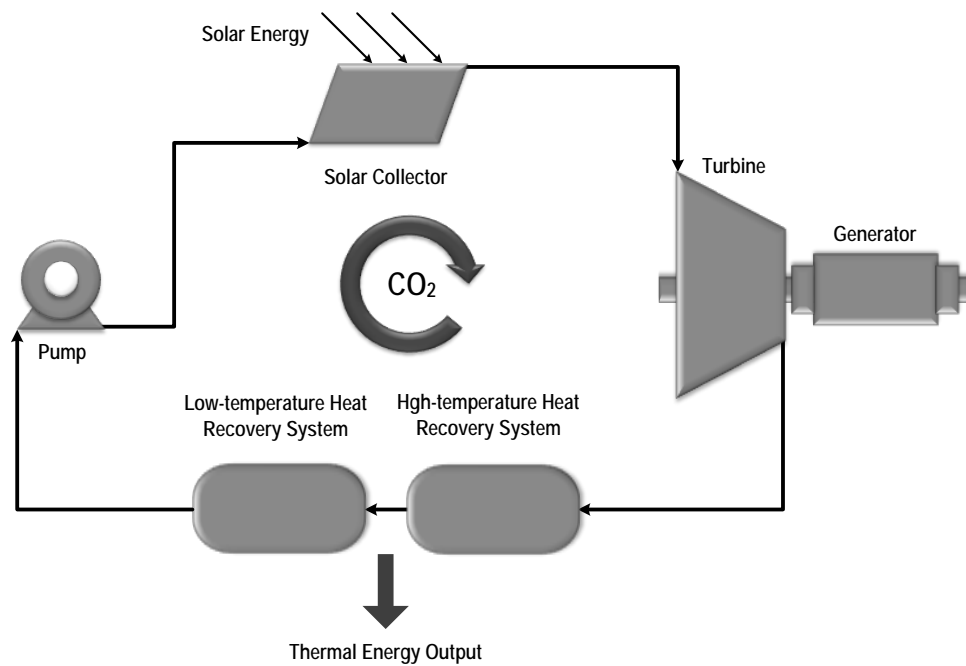


**Figure 1-10. $CO_2$ based Rankine cycle for solar energy application**
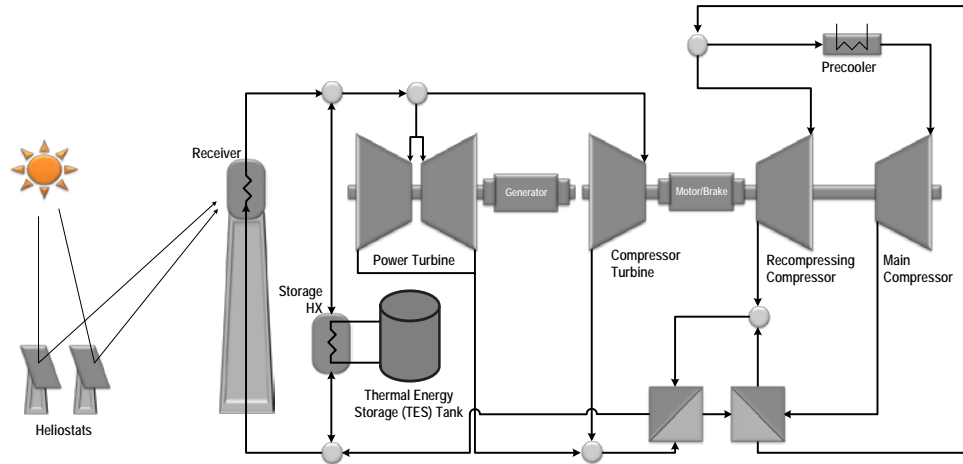
**Figure 1-11. Dual-shaft S-CO$_2$ Brayton cycle solar thermal power system**

### 1.2.5. High vs. Small Power Reactors

The high power density and compactness benefits of S-CO$_2$ PCS have attracted many researchers to look more detail into the feasibility and design of S-CO$_2$ PCS for wider output power capacity, from thousands to less than hundreds of MWe power output. Table 1-1 summarizes the researches on S-CO$_2$ Brayton cycle which designed to be coupled with nuclear reactors. (Chang et al., 2007; Maisonnier et al., 2007; Medrano et al., 2007; Seong et al., 2009; Son and Suh, 2011).

**Table 1-1. Researches on S-CO$_2$ PCS**

| Reactor | Power [MWe] |
|---|---|
| DEMO (fusion reactor) | ~1,500 |
| KALIMER | ~600 |
| STAR-LM | ~175 |
| SMFR | ~50 |
| BORIS | ~10 |

**1.2.6. Brayton Cycle for Marine Propulsion System**

Majority of studies on Brayton cycle coupled to nuclear reactor are for power generation application. There were only a few literatures focused on Brayton power conversion system for marine application. Moreover, most of nuclear propulsion systems still relied on the mature Rankine cycle instead of gas Brayton cycle. Albeit the Brayton cycle is still not mature yet, this cycle was recommended as one alternative for design of marine nuclear power plant (Gathy, 1967).

Considering hybrid technology features in marine applications, the economic viability of a hybrid gas turbine modular helium reactor (GT-MH) was anticipated for FastShip propulsion system (Vergara and McKesson, 2002). This hybrid option was preferred considering the large power difference between cruising and maximum speed. Also it would gain additional benefits i.e. better investment to operation cost balance and power source redundancy.

Chen et al. (2003) investigated a simple closed Brayton cycle with helium as working fluid for submarine propulsion system. In this study, the maximum power, power density and efficiency were obtained based on the optimum heat conductance distribution among the heat exchangers (intermediate heat exchanger, precooler, and recuperator). The cycle adopted a indirect cycle. The maximum thermal efficiency is about 43%.

## 1.3. Objectives and Contribution

The main objective of this research is to investigate the high efficiency power conversion system for multipurpose by adopting S-$CO_2$ as working fluid. The multipurpose terminology is adopted to represent that the outcomes should be also applicable to any other types of power heat sources and also any other characteristic connected-loads. To enhance the thermal efficiency, a study on

combined control valve to replace the conventional combination stop valve and control valve is performed. Moreover, to improve the cycle performance, a compensation of valve nonlinearity characteristic is further investigated as well.

The major contributions of this work are listed below:

1. Improving the analysis code for S-$CO_2$ Brayton cycle by considering pressure drop of piping system. Using the upgraded code, a conceptual design of power conversion systems for small modular reactor BORIS is analyzed. Also, the design concept is applied to fusion reactor DEMO and an electric nuclear propulsion system to explore other application of analyzed design.

2. Introducing combined valve for improving the efficiency of power conversion system. Because there is no available combined valve flow coefficient data, the flow coefficient data is newly generated by computational analysis and experimental procedure, as well, base on the self manufactured combined valve. Using the obtained data, an application of combined valve was analyzed for a typical turbine system to show the benefit of this combined valve compared to the conventional stop and control valve. Moreover, the analysis was not limited only for common working fluid such as air or steam, but S-$CO_2$ is also considered as working fluid as well. Especially for the S-$CO_2$ Recompressing Brayton cycle, this approach is a new method to improve the thermal efficiency.

3. Analyzing control valve nonlinearity characteristic compensation to enhance the cycle performance. By adopting the compensation mechanism, the control system can be designed much easier because the nonlinearity was eliminated by the compensator. Then, as a standard

analysis code in nuclear engineering, the MARS code is utilized for the analysis of the valve nonlinearity characteristic compensation to obtain a more accurate results in the thermalhydraulic point of view without sacrificing control engineering aspects.

## 1.4. Thesis Organization

This thesis is organized into six chapters and four appendices as follows:

Chapter 1 presents briefly research background and state of the art. The objectives and main contribution of this research are provided in this chapter as well.

Chapter 2 focuses on introduction on power conversion system and power conversion system design, including the computational analysis code and discussion on key components of the system.

Chapter 3 discusses combined valve to replace the common combination of stop valve and control valve to improve thermal efficiency of the power conversion system. To show the effectiveness of utilizing the combined valve, computational studies of both Rankine cycle and also Brayton cycle are provided in this chapter.

Chapter 4 explores the compensation method of control valve nonlinearity characteristic to improve the power conversion system performance. Various cases are analyzed to make easier for understanding the concept. An experimental result is provided to validate to concept as well.

Chapter 5 briefly looks at the applications of the power conversion system in other applications, especially for fusion reactor and marine propulsion applications. The DEMO model AB is selected as the reference of fusion

reactor. Also, NAVIS which adopts BORIS, MOBIS and also NEPA is shortly discussed as an example of the next generation concept of marine nuclear propulsion system.

Chapter 6 summarizes this work and make recommendations for future work.

Three appendices are provided as additional information and/or data to the main chapters.

# 2. POWER CONVERSION SYSTEM

## 2.1. Introduction

Currently, the Battery Omnibus Reactor Integral System (BORIS) is being developed at Seoul National University as a multipurpose integral fast reactor for such application as power generation, marine propulsion system, hydrogen production etc. BORIS is designed to meet Gen IV reactor objectives in term of safety, sustainability, reliability and economy (Son and Suh, 2011). BORIS reactor assembly has six heat exchangers as illustrated in Figure 2-1 (Son and Suh, 2011). The interim results of BORIS primary system design is depicted in Table 2-1 (Son et al., 2011).
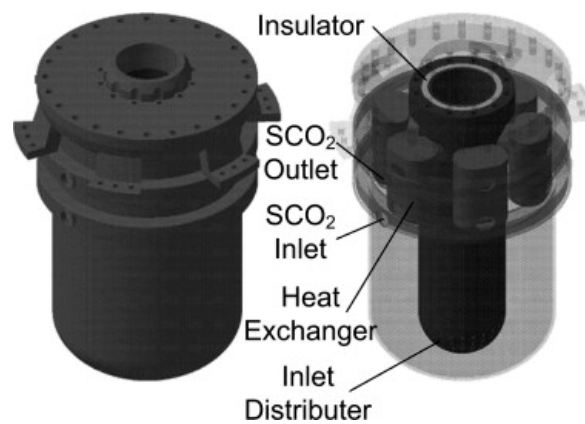


**Figure 2-1. BORIS reactor vessel assembly**

17

**Table 2-1. Specification of BORIS primary system**

| | |
|---|---|
| Thermal/electric power [MW] | ~23.5/10 |
| Thermal efficiency [%] | 43.46 |
| Core diameter [m] | 1.0124 |
| Active core height [m] | 0.9351 |
| Fuel pin pitch-to-diameter | 1.15 |
| Number of fuel pins | 1,285 |
| Fuel pin diameter [m] | 0.0175 |
| Primary mass flow rate [kg/s] | 1397.09 |
| Temperature difference [K] | 111.55 |
| Thermal center difference [m] | 2.28 |
| Fuel Cost Ratio ($C_{ir}/C_{dr}$) | 9.540e6 |
| Decay ratio | 0.9966 |

The BORIS is designed to be coupled with the Modular Optimal Balance Integral System (MOBIS) as its power conversion system. The MOBIS development effort aims to design a small and efficient power conversion system which can produce 10 MWe output power (Jeong, 2010). For MOBIS analysis, the Optimized Supercritical Cycle Analysis (OSCA) is also being developed. The OSCA code provides a model for simulating the $S-CO_2$ Brayton cycle to obtain the optimal condition for power conversion system operation. The recompression $S-CO_2$ Brayton cycle is selected as the main power conversion system layout in this analysis.

## 2.2. Conceptual Design of Power Conversion System

Based on the previous study, MOBIS adopted a recompressing Brayton cycle for its layout (Halimi and Suh, 2010b; Jeong, 2010) as illustrated in Figure 2-2. In this conceptual design step, the power conversion system is designed using energy balance equation to generate the operating conditions of main components of MOBIS.
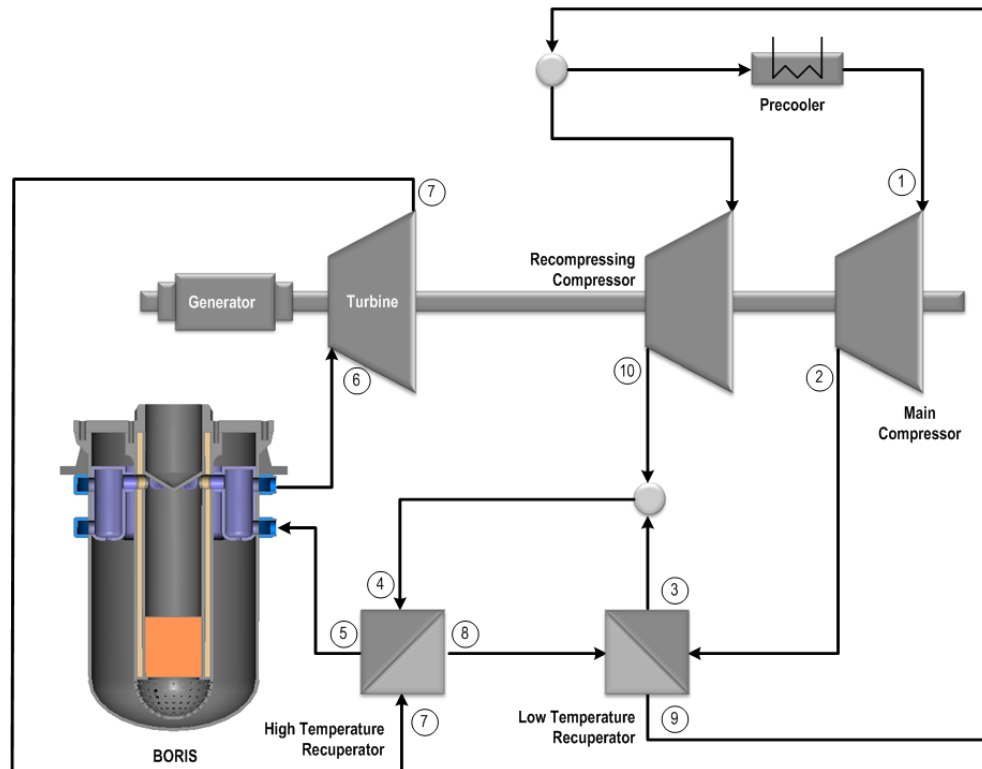


**Figure 2-2. MOBIS scheme**

In this first design step, the pipe line pressure drop by friction is neglected. The amount of heat transfer through heat exchangers is assumed constant. Also the efficiencies of turbomachineries are constant and independent to mass flow rate.

The flowchart of conceptual design system code is shown in Figure 2-3. Base on the critical point of the working fluid, the calculation is started from the inlet of main compressor. The difference of calculated and assumed HTR effectiveness $\varepsilon_{HTR}$ is chosen as calculation convergence criterion.

The required thermal power is estimated by using the mass and energy balance equations at heat exchangers, low temperature recuperator (LTR), and high temperature recuperator (HTR) as follow (Halimi and Suh, 2010b)

$$Q = m_{total} \ (h_6 - h_5 ) \tag{2-1}$$

$$m_r(h_3 - h_2) = \ (h_8 - h_9 ) \tag{2-2}$$

$$h_5 - h_4 = h_7 - h_8 \tag{2-3}$$

$$h_4 = m_r h_3 + (1 - m_r )h_{10} \tag{2-4}$$

where $m_{total}$ is the total mass flow rate of S-CO$_2$, $m_r$ is the mass flow separation fraction to LTR, $Q$ is the reactor power, $h$ is the enthalpy, and the subscripted numerals refer to the points of state as illustrated in Figure 2-2.

The isentropic efficiency of the turbine and compressor, and the effectiveness of the HTR and LTR are proposed to reduce the number of unknown parameters as follows

$$\eta_{turbine} \ = \frac{h_6 - h_7}{h_6 - h_{7s}} \tag{2-5}$$

$$\eta_{comp \ \#1} = \frac{h_{2s} - h_1}{h_2 - h_1} \tag{2-6}$$

$$\eta_{comp \ \#2} = \frac{h_{10s} - h_9}{h_{10} - h_9} \tag{2-7}$$

$$\varepsilon_{HTR} = \frac{T_7 - T_8}{T_7 - T_4} \tag{2-8}$$

$$\varepsilon_{LTR} = \frac{T_8 - T_9}{T_8 - T_2} \tag{2-9}$$

where subscript $s$ represents the isentropic process, $\eta_{turbine}$ is the turbine efficiency, $\eta_{comp\ \#1}$ and $\eta_{comp\ \#2}$ are the main and the recompression compressor efficiency, and $\varepsilon_{HTR}$ and $\varepsilon_{LTR}$ are the effectiveness of HTR and LTR. The net work and thermal efficiency are calculated as follows

$$W_{net} = m_{total}\,(h_6 - h_7) - m_{total}\,m_r(h_2 - h_1) - m_{total}\,(1 - m_r)(h_{10} - h_9)$$

$$\tag{2-10}$$

$$\eta_{thermal} = \frac{W_{net}}{Q} \tag{2-11}$$

where $W_{net}$ is the net power generated, and $\eta_{thermal}$ is the thermal thermal efficiency. Figure 2-3 shows the diagram of conceptual design.
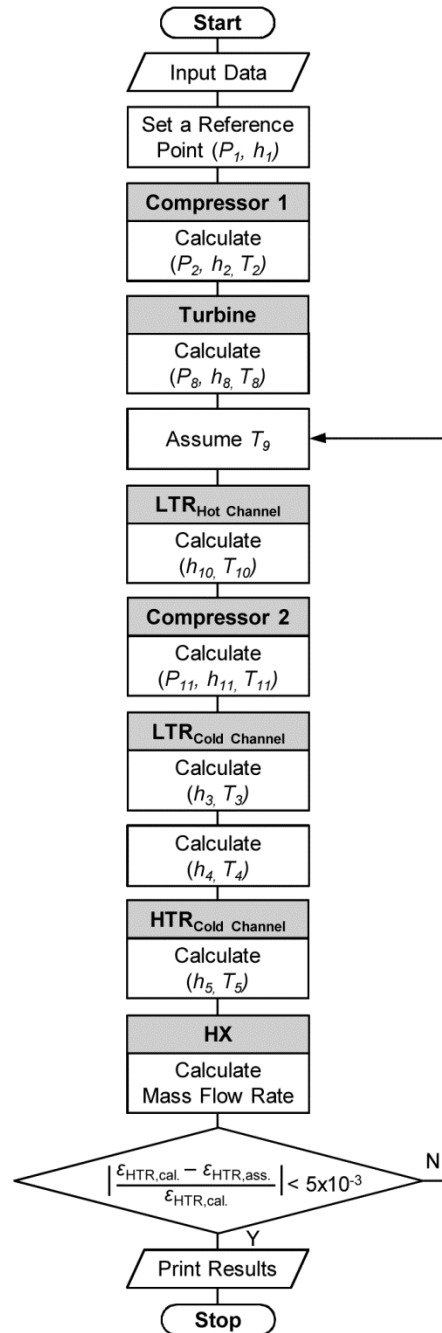
**Figure 2-3. Conceptual design flowchart**

## 2.2.1. Code Benchmarking

Before the conceptual design code is adopted for MOBIS, the code was firstly validated. Thus, the numerical model of $CO_2$ recompression cycle has been benchmarked against the published data with differing reactor types (Ishiyama et al., 2008; Moisseytsev and Sienicki, 2006; Seong et al., 2009). Seong et al. (2009) developed a computation model to analyze the performance of 600 MWe Korea Advanced Liquid Metal Reactor (KALIMER-600) coupled with an S-CO$_2$ Brayton cycle. This reactor is a pool-type reactor and uses sodium as the coolant in the primary and intermediate loops. The KALIMER-600 power conversion system is schematically similar to that illustrated in Figure 2-2, except that the power conversion system is connected to the primary system via intermediate loops. To approach the critical point and maximize the thermal efficiency, the main compressor inlet temperature and pressure are set equal to 304.40 K and 7.4 MPa, respectively. The mass flow separation, or flow split, fraction was assigned to be 71%. The turbomachinery efficiencies are assumed to be 93%, 89%, and 87% for turbine, main and recompressing compressor, respectively. By applying the same recuperator effectiveness ($\varepsilon_{HTR}$ = 92% and $\varepsilon_{LTR}$ = 95%), the current calculation shows that the cycle thermal efficiency is 42.8% with total mass flow rate 8,082 kg/s splitting into 5,738 kg/s and 2,344 kg/s. This value matches with the KALIMER-600 reference data of 42.8% with total mass flow rate 8,077 kg/s splitting into 5,734 kg/s and 2,342 kg/s. In terms of thermodynamic properties error at each cycle state, the temperature and entropy maximum errors are 0.77% and 0.56%, respectively, as summarized in Table 2-2(a) and Figure 2-4(a).

Another comparison for a different operating point is made to data from the Secure Transportable Autonomous Reactor with Liquid Metal coolant (STAR-LM) coupled to the S-CO$_2$ Brayton cycle (Moisseytsev and Sienicki, 2006). STAR-LM is a lead-cooled pool-type fast reactor. The reactor core power is 400 MWt. The STAR-LM power conversion system is the same as in KALIMER-600 except that

the heat from the reactor is transferred to the S-CO$_2$ Brayton cycle in in-reactor heat exchanger instead of intermediate loop heat exchangers. The lowest temperature and pressure are the same as in KALIMER-600 power conversion system. But the highest temperature is 814 K instead of 781 K. The flow split fraction is set equal to 65%. By applying the same turbine efficiency and effectiveness of both recuperator of $\eta_{turbine} = 91\%$, $\eta_{comp\#1} = 91.6\%$, $\eta_{comp\#2} = 91\%$, $\varepsilon_{HTR} = 98.3\%$ and $\varepsilon_{LTR} = 98.7\%$, the cycle thermal efficiency is 46% with total mass flow rate 2,252 kg/s splitting into 1,464 kg/s and 788 kg/s according to conceptual design code. This value closely matches with the reference calculation of 45% with total mass flow rate 2,276 kg/s splitting into 1,479 kg/s and 797 kg/s. The calculation results also show that the maximum error in temperature and entropy at all the operating points are minor, i.e. 0.81% and 0.57%, respectively, as exemplified by the temperature-specific entropy ($T$-$s$) diagram in Figure 2-4(b).

Further, the design code calculation results are benchmarked against the prototype fusion reactor reported data (Ishiyama et al., 2008). In this case the existence of divertor heat source should be taken into account. The total blanket and divertor power are 2,420 MW and 490 MW, respectively, which are divided into four module systems in consideration of the component capacity. The divertor heat source is used to heat up the CO$_2$ leaving the main compressor as shown in Figure 2-5. The maximum temperature is set equal to 753 K with maximum pressure 20.6 MPa. The results show that the predicted thermal efficiency by utilizing design code is 37% with total mass flow rate 3,843kg/s which reasonable concurs with the prototype design data of 36% with same total mass flow rate 3,843kg/s. The thermodynamic properties at each operation point are mostly in close agreements with the reference data (Ishiyama et al., 2008) as illustrated in Figure 2-5 and Table 2-3.

24
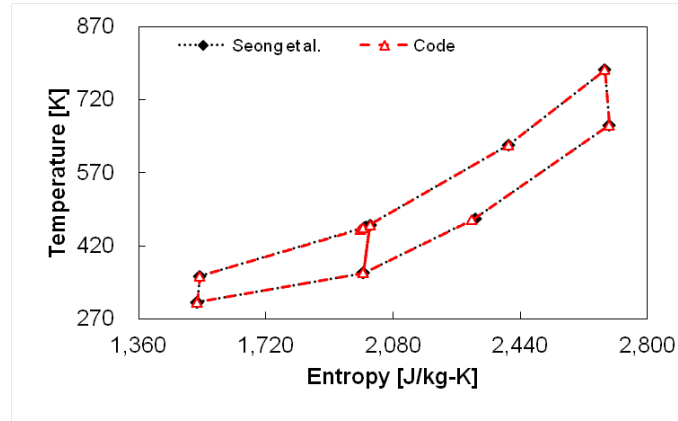
(a)  Code-(Seong et al., 2009)
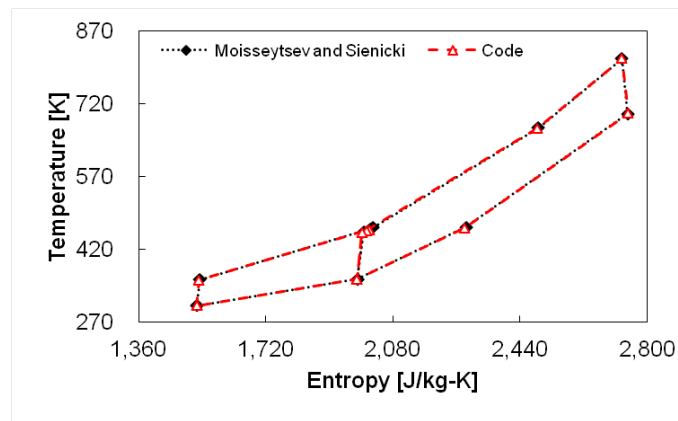


(b)  Code-(Moisseytsev and Sienicki, 2006)

**Figure 2-4.** *T-s* **diagram of code validation results**
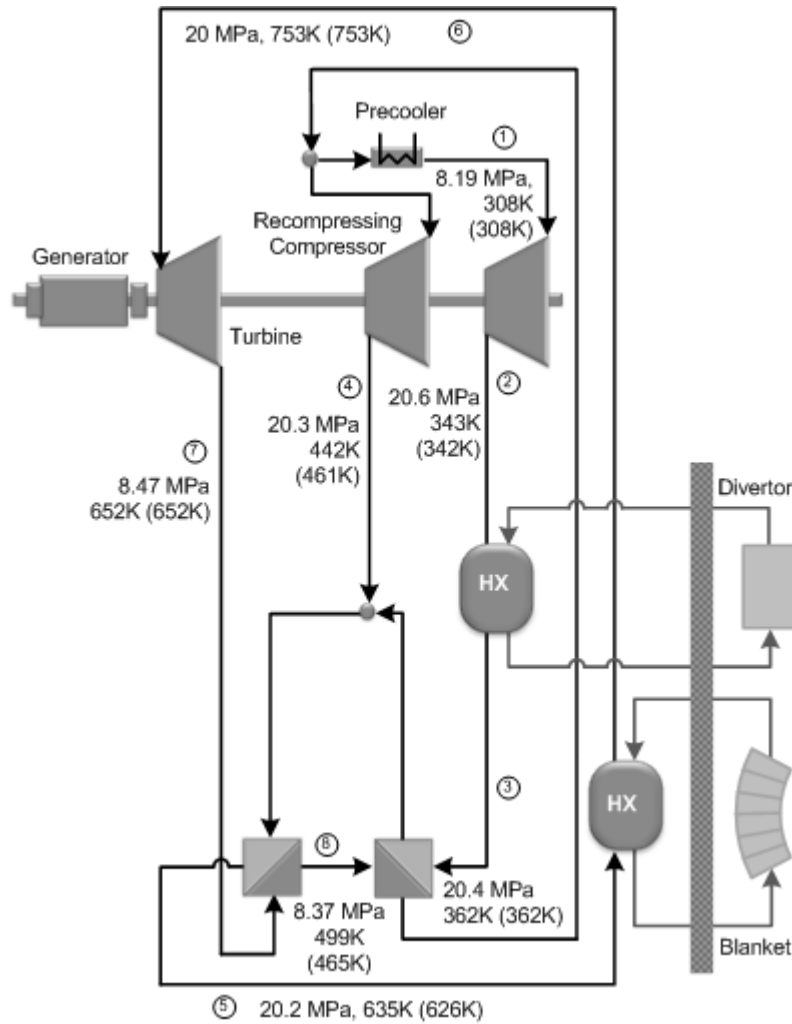
**Figure 2-5. Code validation with prototype fusion reactor reference model**
(Ishiyama et al., 2008)

**Table 2-2. Code validation results**

(A: Code, B: references, C: error (%); (a) Seong et al. (2009), (b) Moisseytsev and

Sienicki (2006))

| No. | Pressure [MPa] | Temperature [K] | | | Entropy[J/kg-K] | | | Enthalpy [kJ/kg] | | |
|-----|------|-----|-----|-----|------|------|-----|------|------|-----|
| | | A | B | C | A | B | C | A | B | C |
| *(a)* | | | | | | | | | | |
| 1 | 7.40 | 304 | 304 | 0.00 | 1525 | 1525 | 0.00 | 360 | 360 | 0.00 |
| 2 | 20.00 | 358 | 358 | 0.06 | 1534 | 1532 | 0.10 | 389 | 389 | 0.14 |
| 3 | 19.98 | 454 | 457 | 0.77 | 1988 | 1999 | 0.56 | 570 | 576 | 0.89 |
| 4 | 19.98 | 456 | 459 | 0.58 | 1995 | 2004 | 0.42 | 574 | 578 | 0.66 |
| 5 | 19.94 | 627 | 627 | 0.01 | 2407 | 2407 | 0.00 | 794 | 794 | 0.01 |
| 6 | 19.74 | 781 | 781 | 0.00 | 2679 | 2679 | 0.00 | 983 | 983 | 0.00 |
| 7 | 7.60 | 667 | 667 | 0.00 | 2692 | 2692 | 0.00 | 861 | 861 | 0.00 |
| 8 | 7.53 | 473 | 476 | 0.71 | 2304 | 2312 | 0.35 | 641 | 645 | 0.59 |
| 9 | 7.46 | 364 | 364 | 0.00 | 1995 | 1996 | 0.00 | 512 | 512 | 0.00 |
| 10 | 19.98 | 462 | 463 | 0.03 | 2015 | 2015 | 0.02 | 583 | 583 | 0.03 |
| *(b)* | | | | | | | | | | |
| 1 | 7.40 | 304 | 304 | 0.00 | 1525 | 1525 | 0.00 | 360 | 360 | 0.00 |
| 2 | 20.00 | 358 | 358 | 0.08 | 1531 | 1534 | 0.14 | 388 | 389 | 0.20 |
| 3 | 19.98 | 462 | 465 | 0.81 | 2012 | 2024 | 0.57 | 582 | 587 | 0.91 |
| 4 | 19.98 | 459 | 462 | 0.67 | 2005 | 2015 | 0.47 | 578 | 583 | 0.75 |
| 5 | 19.93 | 670 | 672 | 0.22 | 2489 | 2492 | 0.11 | 847 | 849 | 0.21 |
| 6 | 19.88 | 814 | 814 | 0.00 | 2729 | 2729 | 0.00 | 1024 | 1024 | 0.00 |
| 7 | 7.71 | 701 | 700 | 0.13 | 2746 | 2745 | 0.06 | 900 | 899 | 0.12 |
| 8 | 7.58 | 465 | 466 | 0.39 | 2283 | 2287 | 0.19 | 632 | 634 | 0.32 |
| 9 | 7.41 | 359 | 359 | 0.06 | 1979 | 1980 | 0.04 | 506 | 506 | 0.06 |
| 10 | 19.98 | 455 | 457 | 0.40 | 1992 | 1998 | 0.29 | 572 | 575 | 0.46 |

**Table 2-3. Code validation with prototype fusion reactor reference model**

(A: Code, B: Ishiyama et al. (2008), C: error (%))

| No. | Pressure [MPa] | Temperature [K] | | | Entropy[J/kg-K] | | | Enthalpy[kJ/kg] | | |
|---|---|---|---|---|---|---|---|---|---|---|
| | | A | B | C | A | B | C | A | B | C |
| 1 | 8.19 | 308 | 308 | 0.00 | 1401 | 1401 | 0.00 | 324 | 324 | 0.00 |
| 2 | 20.6 | 343 | 342 | 0.13 | 1409 | 1406 | 0.23 | 347 | 345 | 0.31 |
| 3 | 20.4 | 362 | 362 | 0.01 | 1554 | 1554 | 0.02 | 397 | 397 | 0.02 |
| 4 | 20.3 | 442 | 461 | 4.09 | 1944 | 2006 | 3.07 | 552 | 580 | 4.79 |
| 5 | 20.2 | 635 | 626 | 1.37 | 2419 | 2403 | 0.69 | 803 | 793 | 1.33 |
| 6 | 20.0 | 753 | 753 | 0.00 | 2631 | 2631 | 0.00 | 949 | 949 | 0.00 |
| 7 | 8.47 | 652 | 652 | 0.01 | 2643 | 2643 | 0.00 | 842 | 842 | 0.01 |
| 8 | 8.37 | 499 | 465 | 7.37 | 2341 | 2260 | 3.59 | 668 | 629 | 6.22 |

### 2.2.2. Conceptual Design of MOBIS

Considering the current available technology, Dostal et al. (2006a) suggested the main compressor pressure outlet should be 20 MPa for a recompression Brayton cycle. This choice is still enable the $S\text{-}CO_2$ cycle to achieve very attractive efficiency. Thus the maximum cycle pressure of MOBIS is set to be 20 MPa.

The maximum temperature and minimum enthalpy are chosen to be 813.15 K and 360.01 kJ/kg-K, respectively, for the boundary conditions as depicted in Table 2-4. The required thermal power is estimated resorting to the mass and energy balance equations at the heat exchanger interfaces between the primary and secondary systems, the low temperature recuperator (LTR), and the high temperature recuperator (HTR) (Son et al., 2011).

**Table 2-4. Input parameters for BORIS**

| | |
|---|---|
| Thermal power [MW] | 23.50 |
| Turbine efficiency [%] | 93 |
| Compressor efficiency [%] | 88 |
| Low temperature recuperator effectiveness [%] | 94 |
| High temperature recuperator effectiveness [%] | 91 |
| Turbine inlet temperature [K] | 813.15 |
| Maximum pressure [MPa] | 20 |
| Minimum temperature [K] | 304.4 |

The determination of operation point is optimized based on thermal efficiency value and total volume of heat exchangers (HTR, LTR and precooler). The minimized volume of heat exchanger means a minimal required space and also reduces the cost. The six reactor heat exchangers are not covered in this optimization process.

To obtain the optimum point, various sensitivity studies on mass flow ratio, pressure ratio of recompressing compressor and heat exchanger pressure drop were performed. The main goal is to find a high thermal efficiency with minimum total heat exchanger volume.

Figure 2-6 shows three run cases for mass flow ratio value from 0.65 to 0.73. The cases were run with different pressure drop of heat exchanger and pressure ratio of recompressing compressor. In this study, the LTR has a dominant contribution on total heat exchanger volume compared to HTR and precooler. Moreover, it is presented in Figure 2-6 that the thermal efficiency will be reduced by decreasing the total volume of heat exchangers. In all cases, for mass flow split ratio less than

0.70, the total volume of heat exchangers will decrease significantly by increasing the pressure ratio value. Based on this result, the split ratio of 0.7 is a reasonable value for MOBIS.
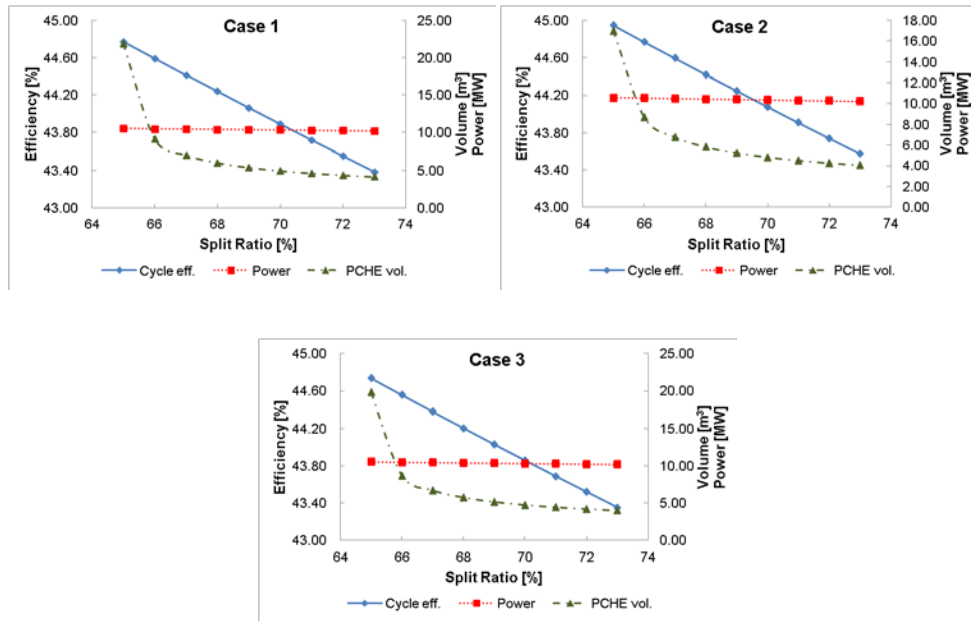


**Figure 2-6. Mass flow ratio to thermal efficiency and total PCHE volume**

In this study, a sensitivity of turbomachinery pressure ratio to thermal efficiency was performed as well. Figure 2-7 illustrated the results of this sensitivity analysis. Seven cases were selected for this investigation. Considering the thermal efficiency and total volume of heat exchangers, the pressure ratio of 2.65 is a reasonable for the recompressing compressor.
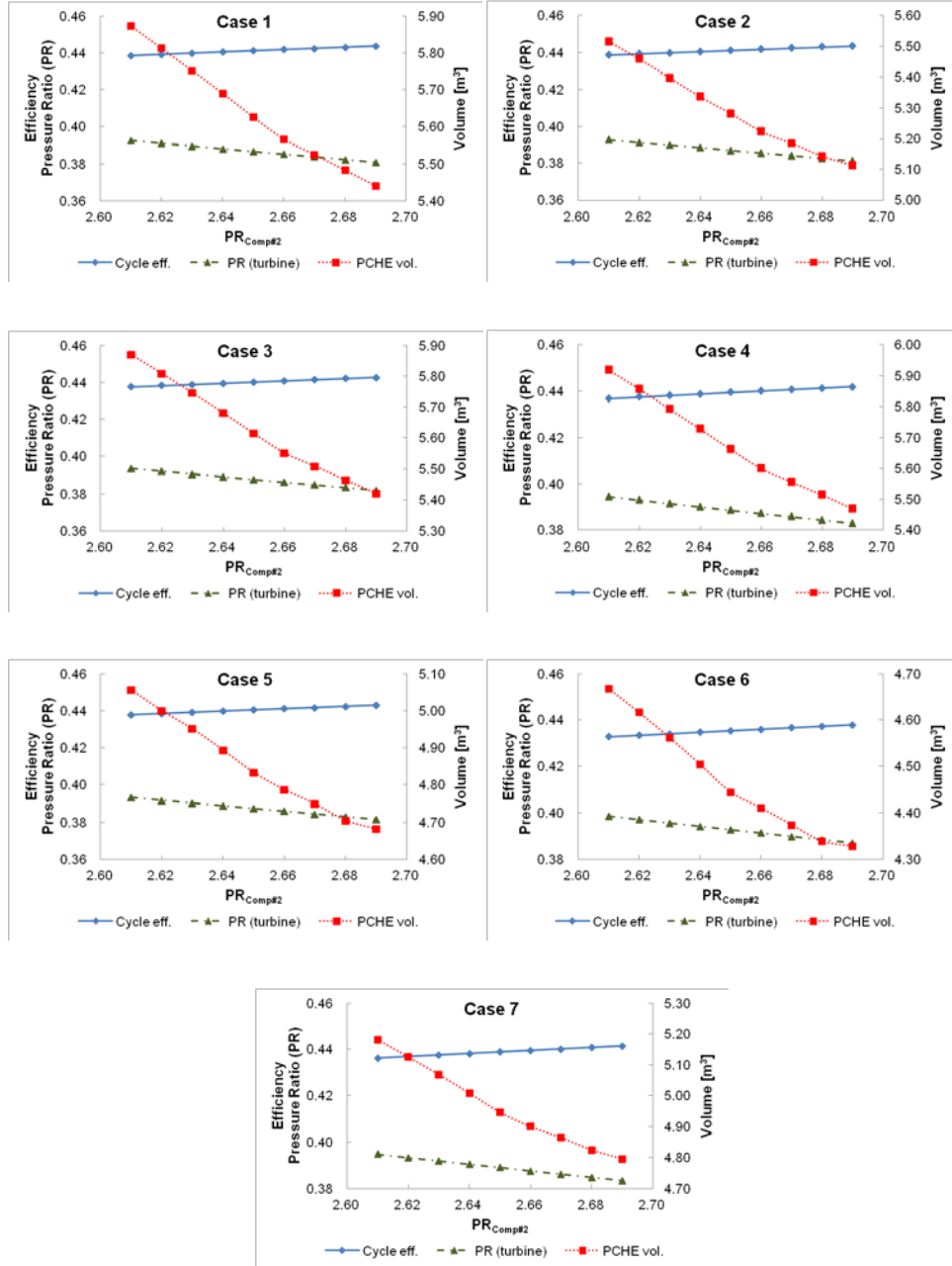
**Figure 2-7. Pressure ratio of recompressing compressor**

Also, a study on sensitivity of turbomachinery efficiency to thermal efficiency was performed. Figure 2-8 illustrates the turbomachinery efficiency of turbine, main compressor and recompressing compressor to thermal efficiency. It can be concluded that the selected turbine efficiency value gives more significant effect to thermal efficiency compared to both compressors.
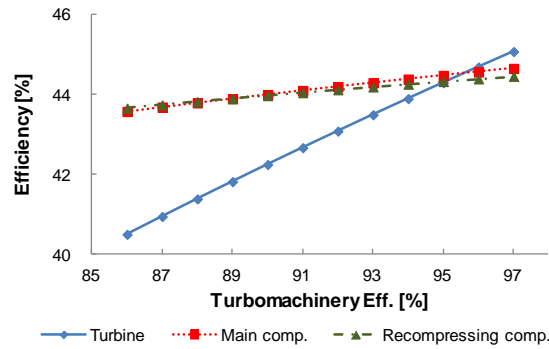


**Figure 2-8. Turbomachinery efficiency**

Table 2-5 shows the calculation result of the thermodynamic value at each significant spot for conceptual design of MOBIS. The mass flow ratio and pressure ratio of recompressing compressor are 0.70 and 2.65, respectively. The pressure drops on hot coolant and cold coolant side of heat exchangers are assumed 0.07 and 0.04 MPa. The minimum pressure is set equal to 7.40 MPa at point 1 (inlet of main compressor). The thermal efficiency and net generated power are 43.89% and 10.00 MWe, respectively. The total secondary mass flow rate is 122.1799 kg/s which splits to 85.5259 kg/s and 36.6540 kg/s before the compressors. Moreover, the pressure and temperature of inlet and outlet for the heat exchanger are found to be 19.92 MPa, 656.78K, 19.72 MPa, and 813.15K, respectively.

**Table 2-5. Conceptual design of MOBIS**

| No. | Pressure [MPa] | Temperature [K] | Enthalpy [kJ/kg] | Entropy [J/kg-K] |
|-----|-----|-----|-----|-----|
| 1 | 7.40 | 304.40 | 360.01 | 1,525 |
| 2 | 20.00 | 358.30 | 389.59 | 1,535 |
| 3 | 19.96 | 471.80 | 596.04 | 2,043 |
| 4 | 19.96 | 469.10 | 592.38 | 2,035 |
| 5 | 19.92 | 656.78 | 830.60 | 2,464 |
| 6 | 19.72 | 813.15 | 1022.94 | 2,729 |
| 7 | 7.67 | 698.16 | 896.91 | 2,743 |
| 8 | 7.60 | 488.75 | 658.70 | 2,339 |
| 9 | 7.53 | 366.13 | 514.18 | 1,999 |
| 10 | 19.96 | 463.11 | 583.85 | 2,017 |

## 2.3. Key Components of MOBIS

Design of MOBIS power conversion system focuses on the key components of MOBIS i.e. heat exchangers (HTR, LTR, and pre-cooler) and turbomachinery (turbine, main compressor and recompressing compressor). All designs are based on the operation points as shown in Table 2-5

### 2.3.1. Heat Exchanger

MOBIS adopts printed circuit heat exchanger (PCHE) type for HTR, LTR and precooler. The PCHE technology was originally invented by as a result of research performed at the University of Sydney in the early 1980's. Then the concept was commercialized by Heatric (Johnston et al., 2001). Its compact core is constructed

by chemically milling flow passages into flat metal plates, stacking and diffusion bonding the plates into a single block.

As one of the most promising heat exchanger technologies, the EU Framework Programme have selected this Heatric PCHE as one of the recuperator candidates for the High Temperature Reactor-European program (Pra et al., 2008).

The MOBIS has three heat exchanger modules viz. high temperature recuperator (HTR), low temperature recuperator (LTR) and pre-cooler. Considering the optimum value, total heat exchanger volume and thermal efficiency (as discussed in previous chapter), the total volume of 4.9472 $m^3$ (43.89% efficiency) is selected as the conceptual design of MOBIS.

In this design, the flow path is assumed as zig-zag shape. The flow path diameter and plate thickness should be in the range of 0.5 to 2.0 mm. Only flow path direction change and pressure drop by friction are considered. The structure material is SS316.

The governing equation of mass, momentum and energy conservation equation can be written as follows

$$m_i = \sum_{j=1}^{N} m_{i,j} \tag{2-12}$$

$$\Delta P_{i,j} = \left(\frac{m_{i,j}}{A_{i,j}}\right)^2 \left[\left(f\frac{m_{i,j}}{A_{i,j}} + K_{form_{i,j}}\right)\left(\frac{1}{2\rho_{avg_{i,j}}}\right) + \left(\frac{1}{\rho_{out_{i,j}}} - \frac{1}{\rho_{in_{i,j}}}\right)\right] \tag{2-13}$$

$$Q_i = m_{i,j}\left(h_{out_i} - h_{in_i}\right) = UA_h\Delta T_{LMTD} \tag{2-14}$$

where $i$ represents hot or cold channel, $N$ is the total number of channels.

The friction factor and form loss coefficient is calculated using correlation formulated by Ishizuka et al. (Ishizuka et al., 2006) as follows

$$f = 4(0.0014 + 0.125\text{Re}^{-0.32}) \tag{2-15}$$

$$K_{form} = NC\left[0.946 \sin^2\left(\frac{180-\theta_j}{2}\right) + 2.047 \sin^4\left(\frac{180-\theta_j}{2}\right)\right] \tag{2-16}$$

where $NC$ is the curves number in one channel. The similar correlation was also adopted by previous works (Hejzlar et al., 2006b; Jeong, 2010)

Considering the channel flow path, the correlation recommended by Hesselgreaves (2001) is applied for heat transfer correlation as follows

$$Nu = 4.089 \qquad\qquad \text{for } \text{Re} \le 2300 \tag{2-17}$$

$$Nu = 0.125\text{Re}^{0.64}\text{Pr}^{0.33} \qquad\qquad \text{for } 5000 \le \text{Re} \tag{2-18}$$

Due to the discontinuity on the correlation, it was suggested to use linear interpolation to obtain following equation (Dostal, 2004)

$$Nu = 4.089 + \frac{Nu_{\text{Re}=5000}-4.089}{5000-2300}(\text{Re}-2300) \ \text{ for } 2300 \le \text{Re} \le 5000 \tag{2-19}$$

The heat exchanger effectiveness is estimated as follows (Nikitin et al., 2006)

$$\varepsilon = \frac{T_{hot,in}-T_{hot,out}}{T_{hot,in}-T_{cold,out}} \tag{2-20}$$

The conceptual design of MOBIS heat exchangers are presented in Table 2-6 through 2-8.

**Table 2-6. Conceptual design of HTR**

| Parameter | Hot Side | Cold Side |
|---|---|---|
| Capacity [MWt] | 29.10 | |
| Inlet temperature [K] | 698.16 | 469.17 |
| Outlet temperature [K] | 488.75 | 656.78 |
| Inlet pressure [MPa] | 7.67 | 19.96 |
| Outlet pressure [MPa] | 7.60 | 19.92 |
| Total flow rate [kg/s] | 122.18 | 122.18 |
| Effectiveness | 91.45 | |
| Channel diameter [mm] | 1.50 | 1.50 |
| Number of turns | 87 | 92 |
| Bending angle [deg] | 170.00 | 143.77 |
| Flow area per channel [mm$^2$] | 0.88 | 0.88 |
| Length per channel [mm] | 873.54 | 915.61 |
| Total channels number | 216,542 | 206,594 |
| Total heat transfer area [m$^2$] | 729.43 | 729.43 |
| Dimension (L x W x H) [m] | 0.8702 x 0.6000 x 3.4464 | |

**Table 2-7. Conceptual design of LTR**

| Parameter | Hot Side | Cold Side |
|---|---|---|
| Capacity [MWt] | 17.66 | |
| Inlet temperature [K] | 488.75 | 358.3 |
| Outlet temperature [K] | 366.13 | 471.8 |
| Inlet pressure [MPa] | 7.60 | 20.00 |
| Outlet pressure [MPa] | 7.53 | 19.96 |
| Total flow rate [kg/s] | 122.18 | 85.53 |
| Effectiveness | 94.00 | |
| Channel diameter [mm] | 1.50 | 1.50 |
| Number of turns | 141 | 165 |
| Bending angle [deg] | 170.00 | 117.46 |
| Flow area per channel [mm$^2$] | 0.88 | 0.88 |
| Length per channel [mm] | 1412.70 | 1646.55 |
| Total channels number | 216756 | 185972 |
| Total heat transfer area [m$^2$] | 1180.81 | 1180.81 |
| Dimension (L x W x H) [m] | 1.4073 x 0.6000 x 3.1078 | |

**Table 2-8. Conceptual design of pre-cooler**

| Parameter | Hot Side | Cold Side |
|---|---|---|
| Capacity [MWt] | 13.19 | |
| Inlet temperature [K] | 366.13 | 303.15 |
| Outlet temperature [K] | 304.4 | 308.95 |
| Inlet pressure [MPa] | 7.53 | 0.33 |
| Outlet pressure [MPa] | 7.40 | 0.10 |
| Total flow rate [kg/s] | 85.53 | 548.84 |
| Effectiveness | 98.02 | |
| Channel diameter [mm] | 1.50 | 1.50 |
| Number of turns | 58 | 43 |
| Bending angle [deg] | 100.00 | 180.00 |
| Flow area per channel [mm$^2$] | 0.88 | 0.88 |
| Length per channel [mm] | 578 | 430 |
| Total channels number | 88,088 | 118,403 |
| Total heat transfer area [m$^2$] | 196.36 | 196.36 |
| Dimension (L x W x H) [m] | 0.4428 x 0.6000 x 1.9701 | |

### 2.3.2. Turbine

As mentioned in the previous sub-chapter, the thermal efficiency is more sensitive to turbine efficiency than the compressor ones. Thus it is desirable to maximize the efficiency of turbine to recover efficiency losses on compressor side.

Axial turbine type is selected for MOBIS. Based on earlier researches on the S-CO$_2$ power cycle focused on axial turbines and compressors, it was found that the axial ones have higher efficiencies compared with the radial machines. But the axial machines also have drawbacks such as small operating margin to surge and stall on

axial compressor that may make more complex in term on control (Hejzlar et al., 2006b). The very compact turbine is a significant advantage of MOBIS power conversion system for BORIS application where space is limited especially for marine application such as NAVIS.

The design of turbine is based on $N_s$-$D_s$ diagram in Figure 2-9. The correlation of specific speed and angular speed, flow and adiabatic enthalpy rise can be written as follows

$$N_s = \frac{N(V_1)^{\frac{1}{2}}}{(H_{ad})^{\frac{3}{4}}} \tag{2-21}$$
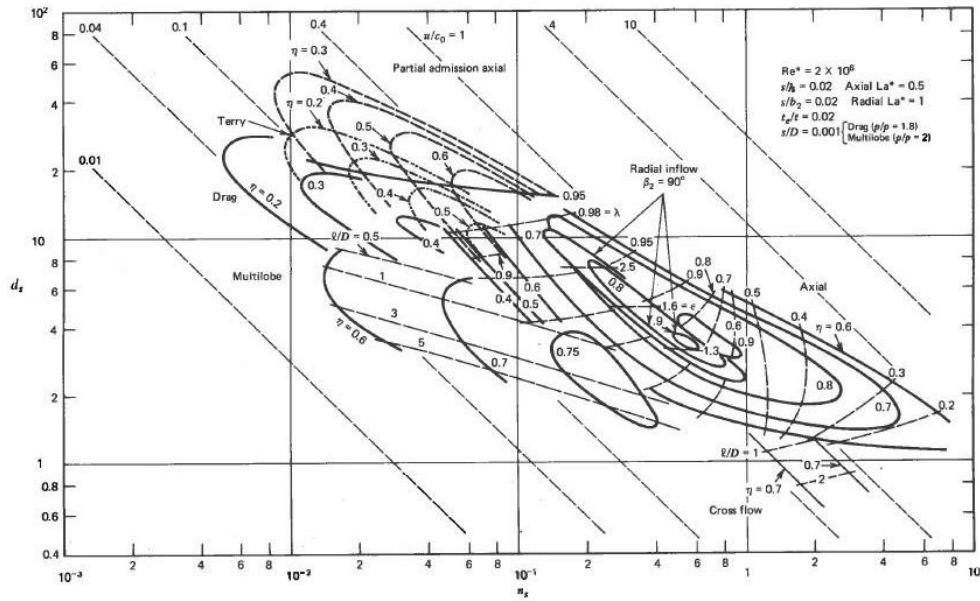


**Figure 2-9. $N_s$ - $D_s$ chart for turbine design** (Balje, 1981)

The optimum diameter can be obtained as follows

$$D_s = \frac{D(H_{ad})^{\frac{1}{4}}}{(V_1)^{\frac{1}{2}}}$$ (2-22)

The preliminary design result is provided in Table 2-9.

**Table 2-9. Preliminary design of turbine**

| Stage | | Temperature [K] | Pressure [MPa] | Density [kg/m³] | Enthalpy [kJ/kg] | Diameter [m] |
|---|---|---|---|---|---|---|
| 1 | Inlet | 813.15 | 19.72 | 124.37 | 1022.94 | 0.3263 |
|   | Isentropic exit | 791.78 | 16.71 | 109.14 | 999.00 | |
| 2 | Inlet | 791.78 | 16.71 | 109.14 | 999.00 | 0.3498 |
|   | Isentropic exit | 766.80 | 13.70 | 93.14 | 971.36 | |
| 3 | Inlet | 766.80 | 13.70 | 93.14 | 971.36 | 0.3868 |
|   | Isentropic exit | 736.57 | 10.68 | 76.22 | 938.32 | |
| 4 | Inlet | 736.57 | 10.68 | 76.22 | 938.32 | 0.4370 |
|   | Isentropic exit | 697.87 | 7.67 | 58.16 | 896.58 | |

### 2.3.3. Compressor

The design of compressor is based on $N_s$-$D_s$ diagram in Figure 2-10. This diagram can be utilize for preliminary sizing of turbomachinery. The optimum specific speed for a centrifugal type of compressor is 0.6-0.77 (Fuller et al., 2012; Rodgers, 1979). The correlation of specific speed and angular speed, flow and adiabatic enthalpy rise can be written as follows

$$N_s = \frac{N(V_1)^{\frac{1}{2}}}{(H_{ad})^{\frac{3}{4}}}$$ (2-23)

An optimum efficiency is main goal in the design work. But a minimum shaft speed is also preferred to get design result with more availability and longer life for seals and gear box hardware (Fuller et al., 2012).

Using a similar calculation, the optimum diameter can be obtained as follows

$$D_s = \frac{D(H_{ad})^{\frac{1}{4}}}{(V_1)^{\frac{1}{2}}}$$

(2-24)

The preliminary design result of the main compressor and recompressing compressor are provided in Table 2-10 and 2-11, respectively.
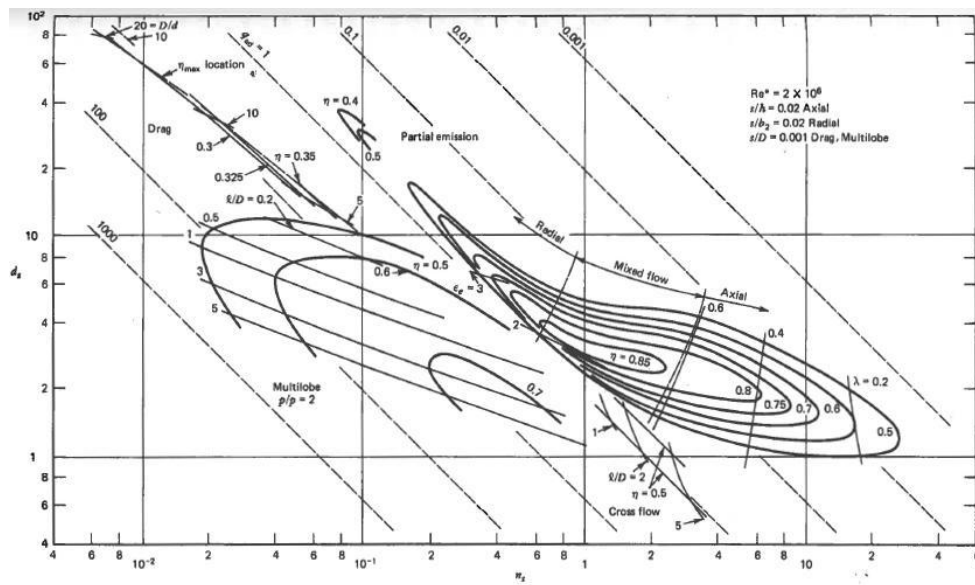


**Figure 2-10. $N_s$ - $D_s$ diagram for compressor design** (Balje, 1981)

**Table 2-10. Preliminary design of main compressor**

| | Stage | Temperature [K] | Pressure [MPa] | Density [kg/m$^3$] | Enthalpy [kJ/kg] | Diameter [m] |
|---|---|---|---|---|---|---|
| 1 | Inlet | 304.40 | 7.40 | 368.61 | 360.01 | 0.2369 |
| | Isentropic exit | 323.83 | 10.55 | 438.32 | 370.80 | |
| 2 | Inlet | 323.83 | 10.55 | 438.32 | 370.80 | 0.223 |
| | Isentropic exit | 338.35 | 13.70 | 487.15 | 378.98 | |
| 3 | Inlet | 338.35 | 13.70 | 487.15 | 378.98 | 0.1828 |
| | Isentropic exit | 349.86 | 16.85 | 524.62 | 386.06 | |
| 4 | Inlet | 349.86 | 16.85 | 524.62 | 386.06 | 0.1773 |
| | Isentropic exit | 359.44 | 20.00 | 554.88 | 392.52 | |

**Table 2-11. Preliminary design of recompressing compressor**

| | Stage | Temperature [K] | Pressure [MPa] | Density [kg/m³] | Enthalpy [kJ/kg] | Diameter [m] |
|---|---|---|---|---|---|---|
| 1 | Inlet | 366.13 | 7.53 | 136.19 | 514.2 | 0.2567 |
| | Isentropic exit | 381.92 | 8.91 | 154.06 | 524.99 | |
| 2 | Inlet | 381.92 | 8.91 | 154.06 | 524.99 | 0.2444 |
| | Isentropic exit | 395.80 | 10.29 | 170.93 | 534.61 | |
| 3 | Inlet | 395.80 | 10.29 | 170.93 | 534.61 | 0.2343 |
| | Isentropic exit | 408.21 | 11.67 | 186.93 | 543.35 | |
| 4 | Inlet | 408.21 | 11.67 | 186.93 | 543.35 | 0.226 |
| | Isentropic exit | 419.42 | 13.05 | 202.13 | 551.38 | |
| 5 | Inlet | 419.42 | 13.05 | 202.13 | 551.38 | 0.2189 |
| | Isentropic exit | 429.66 | 14.44 | 216.6 | 558.82 | |
| 6 | Inlet | 429.66 | 14.44 | 216.6 | 558.82 | 0.2128 |
| | Isentropic exit | 439.09 | 15.82 | 230.41 | 565.79 | |
| 7 | Inlet | 439.09 | 15.82 | 230.41 | 565.79 | 0.177 |
| | Isentropic exit | 447.81 | 17.20 | 243.61 | 572.35 | |
| 8 | Inlet | 447.81 | 17.20 | 243.61 | 572.35 | 0.1726 |
| | Isentropic exit | 455.94 | 18.58 | 256.23 | 578.56 | |
| 9 | Inlet | 455.94 | 18.58 | 256.23 | 578.56 | 0.1688 |
| | Isentropic exit | 463.55 | 19.96 | 268.33 | 584.47 | |

For further design, one important aspect in compressor design, the correct simulation of various losses, should be considered as well.

Incidence loss (Conrad et al., 1980)

$$\Delta h_{inc} = f_{inc} \frac{W_{ui}^2}{2} \qquad (2\text{-}25)$$

where $f_{inc} = 0.5 - 0.7$.

Blade loading loss(Coppage et al., 1956)

$$\Delta h_{blade} = 0.05 D_f^2 U_2^2 \tag{2-26}$$

Skin friction loss (Jansen, 1967)

$$\Delta h_{skin} = 2 C_f \frac{L_b}{D_{hyd}} \overline{W}^2 \tag{2-27}$$

Clearance loss (Jansen, 1967)

$$\Delta h_{cl} = 0.6 \frac{\varepsilon}{b_2} V_2 \left\{ \frac{4\pi}{b_2 Z} \left[ \frac{r_{1t}^2 - r_{1h}^2}{(r_2 - r_{1t})(1 + \rho_2/\rho_1)} \right] V_{u2} V_{m1m} \right\} \tag{2-28}$$

where $\overline{W} = \frac{V_{1t} + V_2 + W_{1t} + 2W_{1h} + 3W_2}{8}$

Mixing loss (Johnston and Dean Jr., 1966)

$$\Delta h_{mix} = \frac{1}{1 + \tan^2 \alpha_2} \left( \frac{1 - \varepsilon_{wake} - b^*}{1 - \varepsilon_{wake}} \right)^2 \frac{V_2^2}{2} \tag{2-29}$$

Vaneless diffuser loss (Stanitz, 1952)

$$\Delta h_{vaneless} = C_p T_{02} \left[ \left( \frac{P_3}{P_{03}} \right)^{(\gamma-1)/\gamma} - \left( \frac{P_3}{P_{02}} \right)^{(\gamma-1)/\gamma} \right] \tag{2-30}$$

Disc friction loss (Daily and Nece, 1960)

$$\Delta h_{disk} = f_{disk} \frac{\overline{\rho} U_2^3 r_2^2}{4\dot{m}} \tag{2-31}$$

$$\overline{\rho} = \frac{\rho_1 + \rho_2}{2} \tag{2-32}$$

$$f_{disk} = \begin{cases} \frac{2.67}{\text{Re}_{disk}^{0.5}}, & \text{Re}_{disk} < 3 \times 10^5 \\ \frac{0.0622}{\text{Re}_{disk}^{0.2}}, & \text{Re}_{disk} \geq 3 \times 10^5 \end{cases} \tag{2-33}$$

$$\text{Re}_{disk} = \frac{U_2 r_2}{v_2} \tag{2-34}$$

Due to the clearance between the impeller, rotating at high velocity, and the compressor housing, it will generate recirculation losses which formulated as follows (Coppage et al., 1956)

$$\Delta h_{rc} = U_2^2 0.02 (\tan\alpha_2)^{\frac{1}{2}} D_f^2 \tag{2-35}$$

Leakage loss (Aungier, 1995)

$$\Delta h_{leakage} = \frac{\dot{m}_{cl} U_{cl} U_2}{2\dot{m}} \tag{2-36}$$

$$U_{cl} = 0.816 \sqrt{\frac{2\Delta P_{cl}}{\rho_2}} \tag{2-37}$$

$$\Delta P_{cl} = \frac{\dot{m}[r_2 V_{u2} - (r_1 V_{u1})_{\text{m}}]}{Z \bar{r} \bar{b} L_\theta} \tag{2-38}$$

$$\bar{r} = \frac{r_1 + r_2}{2} \tag{2-39}$$

$$\bar{b} = \frac{b_1 + b_2}{2} \tag{2-40}$$

$$\dot{m}_{cl} = \rho_2 Z \varepsilon L_\theta U_{cl} \tag{2-41}$$

### 2.3.4. Piping System

The previous version of power conversion system code did not consider the pressure drop of piping system. To obtain more realistic results, the current analysis considered piping system based on a piping numbering method as illustrated in

Figure 2-11. Figure 2-12 shows MOBIS cycle with numbers of flow paths connecting components. MOBIS has 12 interconnecting flow paths. The current OSCA code is designed to allow for various arrangements of each path by considering various pipe geometries, cross sections, and also multiple parallel piping. By assuming that each of the 12 paths have *NP* ducts of identical geometry in parallel and each duct has *NS* sections in series, the pressure drop in each path can be calculated using following formula (Hejzlar et al., 2006b)

$$\Delta P = \sum_{i=1}^{NS} \left[ f(\text{Re}_i) \frac{L_i}{D_i} + \xi_i \right] \frac{\left( \frac{\dot{m}}{NP} \right)^2}{2 \rho A_i^2} \tag{2-42}$$

The density $\rho$ is $CO_2$ density in the path inlet. The friction factor is determined as a function of section Reynolds number as follows

$$\text{Re}_i = \frac{\dot{m} D_i}{NP A_i \mu} \tag{2-43}$$

The pipe wall roughness in the *i*-th section can be calculated based on the Idelchik correlation.
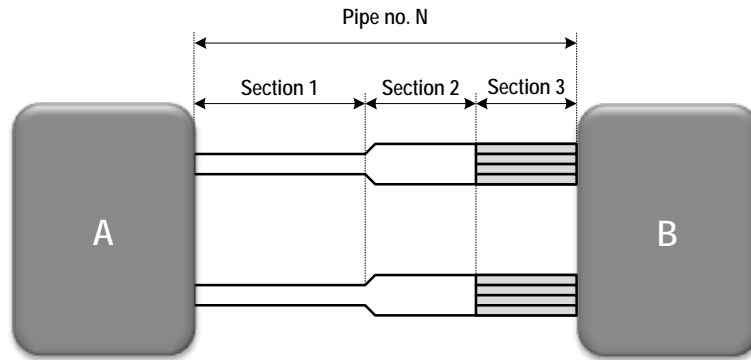


**Figure 2-11. Pipe numbering**

46
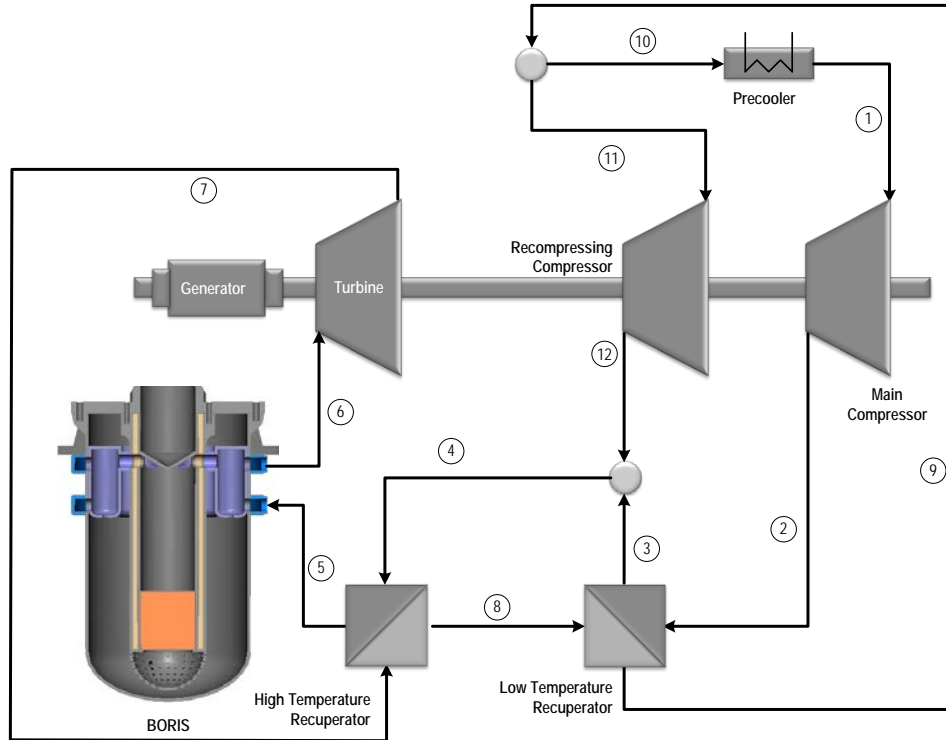
**Figure 2-12. Pipe section number of MOBIS**

## 2.4. Computational Analysis

Figure 2-13 shows the flowchart of OSCA computational process. The current code is written in Matlab script. The code has five main input files which contain general cycle, heat exchangers (HTR, LTR, precooler) and piping system data. The heat exchangers data were generated based on what discussed in Chapter 2.3.1.

Start

Input Data

Assume mass flow rate
($m_{ass.}$) ← B

**Pipe 1**
Calculate
($P_{1,out}$, $T_{1,out}$)

**Compressor 1**
Calculate
($P_{2,in}$, $T_{2,in}$)

**Pipe 9, 10, 11**
Calculate
($P_{9,out}$, $T_{9,out}$, $P_{10,out}$, $T_{10,out}$, $P_{11,out}$, $T_{11,out}$)

**Compressor 2**
Calculate
($P_{12,in}$, $T_{12,in}$)

**Pipe 6, 12**
Calculate
($P_{6,out}$, $T_{6,out}$, $P_{12,out}$, $T_{12,out}$)

**Turbine**
Calculate
($P_{7,in}$, $T_{7,in}$)

**Pipe 4, 7**
Calculate
($P_{4,out}$, $T_{4,out}$, $P_{7,out}$, $T_{7,out}$)

**HTR**
Calculate
($P_{5,in}$, $T_{5,in}$, $P_{8,in}$, $T_{8,in}$, $Q_{HTR}$)

**Pipe 5, 8**
Calculate
($P_{5,out}$, $T_{5,out}$, $P_{8,out}$, $T_{8,out}$)

A

A

**LTR**
Calculate
($P_{3,in}$, $T_{3,in}$, $P_{9,in}$, $T_{9,in}$, $Q_{LTR}$)

**Pipe 3**
Calculate
($P_{3,out}$, $T_{3,out}$)

**Precooler**
Calculate
($P_{1,in}$, $H_{1,in}$, $Q_{Precooler}$)

B

$\left| \dfrac{(m_{cal.} - m_{ass.})}{m_{cal.}} \right| <$ Eps.  N

Y

B

$\left| \dfrac{[\Delta P]_n - [\Delta P]_{n-1}}{[\Delta P]_n} \right| <$ Eps.  N

Y

Print Results

Stop

**Figure 2-13. Flowchart of system analysis**

48

The $CO_2$ properties were calculated by utilizing NIST Refprop 7.0 database (Lemmon et al., 2002). As the NIST Refprop interface for calling the database, a code which was written by L. Vamling at the Chalmers University of Technology and modified by J. Lux of German Aerospace Center was adopted (Lemmon et al., 2007).

Figure 2-14 illustrates temperature and entropy diagram of the computational analysis. By considering the pressure drop of piping system a 42.50% efficiency can be attained. The total pressure drop of piping system is 434.76 kPa with 124.28 kg/s total mass flow rate.
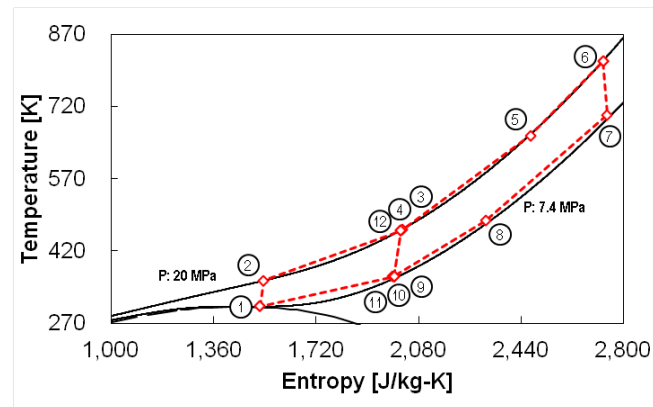


**Figure 2-14.** *T-s* **diagram**

# 3. ENGINEERING OF COMBINED VALVE FOR POWER CONVERSION SYSTEM

## 3.1. Introduction

The 21$^{st}$ century power plant market calls for ever higher performance as well as reduced footprint. The requirements of highly flexible and efficient power conversion systems and low investment costs have resulted in a modular design concept including the emergency stop and governing valves for controlling the fluid flow to turbine. The turbine converts the kinetic energy to mechanical energy in the power conversion system. Electricity from the generator is proportional to the mass flow rate of high pressure steam which is created from a boiler or a steam generator. The turbine system itself comprises fast acting governing control valves and stop valves acting against the seat in the flow passage in the closed position. The control valve is a type of pressure relief valve regulating the steam flow rate entering the first nozzle of turbine. The main function of the stop valve is to rapidly close the fluid inlet valve in response to a fast close signal to swiftly cut off the flow through the inlet valve. Both these valves significantly contribute to improvement of the power system transient stability using fast valving as well (Patel, 2001). Unfortunately, however, the existing turbine valves contributed to the initial pressure decrease in the turbine system by 5-7% (Zaryankin et al., 2003). Consequently, this number will cut down the power conversion system efficiency too.

Considering the power conversion system efficiency, many researchers have been investigating how to achieve high efficiency by focusing on the cycle layout or by improving the flow path of the working fluid. Polyzakis et al. (2008) tried to find out the best option for combined cycle power plant by analyzing four different cycle configurations. The results showed that the gas turbine played a crucial role

because of its high turbine exhaust gas temperature and resulting high thermal efficiency of the bottoming steam cycle. This combination of a gas turbine with a steam turbine cycle appeared to be very successful in particular where natural gas is sufficiently available for electricity generation (Hountalas et al., 2012). Ishiyama et al. (2008) analyzed steam turbine cycle, helium turbine cycle and S-CO$_2$ turbine cycle for future power generation. The thermal efficiency was examined for the prototype fusion reactor where a low temperature divertor heat source was included. Fujii et al. (2007) focused on a different way to enhance the thermal efficiency. They proposed an efficiency enhancement by adopting the steam flow path improvement. Their paper presented that the role of aerodynamic loss in the secondary flow regions and in the boundary layers along the blade length becomes significant. Therefore an optimized reaction blade based on a design concept that takes such steam flow characteristics into account was proposed. Various another methods which are related to the steam path design on commercial steam turbine by utilizing three-dimensional steam path design concept were also discussed by Leyzerovich (2008). The main idea of these methods are to reduce the major losses in turbine stages such as the profile energy losses, secondary losses, and the losses with leakages of steam passing beyond the stage's rotating blades.

Albeit varying improvement approaches have been proposed to increase the economic efficiency of power turbines, most of them have not concerned the entire flow path of the turbine which is actually starting from the turbine valves and ending with the exhaust hood. In this point of view, more investigations on turbine valves, which are the starting points of steam flow path, are still required to optimize the power conversion system efficiency. From this point of view, an idea of combining the stop and control valve into one module should deserve an investigation for the increase in power efficiency. Generally, the stop and control valves are separately manufactured. The valve pressure drop and space requirement can be minimized and thus the power conversion system efficiency may as well be

improved by combining the valves into one module. The combined valve can be utilized in Rankine cycle as well as Brayton cycle power conversion systems. Realizing the benefit of this kind of valve, the recent design of commercial turbine tends to adopt the combined stop and control valve (Barinberg et al., 2011).

This chapter focuses on the computational and experimental analysis of the combined stop and control valve. Combined Airflow Regulation Analysis (CARA) is performed to check on the hydrodynamic characteristic, which is represented by flow coefficient characteristic, of the control valve in the combined valve. The CARA focuses on modeling and simulation using three-dimensional computer-aided design and engineering (CAD/CAE) tools for computational fluid and structural dynamics. Then the combined valve will be computationally analyzed to optimize flow characteristics. Air is selected as working fluid for this analysis. Also, an experimental investigation was performed as well via Combined Airflow Regulation Operation (CARO) experiment. The CARO flow characteristic curve is plotted by calculating the ratio of the calculated mass flow rate from the dedicated control valve to that from the combined valve. Based on the CARA/CARO outcome, a typical turbine system is simulated to show the improvement over the existing system by adopting the combined valve instead of the separated stop valve and control valve.

## 3.2. Combined Valve

The indispensable idea of combined valve is to reduce the valve pressure drop and space requirement. Different ideas of combined valves design were proposed in the literatures. Oberle (1974) firstly proposed a bell-shaped structure for combined emergency stop and control valve. However it had been found that the bell-shaped control valve has tendency to vibrate when it is in the throttled position. To solve this problem, a bulb-shaped control valve was proposed (Oberle, 1978).

Moreover, an outstanding characteristic of combined valve for blocking and adjusting the flow rate of the heating steam in a reheating steam turbine was demonstrated by Araki and Kuwashima (1984). Due to the fairly strong wake downstream characteristic in a fully open butterfly type valve, a combined version of this kind of valve was proposed by Clark et al. (1999). The basic idea of this proposed combined valve is to take advantage of a butterfly valve as a controlling valve located close to the turbine while preventing the flow disturbances from this valve from reaching the first stage of the turbine. A different valve arrangement for power plant was described by Gerdes et al. (2003). The proposed arrangement contains a shutoff valve and a control valve for shutting off and controlling a fluid flow through a housing outlet and also a bypass valve. Steenburgh et al. (2003) adopted a balance chamber and inlet bleed for enabling fast closure of the control valve to provide optimum flow characteristics of the combined valve. Considering its merit, this research uses the combined valve type as main reference. The typical design of the combined stop and control valve and its application are illustrated in Figure 3-1(a) and 3-1(b). This combined valve is similar to the combined reheat and intercept valve which is often used with commercial units (Boss, 1996). As depicted in Figure 3-1(a), the main stop valve and control valve are contained within the same valve casing and share the same seat as well. But the actuators, stems and disks are completely independent for protection and control purposes.
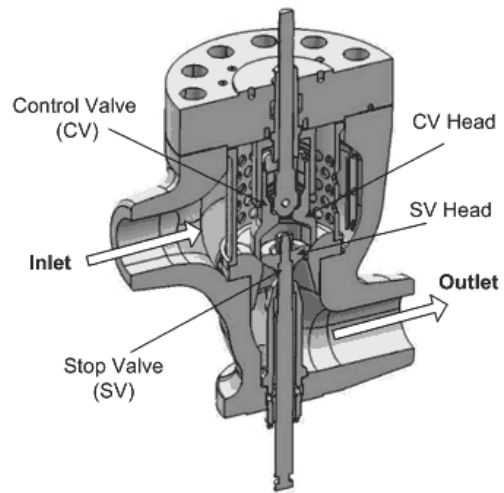
(a) Cross section
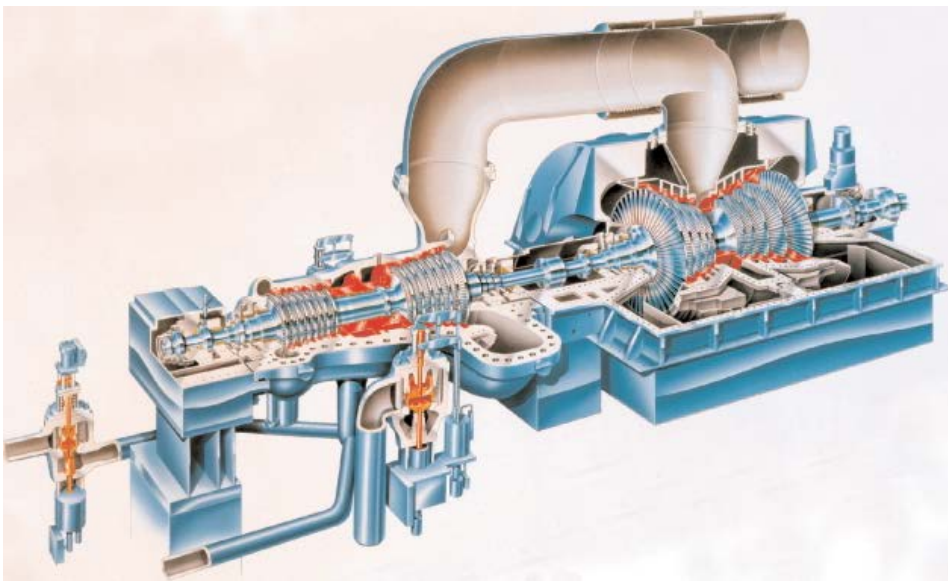


(b) Reheat steam turbine with combined valve (Chase and Kenhoe)

**Figure 3-1. Combined stop and control valve**

## 3.3. Flow Characteristic

Flow characteristic of a valve may be represented by valve flow coefficient. A standard method for measuring a valve flow coefficient for compressible and incompressible fluid is provided by the International Electrotechnical Commission (IEC, 1998). Basically the valve flow coefficient can be calculated by measuring upstream and downstream pressures and the corresponding flow rate. A numerous studies have been made to obtain flow characteristic curves by relying on analytical and numerical methods. Fu and Ger (1998) analyzed a method of determining a valve flow coefficient of a valve under compressible gas flow. They examined a ball valve and two diaphragm valves. Long and Guan (2011) adopted valve flow coefficient and resistance coefficient of an angle-seat valve to predict the fluid flow characteristic. Grace and Frawley (2011) presented a technique to predict valve coefficient for choke valve. The prediction method used a data trend based on a number of flow tests. Aragón-Camarasa et al. (2009) described a test bench to determine the flow coefficient process of control valve. The test bench was used to verify the calibration of the valves.

Considering practical and numerical applications, a combined valve flow coefficient which relies on physical fluid in the combined valve and theoretical mass flow rate is adopted in this research. A similar method was adopted to analyze mass flow rate of a dedicated turbine control valve (Yoo and Suh, 2011). Pirouzmand et al. (2010) used this method to check on the effect of differing seat shape to control valve flow coefficient. The theoretical mass flow rate function is calculated using the theoretical velocity which is expressed utilizing the relation between the enthalpy and the kinetic energy as (White, 2003; Yoo and Suh, 2011)

$$m = A \sqrt{2 \frac{\gamma}{\gamma-1} \frac{p_o}{v_o} \left[ 1 - \left( \frac{p_e}{p_o} \right)^{\frac{\gamma-1}{\gamma}} \right] \left( \frac{p_e}{p_o} \right)^{\frac{2}{\gamma}}} \qquad (3\text{-}1)$$

A dimensionless function being defined by $\psi$, Eq. (3-1) may be rewritten as

$$m = A\psi \sqrt{\frac{p_o}{v_o}} \qquad (3\text{-}2)$$

Equation (3-2) cannot be applied directly to the computer program and experiment since it does not consider the physical behavior of fluid in the valve. The measured flow rate must be included in Eq. (3-2). A flow coefficient $FC$ is defined as the ratio of the measured to theoretical mass flow rate to physically imply the pressure loss in valve as follows

$$FC = \frac{m_a}{A\psi \sqrt{\frac{p_o}{v_o}}} = \frac{m_a}{m_t} \qquad (3\text{-}3)$$

## 3.4. Numerical Analysis

The numerical analysis code CARA is mainly performed to check on the hydrodynamic characteristics of the control valve in the combined valve. A 2:1 linear scaled down model of the combined valve prototype is adopted for this analysis as described in Table 3-1. In the previous study, the experimental results showed that different scaled models of valve prototype do not significantly affect the valve flow coefficient (Yoo and Suh, 2011). In this analysis, a full three-dimensional CAD work of the combined valve is firstly done by CATIA. Computational fluid dynamic (CFD) analysis is then performed by CFX. The CFD codes are very reliable and can be used extensively in the design stage of control valves (Amirante et al., 2006). The air at room temperature ($25^o$C) is chosen as working fluid for this analysis. The irregularity, time-dependence and three-dimensionality of turbulence are analyzed by using the $k$-$\varepsilon$ two-equation model considering the accuracy, the level of description and also computational cost

(Zikanov, 2010). In the analysis, the no-slip boundary condition was applied at the wall. Heat transfer was not considered.

**Table 3-1. Combined valve model**

| | |
|---|---|
| Control valve | |
| Seat diameter (m) | 0.11115 |
| Max. stem lift (m) | 0.0277875 |
| Stop valve | |
| Seat diameter (m) | 0.09525 |
| Max. stem lift (m) | 0.0238125 |
| Stem diameter (m) | 0.028475 |
| Inlet diameter (m) | 0.10795 |
| Outlet diameter (m) | 0.10795 |

For determining the flow coefficient, the numerical results were used as actual mass flow rates. The theoretical ones can be obtained by using Eq. (3-1). The mass flow rate coefficient was then calculated based on Eq. (3-3). The boundary condition of the numerical analysis is provided in Table 3-2. All analysis cases were run with $10^{-4}$ in convergence criterion and 5.0% in turbulence intensity on both inlet and outlet sides.

**Table 3-2. Boundary condition**

| Boundaries | Input Properties |
|---|---|
| Inlet condition | Total temperature and static pressure |
| Outlet condition | Static pressure |

Before executing the numerical analysis, a sensitivity study was performed to

obtain an optimum result. Table 3-3 tabulates the sensitivity test for pressure ratio $p_e/p_o = 0.8$ and normalization ratio $L/D = 0.15$. Considering the calculated result and cost in term of running time, the 6 mm in maximum mesh face size is a reasonable choice for combined valve flow coefficients calculation. Figure 3-2 presents one of the generated meshes in numerical work. To obtain more sufficiently fine meshes around the outlet passage wall section where the flow will rapid change in key variables, a refined computational grid was implemented by adopting a smooth transition inflation layer meshing as illustrated in Figure 3-3. The transition ratio is set at 0.272 value and the maximum layer number is 5.

**Table 3-3. Meshing sensitivity**

| Max. Face Size [mm] | Number of Mesh $(x10^4)$ | Mass Flow Rate [kg/s] | Running Time [h] |
|---|---|---|---|
| 15.0 | 62 | 1.21309 | 0.42 |
| 9.0 | 118 | 1.29176 | 0.70 |
| 6.0 | 155 | 1.27018 | 0.90 |
| 5.0 | 197 | 1.28483 | 1.12 |
| 4.5 | 236 | 1.27108 | 1.34 |

**Figure 3-2. Combined valve meshing**
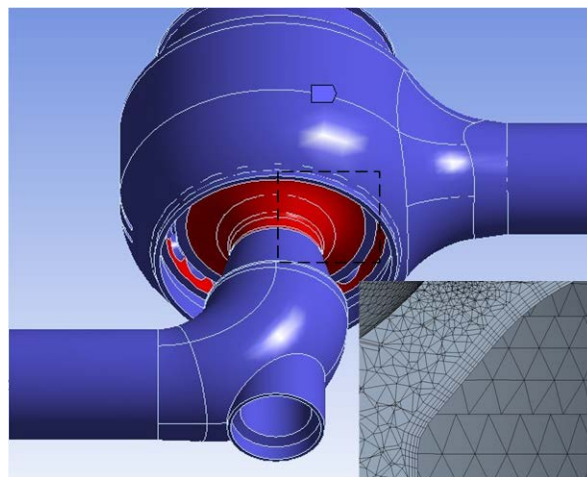


**Figure 3-3. Refined meshing**

Based on the sensitivity study result, the numerical analysis was performed. First of all, the stem lift is normalized to obtain the flow coefficient. The normalized value is defined as $L/D$, i.e. the actual lift height divided by the seat diameter. The mass flow rate was calculated at each given pressure ratio $p_e/p_o$. The computational fluid dynamic analysis was made for the pressure ratios of 0.6, 0.7, 0.75, 0.80, 0.85, 0.9 and 0.95, and the $L/D$ ratios of 0.04, 0.06, 0.08, 0.10, 0.12, 0.14, 0.18, and 0.25.

Figure 3-4 depicts the pressure contour and streamline in the combined valve for the selected pressure ratio $p_e/p_o = 0.9$ and ratio $L/D = 0.25$. This figure illustrates how the annular screen, which is designed to reduce flow blockage and vortex formation, directs the fluid passing through the valve to the outlet passage. The fluid pressure inside the annular screen can be kept almost equalized with the inlet as represented in the pressure contour. The velocity, around the outlet passage showed higher values compared to the others as illustrated in Figure 3-4 (b).

The numerical analysis was run for all pressure ratio and $L/D$ values. The theoretical mass flow rate can be obtained by adopting Eq. (3-2). Then, by using Eq. (3-3) the flow coefficient of combined valve can be easily calculated for certain pressure ratios and $L/D$ values. This sequence is repeated for all pressure ratio and $L/D$ values. Figure 3-5 plots the flow coefficient based on this numerical analysis. As shown in Figure 3-5, the flow coefficient does not change significantly over the $L/D$ ratios of 0.18 through 0.25. This may as well be attributed to the valve almost in the wide open position. Thus, differing $L/D$ values may not necessarily change the flow coefficient.
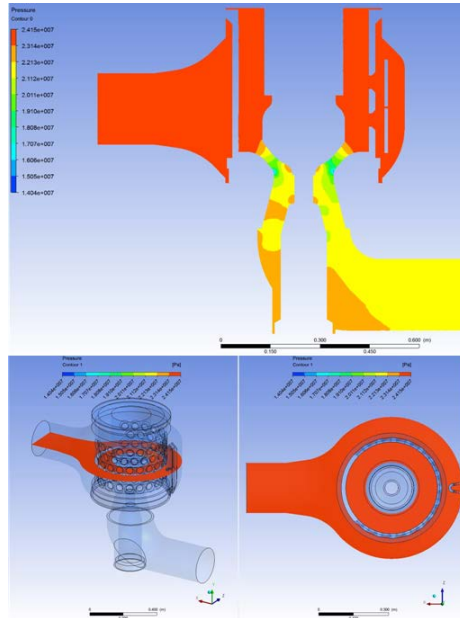
(a)
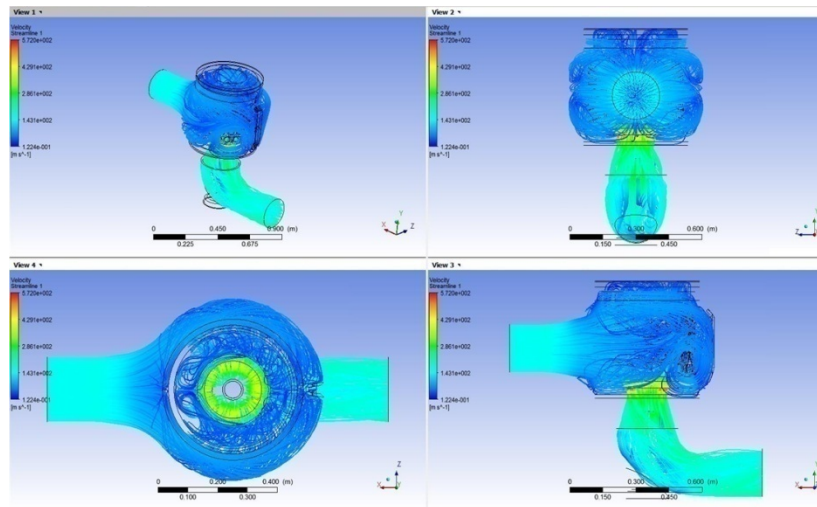


(b)

**Figure 3-4. CFD analysis (a) pressure contour (b) streamline**
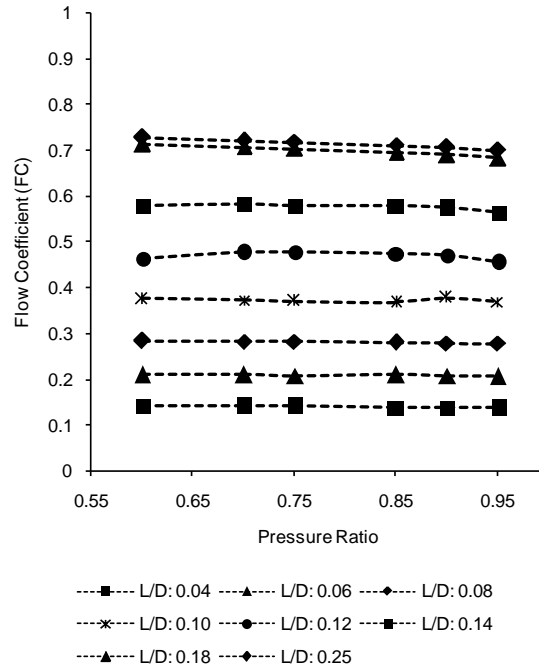
**Figure 3-5. Combined valve flow coefficient by CFX**

## 3.5. Experimental Analysis

The CARO test is performed pursuant to the CARA analysis. Air is selected as working fluid in CARO. The CARO flow characteristic curve is plotted by calculating the ratio of the calculated mass flow rate from the dedicated control valve to that from the combined valve. The CARO experimental setup is illustrated in Figure 3-6. An air tank is utilized as air reservoir. This reservoir is supplied by an air compressor with 2 bar maximum pressure capacity. The up- and downstream-pressures are measured by a diaphragm type CoplanarTM differential, gage and absolute Rosemount 3051S2CD pressure transmitters. They have performance up to 0.025% accuracy and 200:1 range-down. The volumetric flow rate is measured by a vortex flow meter with accuracy, the maximum pressure and

flow rate of 1%, 5 MPa and 1100 m³/hr, respectively. The average upstream temperature is measured by four K-type thermocouples. All measurement instruments are connected to a personal computer (PC) via data acquisition system. The stop valve is always fully open. The pressure transmitters and flow meter are calibrated prior to the experiment.
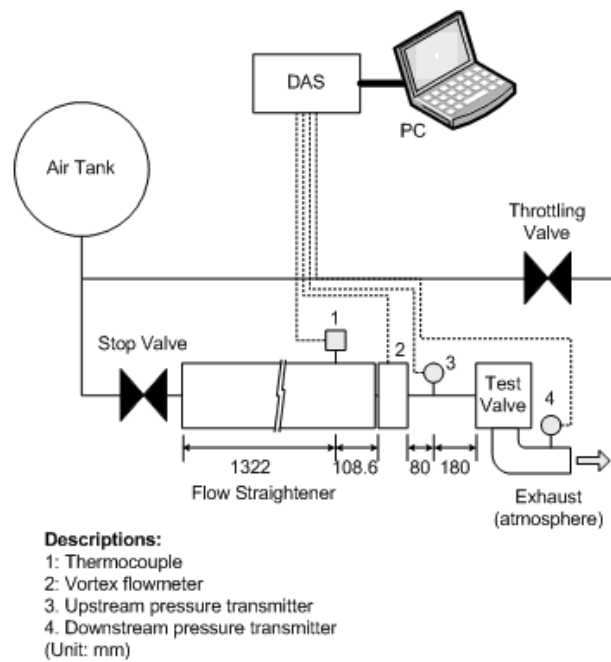


**Figure 3-6. Experimental setup, CARO**

The experimental procedure is as follows

1. Set stem lift of the test valve on a desired *L/D* value

2. Compress a certain amount of air to the air tank

3. Set the stem position of the throttling valve to obtain a specific pressure ratio value

4. Measure and record the upstream and downstream pressures, volumetric

flow rate, and temperature

5.  Repeat steps 3 and 4 for varying pressure ratios

6.  Repeat steps 1 through 5 for differing *L/D* values.

Figure 3-7 plots the flow coefficient based on the experimental investigation for various *L/D* values. Note that the computational results agree well with the experimental data. Experimentally, due to the capacity of the compressor, however, the low pressure ratio cases are difficult to be run for certain *L/D* values. The experiment is performed for *L/D* = 0.04 to 0.10 for various pressure ratios.
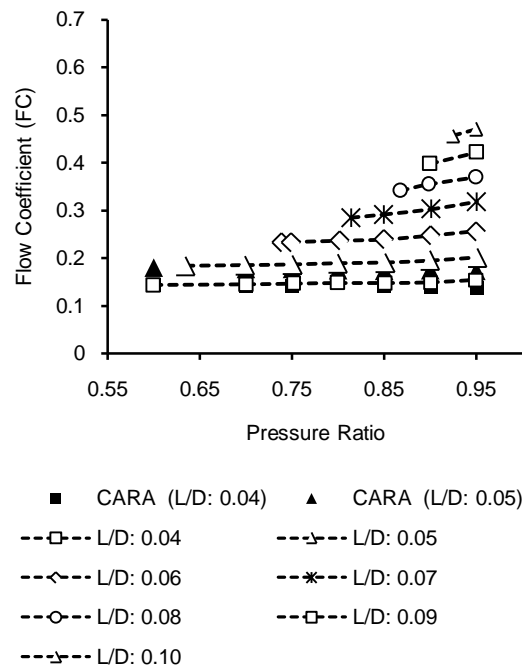


**Figure 3-7. Comparison of numerical and experimental results**

To quantify the magnitude of the dependency of the flow coefficient on its parameters for CARO test results, the finite difference technique is adopted as well

for sensitivity analysis (De Pauw and Vanrolleghem, 2006). It is demonstrated that the temperature and flow rate do not as much affect the flow coefficient calculation results as the pressure. Moreover, the uncertainty of the CARO test can be calculated considering the accuracy of the experimental transducers. Due to the nonlinearity of the correlation of flow coefficient, the result-perturbation technique is chosen for the uncertainty analysis (Holman, 2001). The flow coefficient uncertainty is defined as follows

$$\varpi_{FC} = \left[ \left( \frac{\partial FC}{\partial T} \varpi_T \right)^2 + \left( \frac{\partial FC}{\partial P_{in}} \varpi_{P_{in}} \right)^2 + \left( \frac{\partial FC}{\partial P_{out}} \varpi_{P_{out}} \right)^2 + \left( \frac{\partial FC}{\partial Q} \varpi_Q \right)^2 \right] \qquad (3\text{-}4)$$

where $FC$ is the flow coefficient function; and $\varpi_T, \varpi_{P_{in}}, \varpi_{P_{out}}$, and $\varpi_Q$ are respectively the uncertainties in temperature, inlet pressure, outlet pressure and volumetric flow rate measurements.

Table 3-4 presents the uncertainty analysis of the CARO test results for each $L/D$. All the test results fall within 1% of the uncertainty. Considering the maximum value, the $L/D = 0.10$ gives the greatest uncertainty by 0.004511 or 0.90%.

**Table 3-4. Uncertainty analysis result**

| Experiment | Max. Uncertainty Value |
|---|---|
| $L/D = 0.04$ | 0.001610 |
| $L/D = 0.05$ | 0.002118 |
| $L/D = 0.06$ | 0.002645 |
| $L/D = 0.07$ | 0.003254 |
| $L/D = 0.08$ | 0.003694 |
| $L/D = 0.09$ | 0.004131 |
| $L/D = 0.10$ | 0.004511 |

## 3.6. Application to Steam Turbine System

To check on turbine system improvement by taking the benefit of combined valve, an additional analysis is required. Generally, a turbine system consists of a steam generator or boiler, stop valves, control valves and a turbine. Each component is connected by piping as depicted in Figure 3-8(a). By adopting a combined valve, the system will be simpler as shown in Figure 3-8(b).
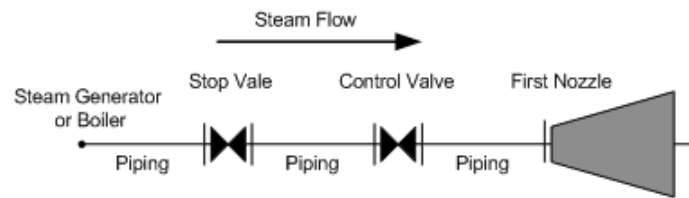


(a) Conventional system
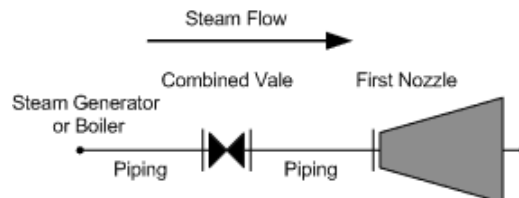


(b) Combined valve system

**Figure 3-8. Scheme of turbine system**

The steam generator or boiler produces steam. The stop valve will shut off the steam flow in an abnormal condition. The steam flow is regulated by the control valve. Differently from the conventional system the stop valve and control valve are integrated into one valve module in the combined valve system. Both of these system configurations are analyzed by an in-house computer code. For the

conventional system the pressure drop has to be calculated in the stop valve as well as in the piping between the stop valve and control valve. The computational procedure for the system with the combined valve is similar to that for the conventional system.

Firstly, a typical turbine system with conventional separated stop valve and control valve was analyzed. In this analysis the steam enthalpy and pressure of steam generator or boiler are assumed to be constant as presented in Table 3-5. The working mechanism of the stop valve is similar to that of the control valve except that it is wide open during the normal condition. Thus, the mass flow rate coefficient of the stop valve can be expressed as a single value which depends on the valve type. For this case, if the inlet and outlet pressures are known, the actual mass flow rare can readily be found. To calculate the pressure drop in the pipe, the following correlation is used

$$p_i - p_e = \frac{flV^2}{2vd} \qquad (3\text{-}5)$$

**Table 3-5. System parameters**

| Parameter | Value |
|---|---|
| Throttle pressure (MPa) | 24.23 |
| Throttle enthalpy (kJ/kg) | 2.32 |
| Throttle specific volume (m$^3$/kg) | 0.0128 |
| Stop valve flow coefficient | 0.627 |

This analysis explores a turbine with two stop valves and four control valves as a reference. All the stop valves are fully open during the normal condition. The same partial admission opening mechanism of the control valves is adopted for the conventional system and the combined system. The first and second control valves

are first opened together. Once both the valves are fully open, the third and fourth valves are sequentially opened. In a simplistic way, this opening sequence can be written as #1, #2➔ #3➔#4. The calculation assumes that the four valves are identical. The control valve prototype from General Electric (GE) is used as a reference for the conventional system (Yoo and Suh, 2011).

The second analysis investigates the typical turbine system with combined valves. The valve admission is the same as the first case. The flow characteristic of the combined valve relies on the previous CARA/CARO analysis. Figure 3-9 and 3-10 show the results of the computational mass flow rate turbine system with combined valve and comparison both analysis cases, respectively. The horizontal axis (step) represents the step of the valve stem lift. Based on the combined valve case simulation, the steady state mass flow rates of valves #1 through #4 are 114.62, 123.87, 124.41 and 117.91 kg/s, respectively. The total flow rate is 480.81 kg/s. In the conventional system, the steady state mass flow rate is 474.70 kg/s. The total pressure drops are about 1.48% and 2.72% for the combined valve and conventional system, respectively. From the efficiency, which is generally defined as the ratio of output and input, point of view the combined valve can reduce the pressure drop in the turbine nozzle inlet by 1.24%. Also, the output power is increased by 1.27% by assuming a linear relationship between steam mass flow rate and output power. This improvement will be much higher for a higher power as illustrated in Figure 3-11.
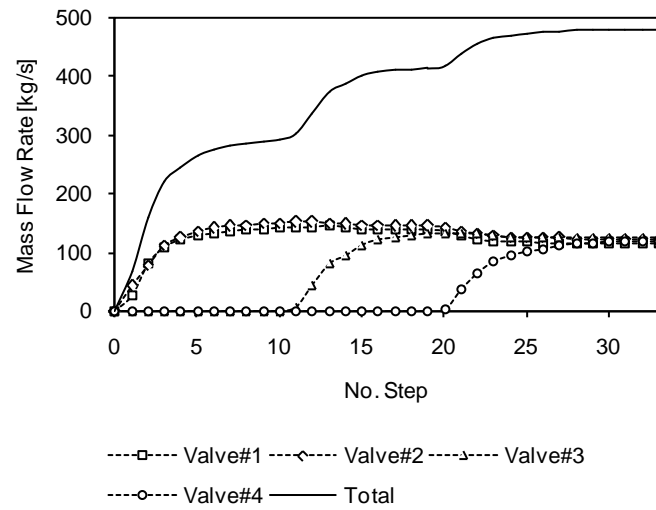
**Figure 3-9. Mass flow rate by opening sequence of combined valve**
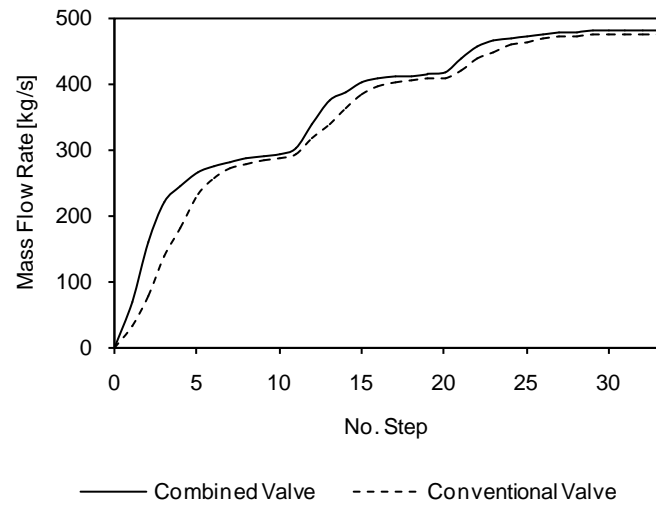


**Figure 3-10. Conventional system and combined valve system**
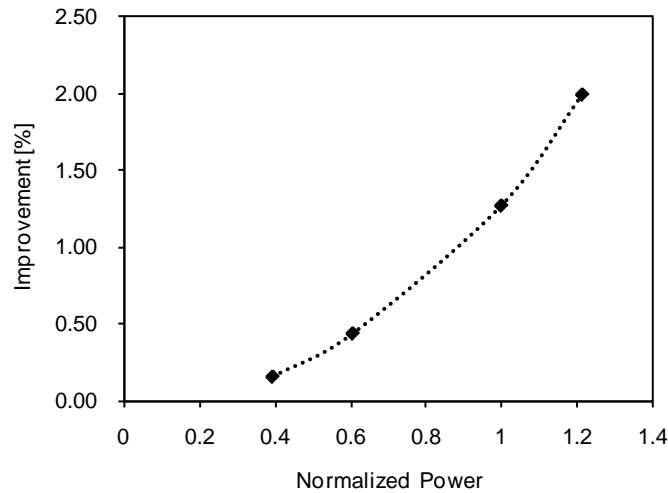
**Figure 3-11. Efficiency improvement as function of power**

## 3.7. Application to Recompression S-CO$_2$ Brayton Cycle

It is different from the steam Rankine cycle, the power control using control valves for S-CO$_2$ recompression cycle has been actively under investigated (Dostal et al., 2006a; Moisseytsev and Sienicki, 2008). Dostal et al. investigated two possibilities, inventory (pressure) control and bypass control, for power control as illustrated in Figure 3-12 (2006a). In the case of pressure control, the pressure ratio is held constant. In order to match the power demand, the mass flow rate is reduced. For bypass control, part of the flow bypasses the turbine. There are two possible locations of the bypass valve. It can be put after the recompressing compressor and merge it at the outlet of HTR or located at the return duct to the reactor and merge it at the turbine outlet. In order to keep the flow split constant, the throttling valve was proposed to be located on the HTR inlet side instead of both compressor inlet sides.

Another control mechanism was proposed by Argonne National Laboratory for

STAR-LM power conversion system (Moisseytsev and Sienicki, 2008). As presented in the previous chapter, the STAR-LM is a 181 MWe (400 MW) autonomous load following, natural circulation lead-cooled fast reactor (LFR) concept which is coupled to S-CO$_2$ Brayton cycle as power conversion system. The power conversion system adopts an in-reactor heat exchanger bypass valve, a turbine inlet valve, a turbine bypass valve, an inventory control system, and a flow split valve for controlling the cycle as shown in Figure 3-13.
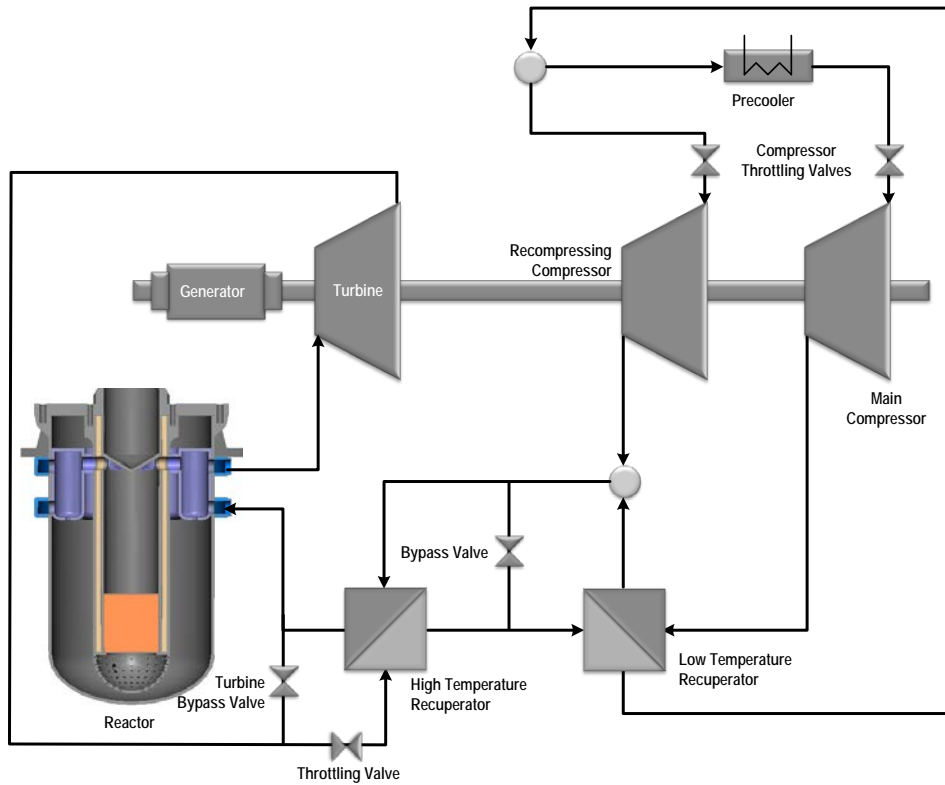


**Figure 3-12. Possible location of throttling and bypass valves**
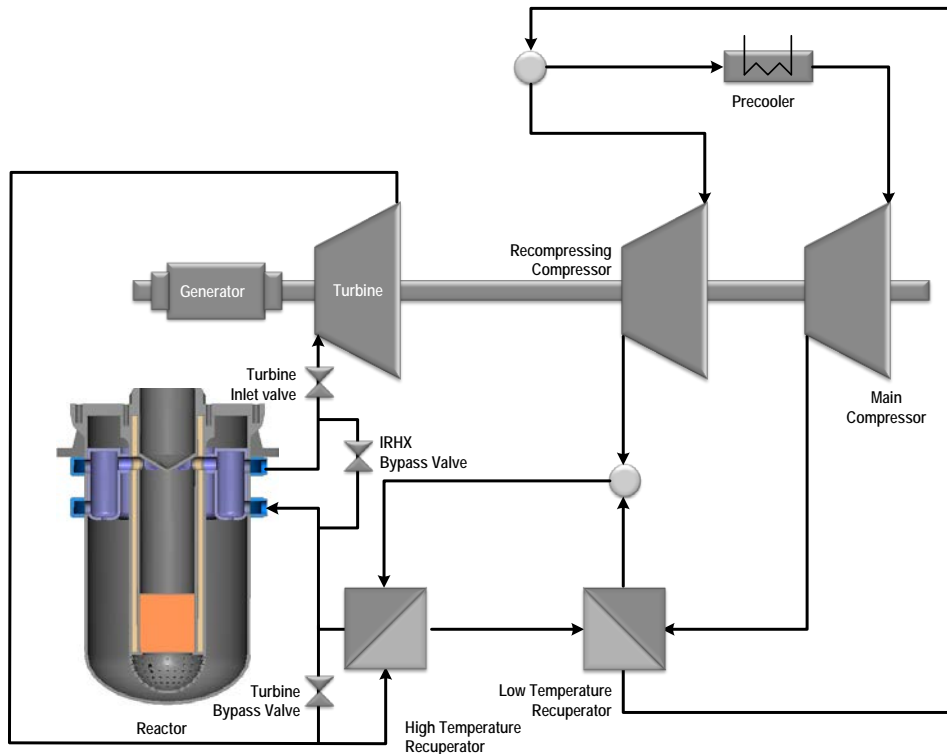
**Figure 3-13. STAR-LM S-CO₂ Brayton cycle control mechanism**

In recompression Brayton cycle, the parallel compressor configuration makes the control mechanism more complicated. To solve this, several valves are proposed as main control components of the power conversion system in the dynamic response of recompression Brayton cycle code which developed by MIT as depicted in Figure 3-14 (Trinh, 2009). A turbine upstream throttle and turbine bypass valve are utilized to control the turbine power during steady state and transient scenarios and to bypass flow around the turbine in the event of loss of external load (LOEL), respectively. Similar to the turbine bypass valve, the IHX/turbine bypass valve will open to bypass flow around the turbine and IHX in the case of LOEL.
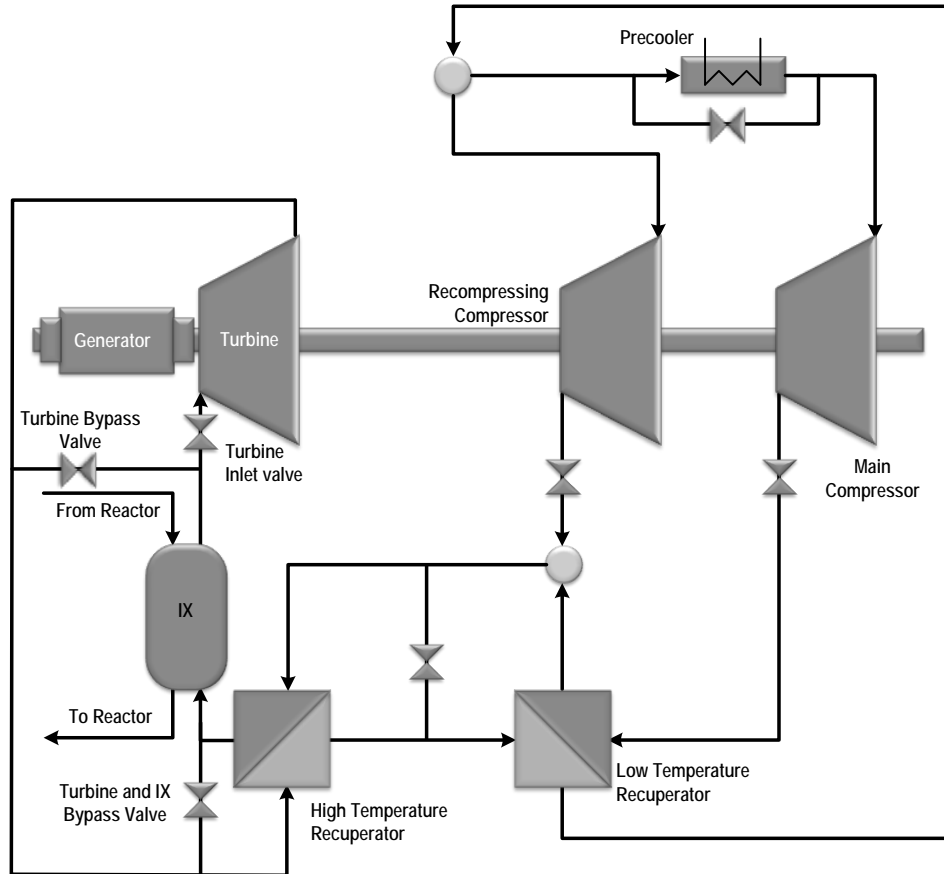
**Figure 3-14. Valve controls of recompression cycle**

### 3.7.1. Flow Coefficient of Combined Valve with S-CO₂ Flow

In a recompression S-CO$_2$ Brayton cycle, the combined valve will replace the conventional turbine upstream throttle valve to regulate the turbine power. Because the working fluid is in supercritical state, it is necessary to check on its deviation from ideal gas behavior. The compressibility factor was investigated first to evaluate the CO$_2$ behavior as follows

$$z = \frac{PV}{RT} \qquad\qquad (3\text{-}6)$$

To refine theoretical mass flow rate in the previous flow coefficient equation, a correction factor was introduced (Younger, 2004) by adding compressibility factor as follows

$$m_{t_{S-CO_2}} = A \sqrt{2 \frac{\gamma}{\gamma-1} \frac{p_o}{z v_o} \left[1 - \left(\frac{p_e}{p_o}\right)^{\frac{\gamma-1}{\gamma}}\right] \left(\frac{p_e}{p_o}\right)^{\frac{2}{\gamma}}}$$  (3-7)

Thus the flow coefficient of combined valve with S-CO$_2$ working fluid can be calculated as follows

$$FC_{S-CO_2} = \frac{m_a}{m_{t_{S-CO_2}}}$$  (3-8)

Based on Eq. (3-7) and (3-8), the compressibility factor will contribute to flow coefficient value in square root form. To check on this contribution, the deviation from ideality of the working fluid is firstly investigated. Figure 3-15 shows the square root of compressibility factor of CO$_2$ gas in various temperatures values. This figure shows that the compressibility factor will insignificantly contribute to flow coefficient of the combined valve. Moreover, as turbine throttle valve, the operation point of combined valve working fluid will be quite far from the critical point and the variance of its properties will be very small as well.
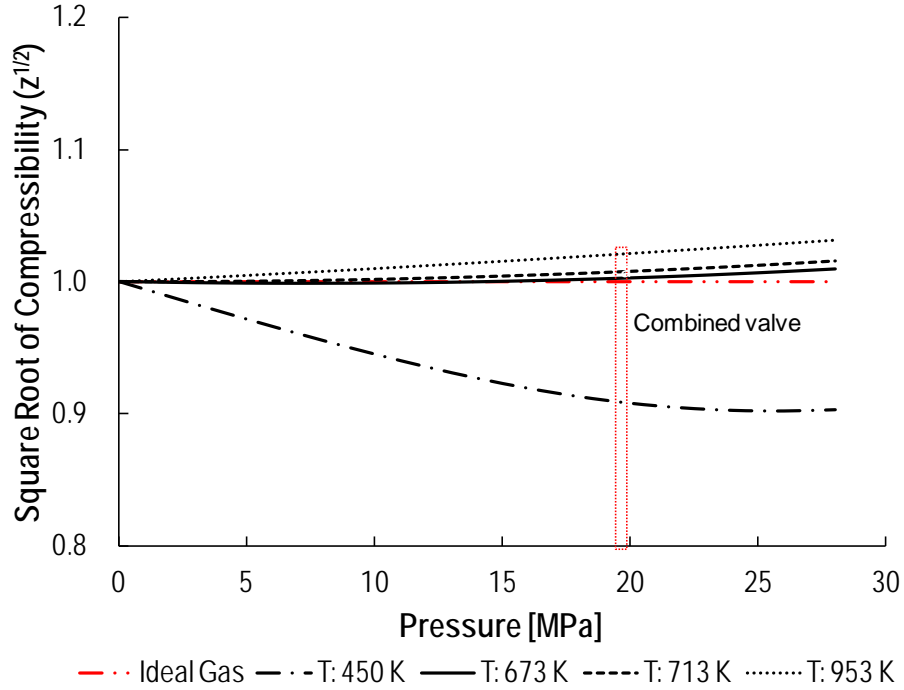
**Figure 3-15. Deviation of CO$_2$ from ideality**

As discussed in the previous chapter, the CATIA software is utilized to generate a full three-dimensional CAD of the combined valve. CFD analysis is then performed by CFX with S-CO$_2$ as working fluid. Considering the accuracy, the level of description and also computational cost, the irregularity, time-dependence and three-dimensionality of turbulence are analyzed by using the $k$-$\varepsilon$ two-equation model.

The CFD analysis was made in three different inlet pressure and temperature working points (P: 19.50 MPa, T: 673.15 K; 19.50 MPa, 953.15 K; 24.50 MPa, 713.15 K) for pressure ratios of 0.6, 0.7, 0.75, 0.80, 0.85, 0.9 and 0.95, and *L/D* ratios of 0.04, 0.06, 0.08, 0.10, 0.12, 0.14, 0.16, 0.20, and 0.25. By adopting Eq. (3-3), calculated flow coefficient can be obtained easily for certain pressure ratios and

*L/D* values. Figure 3-16 and 3-17 depict the pressure contour and streamline in the combined valve with S-CO$_2$ flow for pressure ratio $p_e/p_o = 0.7$ and ratio *L/D* = 0.10.

Figure 3-18 through 3-20 demonstrate the combined valve flow coefficients values for case 1, 2, and 3, respectively. In all cases, the flow coefficient does not change significantly over the *L/D* ratios of 0.20 through 0.25 at same pressure ratio value. This may as well be attributed to the valve almost in the wide open position. Thus, differing *L/D* values may not necessarily change the flow coefficient *FC*. Also, the different inlet pressure and temperature working points do not significantly affect flow coefficient of the valve especially in low *L/D* values region as shown in Figure 3-21.
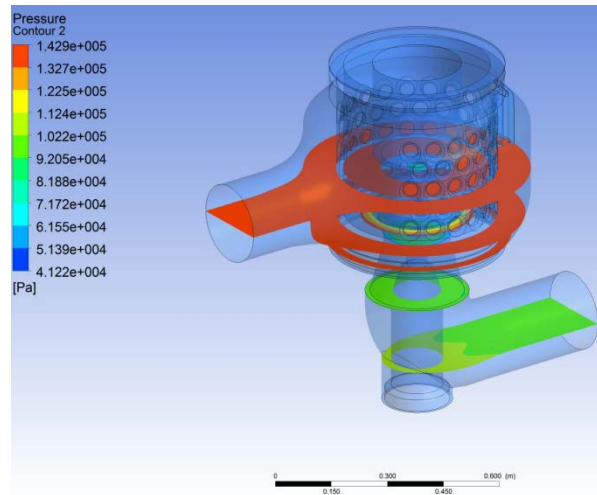


**Figure 3-16. Pressure contour of combined valve with S-CO$_2$ flow**
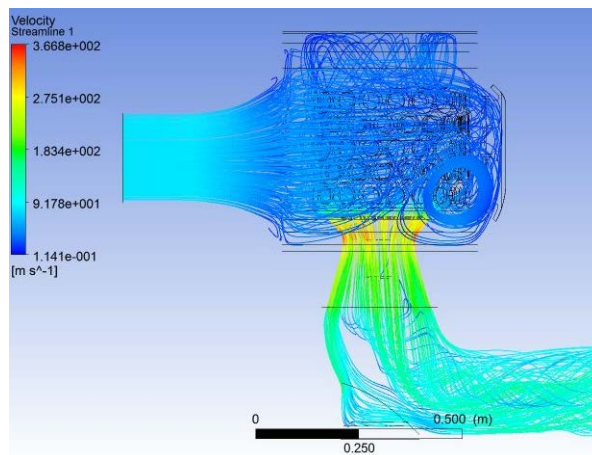
**Figure 3-17. Velocity streamline of combine valve with S-CO₂ flow**
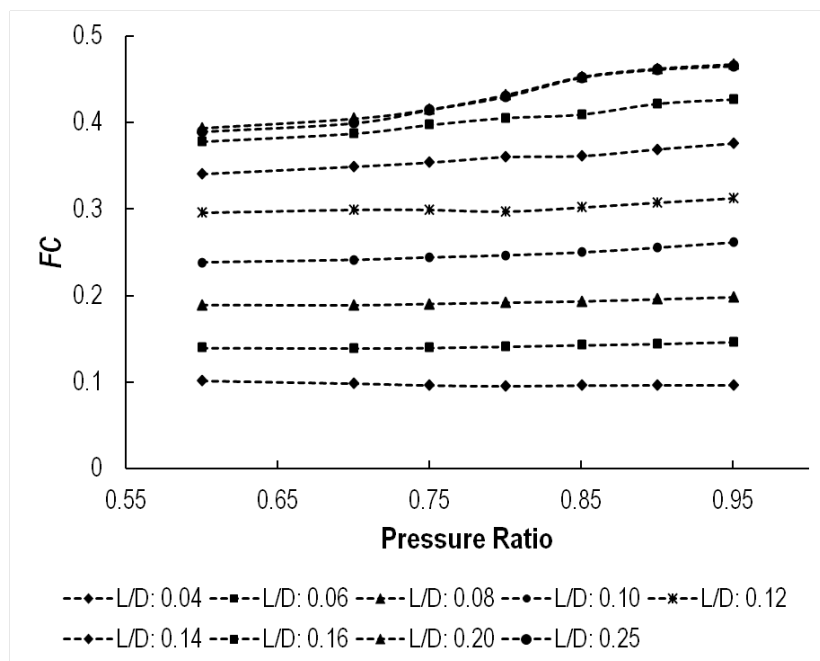


**Figure 3-18. Case 1 (P: 19.50 MPa, T: 673.15 K)**
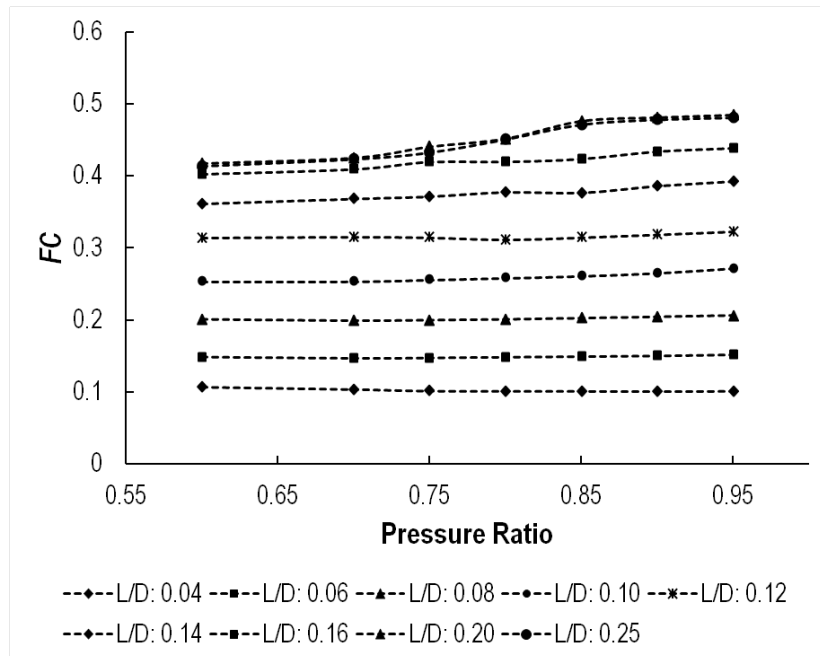
**Figure 3-19. Case 2 (19.50 MPa, 953.15 K)**
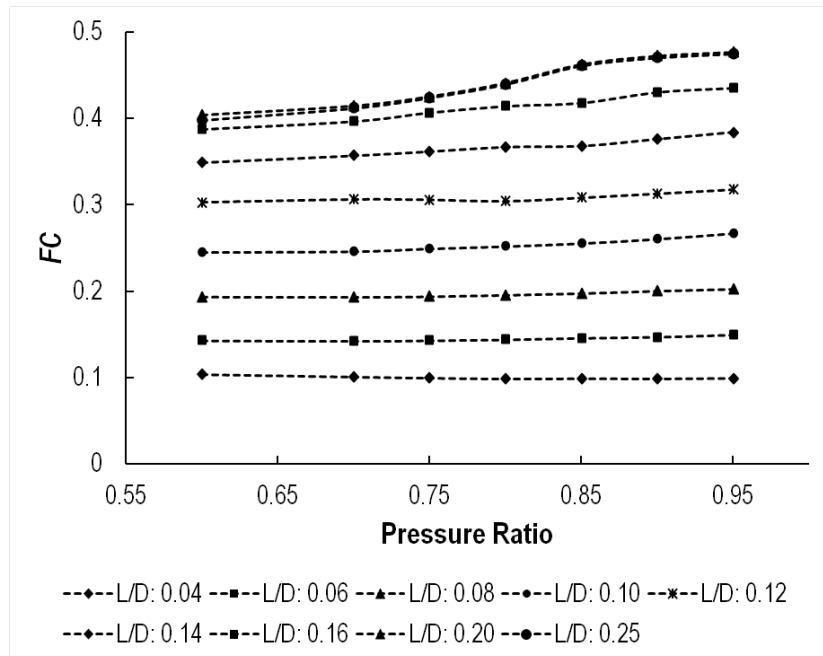
**Figure 3-20. Case 3 (24.50 MPa, 713.15 K)**
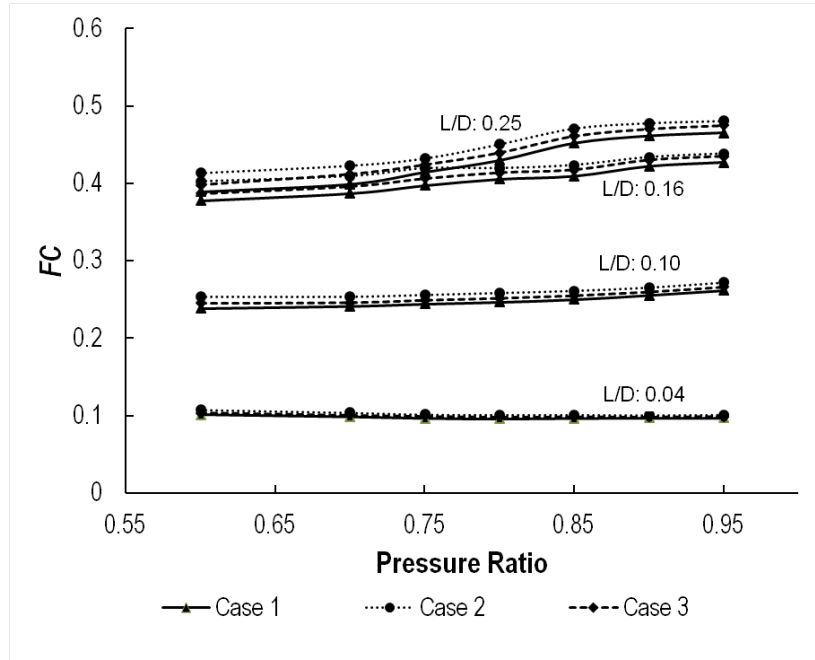
**Figure 3-21. Flow coefficient at various working points**

### 3.7.2. S-CO$_2$ Recompression Brayton Cycle with Combined Valve

Two scenarios are selected to investigate the application of combined valve on S-CO$_2$ recompression Brayton cycle. The first scenario is illustrated in Figure 3-22. In this case, a conventional configuration of one stop valve and one control valve is adopted. The stop valve and turbine bypass valve are normally widely open and totally closed, respectively. Thus, as illustrated in the previous study case, the stop valve can be modeled as a constant *FC* value. Moreover, a replacement of the two valves, stop valve and control, with one combined valve is analyzed in the second scenario as depicted in Figure 3-23. The numbers in Figure 3-22 and 3-23 represent the new pipe section number in both scenarios. Due to its totally closed condition, the turbine bypass valve is currently not considered in computational analysis.

80
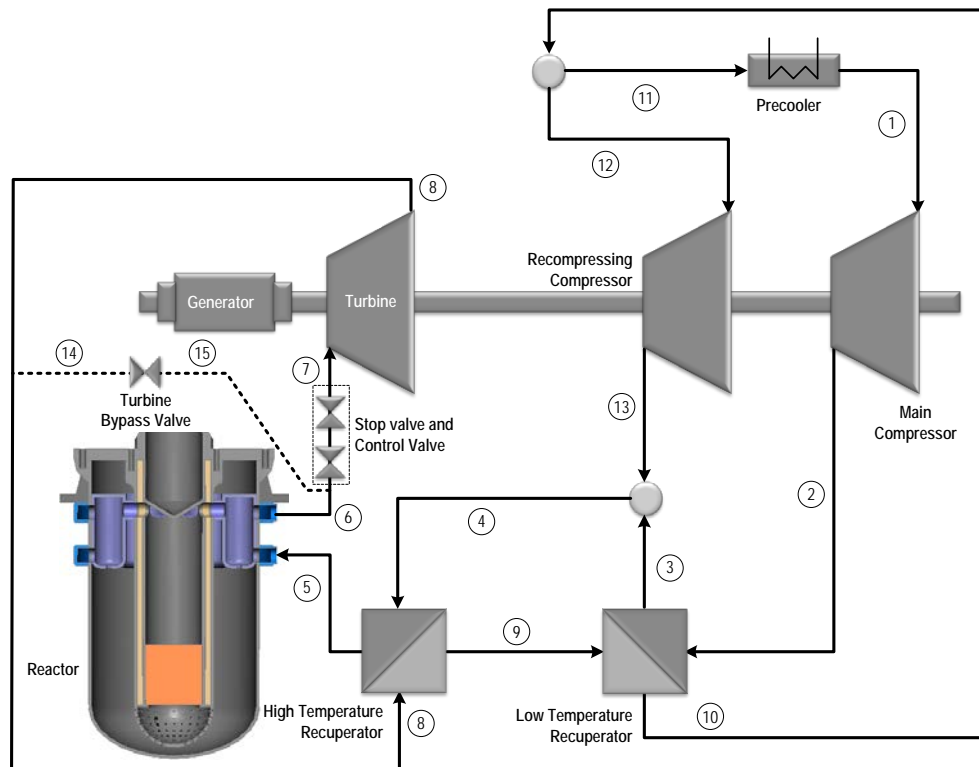
**Figure 3-22. Recompression Brayton cycle with stop and control valve**
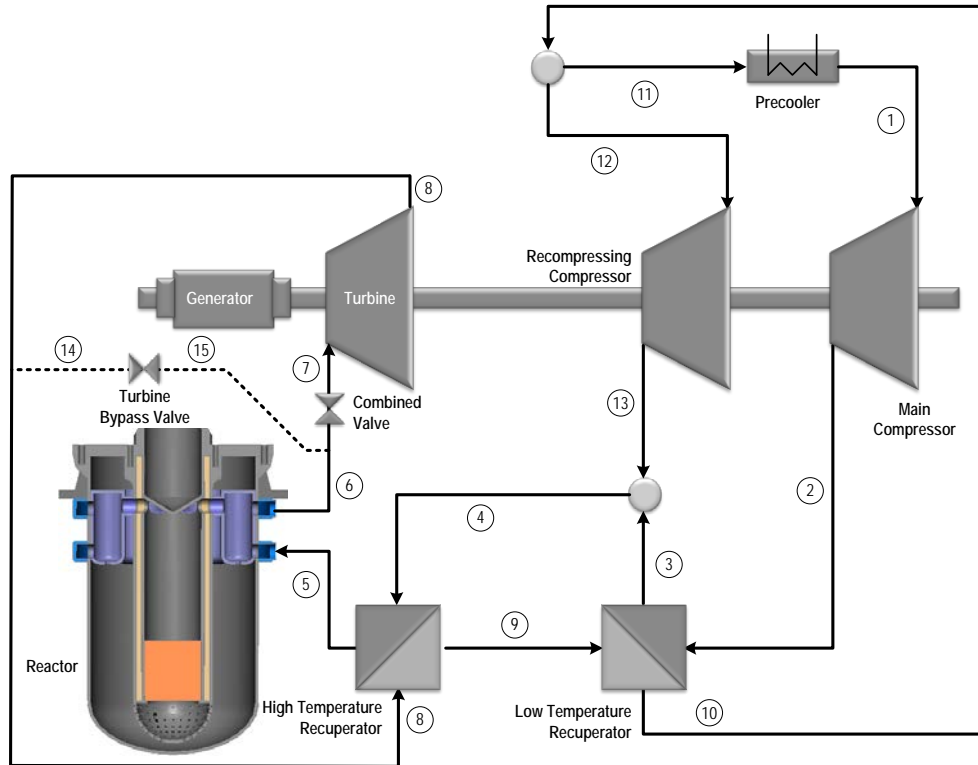
**Figure 3-23. Recompression Brayton cycle with combined valve**

The computational algorithm of both scenarios is basically similar with the previous developed code, as described in the previous chapter, except the additional valve subroutine as depicted in Figure 3-24. The valve pressure drop can be iteratively calculated as discussed in the previous sub chapter.

Start

Input Data

Assume mass flow rate
($m_{ass.}$) ← B

Pipe 1
Calculate
($P_{1,out}$, $T_{1,out}$)

Compressor 1
Calculate
($P_{2,in}$, $T_{2,in}$)

Pipe 10, 11, 12
Calculate
($P_{10,out}$, $T_{10,out}$, $P_{11,out}$, $T_{11,out}$, $P_{12,out}$, $T_{12,out}$)

Compressor 2
Calculate
($P_{13,in}$, $T_{13,in}$)

Pipe 6, 13
Calculate
($P_{6,out}$, $T_{6,out}$, $P_{13,out}$, $T_{13,out}$)

Valve
Calculate
($P_{7,in}$, $T_{7,in}$)

Turbine
Calculate
($P_{8,in}$, $T_{8,in}$)

Pipe 4, 8
Calculate
($P_{4,out}$, $T_{4,out}$, $P_{8,out}$, $T_{8,out}$)

HTR
Calculate
($P_{5,in}$, $T_{5,in}$, $P_{9,in}$, $T_{9,in}$, $Q_{HTR}$)

Pipe 5, 9
Calculate
($P_{5,out}$, $T_{5,out}$, $P_{9,out}$, $T_{9,out}$)

A

A

LTR
Calculate
($P_{3,in}$, $T_{3,in}$, $P_{10,in}$, $T_{10,in}$, $Q_{LTR}$)

Pipe 3
Calculate
($P_{3,out}$, $T_{3,out}$)

Precooler
Calculate
($P_{1,in}$, $H_{1,in}$, $Q_{Precooler}$)

$\left| \dfrac{(m_{cal.} - m_{ass.})}{m_{cal.}} \right| <$ Eps.  — N → B
Y

$\left| \dfrac{[\Delta P]_n - [\Delta P]_{n-1}}{[\Delta P]_n} \right| <$ Eps.  — N → B
Y

Print Results

Stop

**Figure 3-24. Computational flowchart of MOBIS with valve**

83

By inserting the conventional stop valve and control valve, the system was sacrificed by 0.92% to be 41.58% in term of its efficiency. These added valves contributed 352.48 kPa pressure drops. Fortunately, a great degree in term of the efficiency improvement can be said to combined one. By replacing the conventional one with combined valve, a 42.01% efficiency can be attained. Figure 3-25 and 3-15 show the *T-s* diagram of both valve configurations. The detail computational results are presented in Appendix B2 and B3
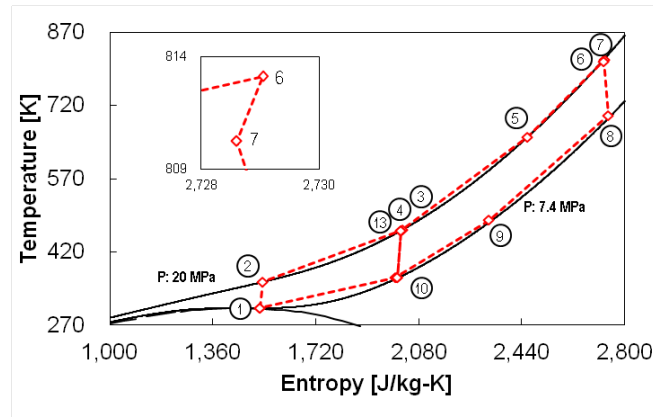


**Figure 3-25. *T-s* diagram of cycle with stop valve and control valve**
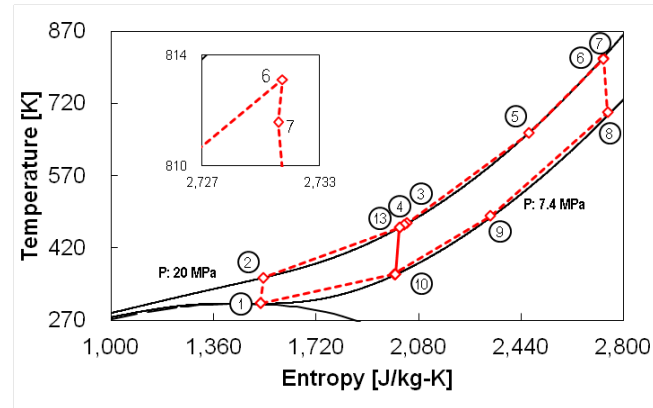


**Figure 3-26. *T-s* diagram of cycle with combined valve**

84

### 3.7.3. S-CO$_2$ Simple Brayton Cycle with Combined Valve

As presented in the previous subchapter, two scenarios are selected to illustrate the application of combined valve on S-CO$_2$ simple compression Brayton cycle. The simple S-CO$_2$ simple compression Brayton cycles with a separated stop valve and control valve and with a combined valve are illustrated in Figure 3-27 and 3-28, respectively. Based on these figures, the CO$_2$ fluid flows through turbine via the turbine valve(s) (SV-CV or combined valve) from the reactor heat exchanger and after that goes through the recuperator to transfer heat to cold-side fluid that comes from the compressor outlet. The CO$_2$ fluid nears its critical point as its temperature lowered in the precooler. From the precooler, the fluid pressure is raised by the compressor then passes through the cold-side of the recuperator before it goes back through the heat exchanger. The thermal efficiency improvement was analyzed computationally based on these both configurations.
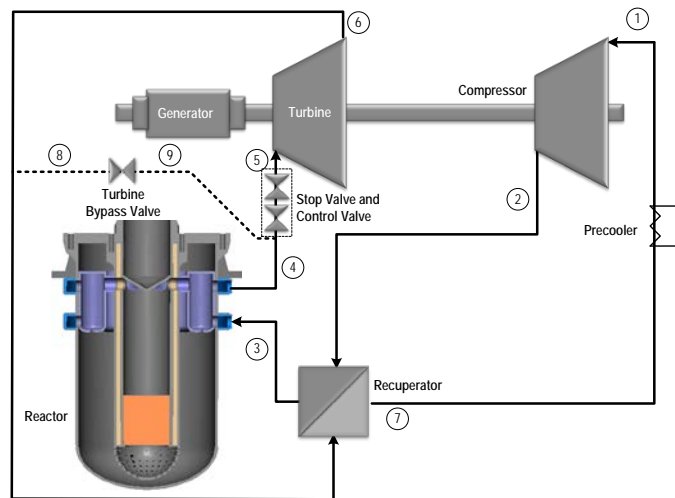


**Figure 3-27. Simple compression Brayton cycle without combined valve**
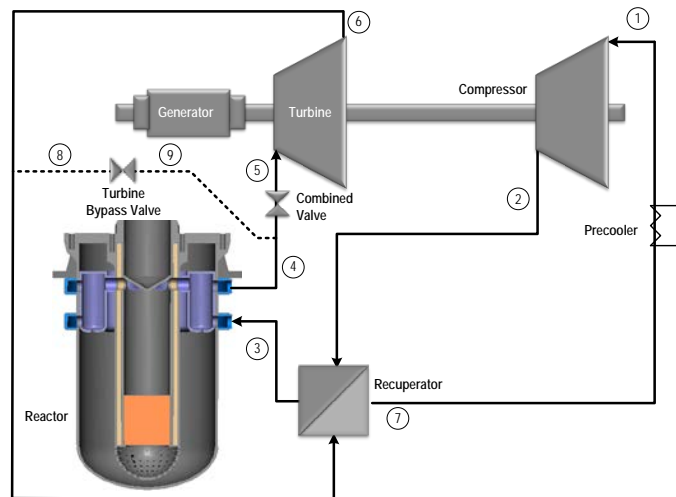
**Figure 3-28. Simple compression cycle Brayton with combined valve**

The *T-s* diagram and points properties simple compression Brayton cycle without optimization is described in Figure 3-29. This cycle layout is the backbone of gas cycles. But, the thermal efficiency is not high. Based on the computational results, for the cycle with conventional stop valve and control valve, the cycle thermal efficiency is 37.098%. By adopting the combined valve, the cycle thermal efficiency can be improved to be 37.142%.
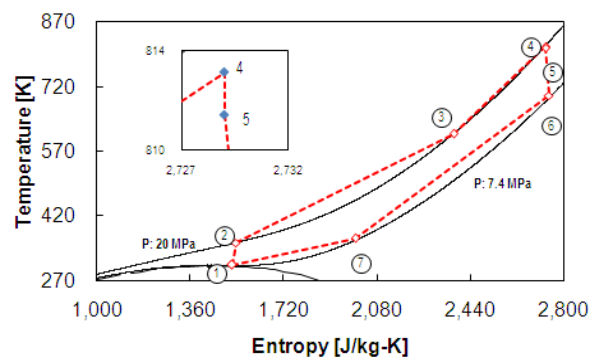


**Figure 3-29. *T-s* diagram of simple compression cycle with combined valve**

# 4. COMPENSATION OF VALVE NONLINEARITY CHARACTERISTIC

## 4.1. Introduction

In a power plant, turbine control valves play an imperative role to regulate the output power of the turbine. Therefore they have to be operated linearly to be run by an automatic control system. Unfortunately, the control valve has inherently nonlinearity characteristic. For a given valve position reference signal, the flow increases more significantly near the closed end than near the open end of the stem travel. However, the steam/gas flow should be proportional to the ultimate desired quantity, output power, of the turbine to achieve a linear operation.

Differing mechanisms have hitherto been presented to compensate for the control valve nonlinearity characteristic. A proportional/linear operation was obtained by a mechanical hydraulic control (MHC) using cams. In this method, MHC improved the system by producing a nonlinear electric compensation to the nonlinear system of control valves. A different compensation approach was proposed by adopting the electro hydraulic control (EHC) using electrical "cams" instead of mechanical cams (Callan, 1963; Eggenberger et al., 1963). Generally, the EHC systems provide more flexibility than the MHC systems for power plant turbines (EPRI, 2006). A further improvement was developed by utilizing an adaptive control system with an electrical throttle pressure compensator to obtain an improved EHC system for reducing the nonlinearity of the load output versus load reference (Jensen and Schenectady, 1969). Two parallel valves can be adopted for a fast valving scheme of steam turbine to improve the transient stability of the power system side (Hassan et al., 1999).

This chapter focuses on engineering analysis for nonlinearity characteristic

compensation of the turbine control valve. To simulate the transient phenomena in this compensation of nonlinearity characteristic analysis, the existing standard engineering software tool MARS is utilized for analyzing the power conversion system instead of the current steady state OSCA code. The MARS code was originally developed based on the RELAP5/MOD3.2.1.2 and COBRA-TF of the U.S. Nuclear Regulatory Commission (KAERI, 2006a). As one of the standard nuclear power plant thermalhydraulic analysis codes, MARS is capable of modeling a wide range of systems spanning single pipes to the primary and secondary sides of the plant. Based on the MARS code result, Matlab Simulink analyzes the power flow of the generator connected to an infinite bus for representing the grid connection. Matlab Simulink, being extensively exploited in numerous disciplines, has an interactive environment to model, analyze and also simulate a wide variety of engineering dynamic systems including the multimachine in power systems. The user can derive many features and built-in components easily from SimPowerSystems toolbox (Patel et al., 2002; Schoder et al., 2003). SimPowerSystems provides with system analysis tools to display steady state voltage and currents, display and modify initial state values, perform load flows and machine initialization, display impedance vs. frequency measurement and also generate a report of the steady sate calculations.

Three different scenarios of Ulchin Units 3&4 are analyzed by considering the control valves opening sequence mechanism and the change rate of output power reference. The concept of the nonlinearity compensation itself can be adopted for the EHC system as well as the digital electro hydraulic control (DEHC) system as has previously been presented (Halimi and Suh, 2010a; Kang et al., 2008, 2009; Kang and Suh, 2009; Kim and Suh, 2009; Suh et al., 2010). Moreover, the compensation mechanism is experimentally tested on a single control valve using the compressed air instead of steam.

## 4.2. Nonlinearity Characteristic of Control Valve

A turbine system comprises such main components as stop valves, control valves and turbines connected by piping. The turbine system conventionally consists of an array of stop and control valves. A commercial large steam turbine generally has multiple control valves (four to ten) to regulate the mass flow of steam. The turbine system of the Optimized power reactor 1000 MWe (OPR1000) houses four stop valves and four control valves as shown in Figure 4-1 for Ulchin Units 3&4, Korea (KEPCO, 1996).
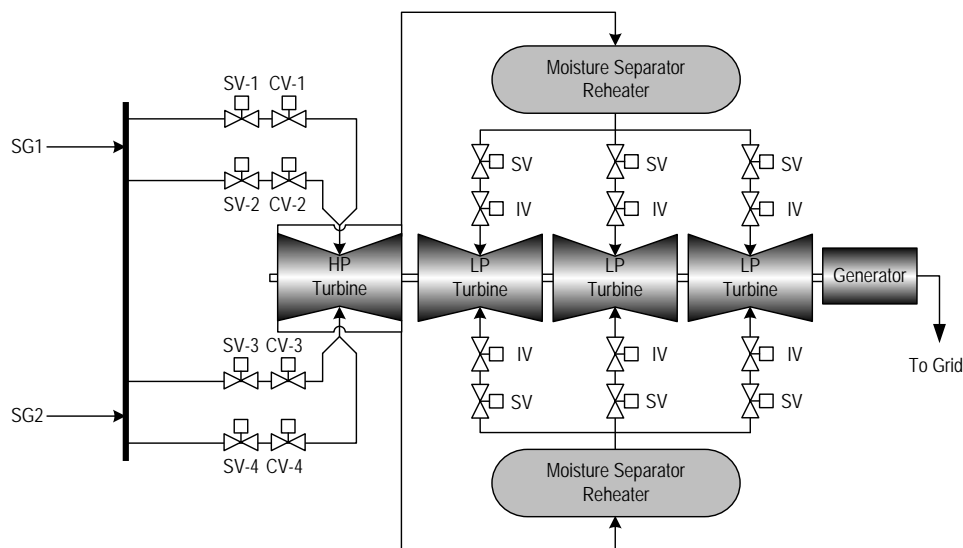


**Figure 4-1. Ulchin Units 3&4 steam turbine system**

The mechanism of opening of the multiple control valves refers to two control mechanisms of the steam flow: full arc and partial arc admissions. The partial arc control mechanism is widely used because it provides a significant improvement in turbine heat rate at partial loads. However, it results in a higher thermal stresses in the steam turbine under most of the operating transients (Eggenberger et al., 1968).

In the full arc admission, all the control valves are opened simultaneously. Instead, each or some control valves is or are opened sequentially in the partial arc mechanism. In practice, the steam flows through four control valves with nonlinear characteristics as shown in Figure 4-2. The full arc curve is found by presuming that the four valves are opened altogether. In Figure 4-2 the partial arc curve is obtained by assuming that the four control valves are in parallel with each other and opened in the following sequence: $1^{st}$ valve ➔ $2^{nd}$ valve ➔ $3^{rd}$ valve ➔ $4^{th}$ valve. Figure 4-2 shows that the flow increases much greater for a given valve position change near the closed end of travel than near the open end in both admission mechanisms.
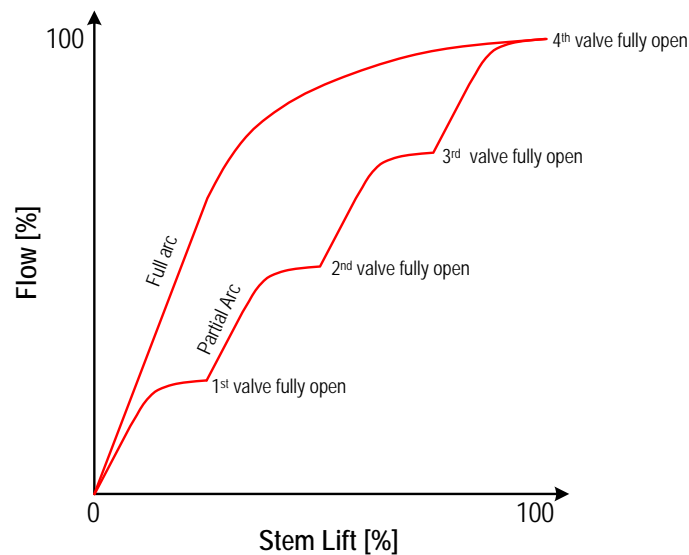


**Figure 4-2. Control valve flow characteristic**

## 4.3. Compensation of Nonlinearity Characteristic

The basic principle of valve nonlinearity compensation, Valve Engineering Linked

Analysis (VELA), is shown in Figure 4-3 and 4-4. A similar approach has previously been presented by Tovorniket al. (1989). Figure 4-3 shows a single control valve system without compensation. Note that the correlation is nonlinear between the stem lift and flow. By adding a nonlinearity compensation block, as exemplified in Figure 4-4, the correlation between the stem lift reference and flow can be rendered to be linear. It is thus possible to be run by automatic control system. To obtain this result, the correlation between $G_c(s)$ and $G_v(s)$ should be in the following form

$$G_c(s) = \frac{1}{G_v(s)} \tag{4-1}$$

where $s = \sigma + j\omega$.
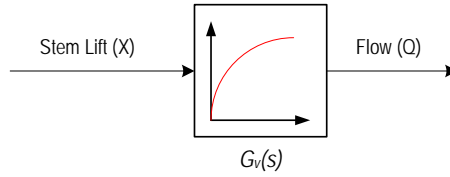


**Figure 4-3. Flow-stem lift block diagram**
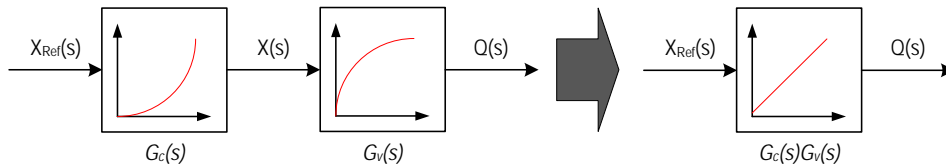


**Figure 4-4. Compensation principle**

In practice, the control valve system has been fully equipped with a stem lift position controller system. This system performance should therefore be

considered during the compensator design process. The original and manipulated block diagrams of control valve fully equipped with a controller system are shown in Figure 4-5(a) and (b), respectively. The nonlinearity can be compensated to a control valve system by using two mechanisms: feedforward compensation and feedback compensation, as shown in Figure 4-6 and 4-7, respectively, by Callan (1963). In the feedforward compensation mechanism the transfer function of the system is given by manipulating the block diagram in Figure 4-6 as follows

$$\frac{Q(s)}{X_{Ref}(s)} = G_{cff}(s)\frac{G_{cx}(s)G_a(s)}{1+G_{cx}(s)G_a(s)}G_v(s) \tag{4-2}$$

Based on Figure 4-5(b), in the normal operation the actual stem lift $X(s)$ shall equal the reference value $X_{Ref}(s)$, such that $\left|\frac{G_{cx}(s)G_a(s)}{1+G_{cx}(s)G_a(s)}\right| \approx 1$ . The transfer function of feedforward compensation can be obtained as follows

$$\frac{Q(s)}{X_{Ref}(s)} \simeq G_{cff}(s)G_v(s) = k_{cff} \tag{4-3}$$

$$G_{cff}(s) = \frac{k_{cff}}{G_v(s)} \tag{4-4}$$

Based on Eq. (4-4), the characteristic or the transfer function of feedforward compensator is an inverse of the control valve system.
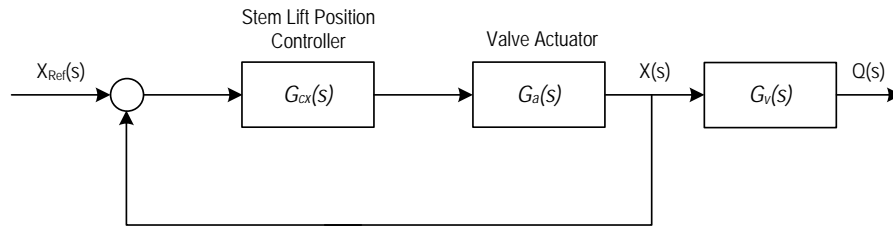
(a)
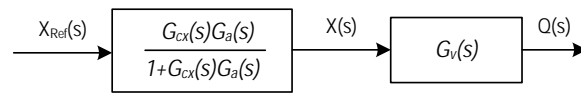


(b)

**Figure 4-5. Control block diagram without compensation**
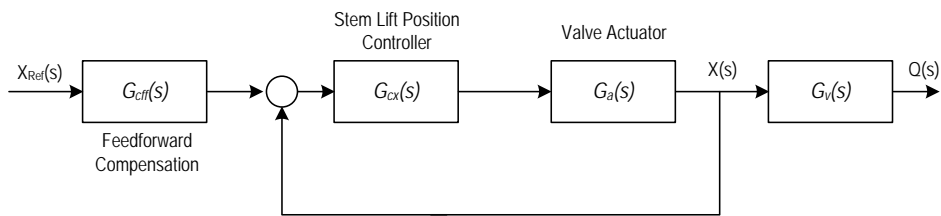


**Figure 4-6. Feedforward compensation block diagram**
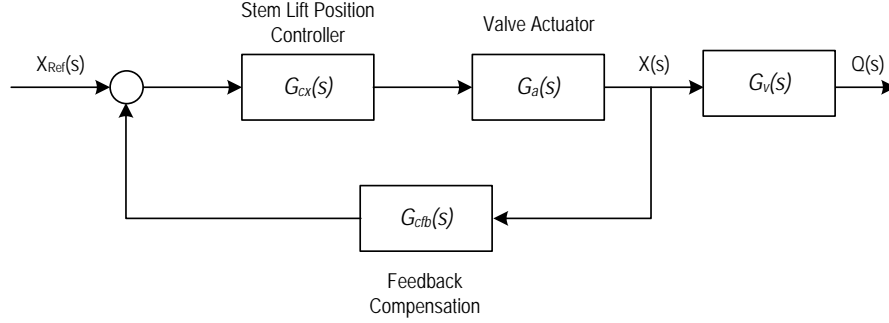
**Figure 4-7. Feedback Compensation Block Diagram**

Similarly, by manipulating the block diagram in Figure 4-7 for the feedback compensation, Eq. (4-2) becomes

$$\frac{Q(s)}{X_{Ref}(s)} = \frac{G_{cx}(s)G_a(s)}{1+G_{cx}(s)G_a(s)G_{cfb}(s)} G_v(s) \qquad (4\text{-}5)$$

As previously, assuming a linearity correlation, Eq. (4-5) can be written as

$$\frac{Q(s)}{X_{Ref}(s)} = \frac{G_{cx}(s)G_a(s)}{1+G_{cx}(s)G_a(s)G_{cfb}(s)} G_v(s) = k \qquad (4\text{-}6)$$

The transfer function of feedback compensation can be obtained as

$$G_{cfb}(s) = \frac{G_v(s)}{k} - \frac{k}{G_{cx}(s)G_a(s)} \qquad (4\text{-}7)$$

Because the original control transfer function $G_{cx}(s)G_a(s)$ is a realizable transfer function, according to the condition of realizability it can be demonstrated that $\frac{k}{G_{cx}(s)G_a(s)} \approx 0$, then Eq. (4-7) can be written as follows

$$G_{cfb}(s) = k_{cfb} G_v(s) \qquad (4\text{-}8)$$

where $k_{cfb} = \frac{1}{k}$

Differently from the feedforward compensator, Eq. (4-8) implies that the transfer function of feedback compensator is proportional to the control valve system transfer function. Moreover, the control valve transfer function can be obtained from stem lift and flow characteristic of the valve.

## 4.4. Computational Analysis

The VELA computational analysis comprises two main calculations: thermalhydraulic and power flow analysis. The thermal hydraulic analysis covers the primary and secondary systems of nuclear power plant by using the MARS code. The electrical power analysis is handled by the Matlab Simulink software. To generate a linked computational analysis between these software analyses, the turbine-generator system is used as the linker component. Thus the turbine output data of the MARS code is designed to be compatible with the required input data of the Matlab Simulink generator component as depicted in the computational analysis flowchart of Figure 4-8. As a reference case study, Ulchin Units 3&4 are chosen for this analysis. First, the primary and secondary systems of Ulchin Units 3&4 are nodalized and analyzed by MARS to generate steady state and transient analysis results. The turbine set is modeled as a single turbine system rather than one high pressure and three low pressure turbines. By this modeling approach, the complexity of control mechanism can be reduced and the concept of nonlinearity compensation may be easier to be understood. To analyze the power flow from the power plant unit to a grid connection system, a single generator machine with infinite-bus power system is considered in Matlab Simulink.
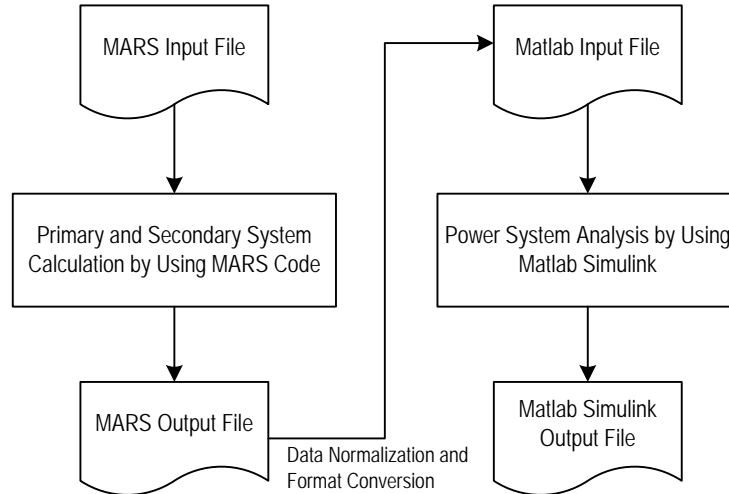
**Figure 4-8. Flowchart of VELA**

### 4.4.1. MARS Simulation Analysis

The Ulchin Units 3&4 nodalization for MARS is depicted in Figure 4-9. The trip valve and servo valve type are selected to represent the stop valve and control valve of the turbine system, respectively. The servo valve model can control the junction flow area between two control volumes as a function of time. The stem position of this valve model is controlled by a controlled variable rather than by a specific rate parameter (KAERI, 2006b, c). As the valve control system, it has adopted a simplified standard electro-hydraulic governor system model for the steam turbine (Byerly, 1973; Lee, 1988; Mello et al., 1991). Figure 4-10 shows the block diagram of this control system. It is assumed that the governor of the control valve has unity gain constant.
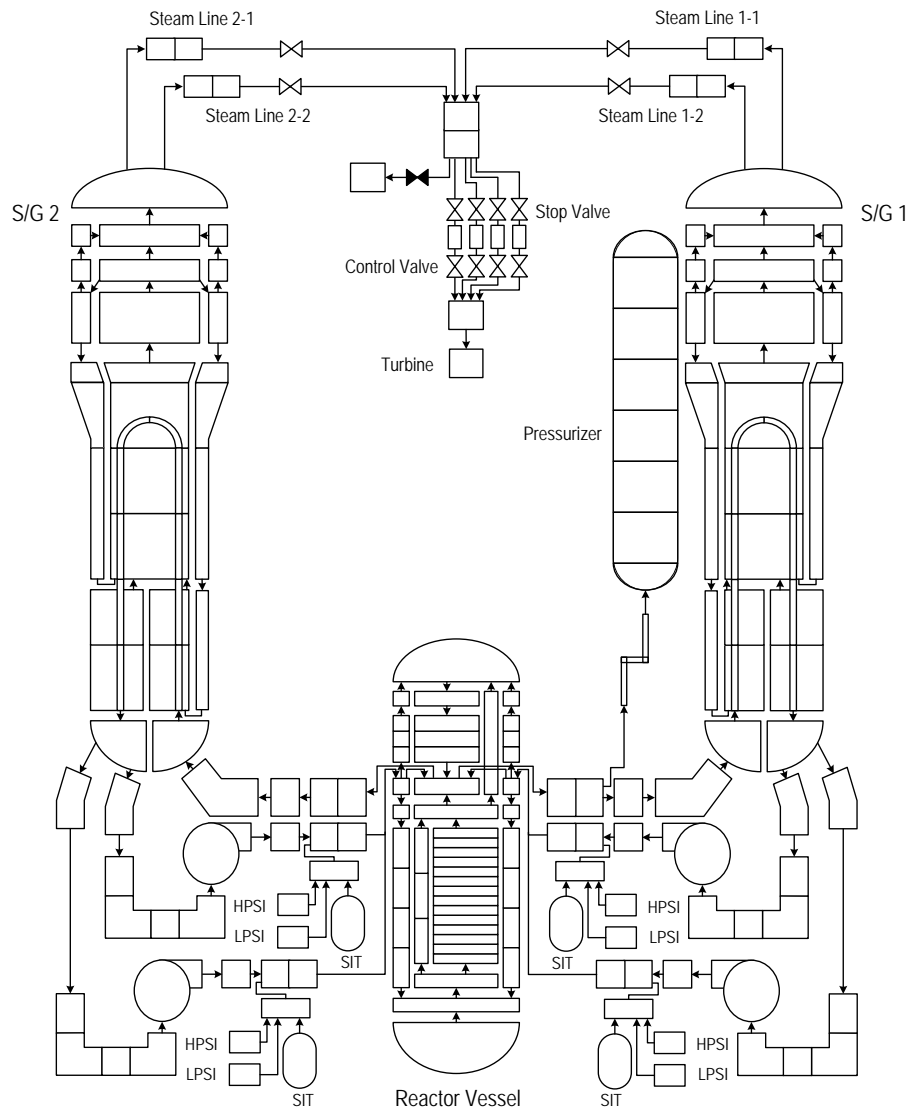
**Figure 4-9. Primary and secondary system nodalization**
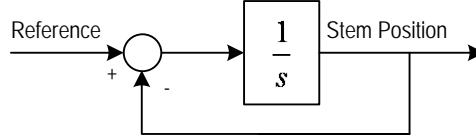
**Figure 4-10. Control system model for control valve**

To show the effectiveness of the compensation, the $\mathcal{L}_2$ norm of the reference tracking error $e_T(t)$, denoted by $J_T$, is used (Aguiar et al., 2008) . The tracking error is defined as

$$e_T(t) = y(t) - r(t) \tag{4-9}$$

where $y(t)$ represents the actual value and $r(t)$ is the reference value.

By using this definition, the transient tracking error can be obtained as

$$J_T(t) = \int_{t_0}^{t_\infty} \|e(\tau)\|^2 \, d\tau \tag{4-10}$$

Three different control valve admission scenarios are analyzed as case study references. Each scenario is analyzed without and with compensation to check on the effectiveness of the compensation. For all scenarios, the steady state simulations are run from $t = 0$ to $t = 2000$ s to obtain the initial condition for transient simulations. During these simulations, all stop and control valves are fully and 10% open, respectively.

In the full arc admission scenario, the stem position of all the control valves start to be changed at $t = 2150$ s. To keep the power output reference rate constant at 9% pu/min (0.0015 pu/s), all the control valves are fully open at $t = 2750$ s. Figure 4-11 through 4-13 show the MARS simulation results for full arc admission without compensation. The primary system pressure is constant at 15.5 MPa as shown in Figure 4-11. Figure 4-12 illustrates the flow of each control valve and turbine inlet.

98

Note that the flow characteristic is not linear albeit the reference is in the linear form. By applying $t_0 = 2000$ s and $t_\infty = 2900$ s to Eq. (4-10), the convergence to the desired reference signal is achieved with transient error $J_T \simeq 50.40$, as depicted in Figure 4-13. This value shows that the nonlinearity characteristic contributes significantly to a linear reference tracking transient error of the system.
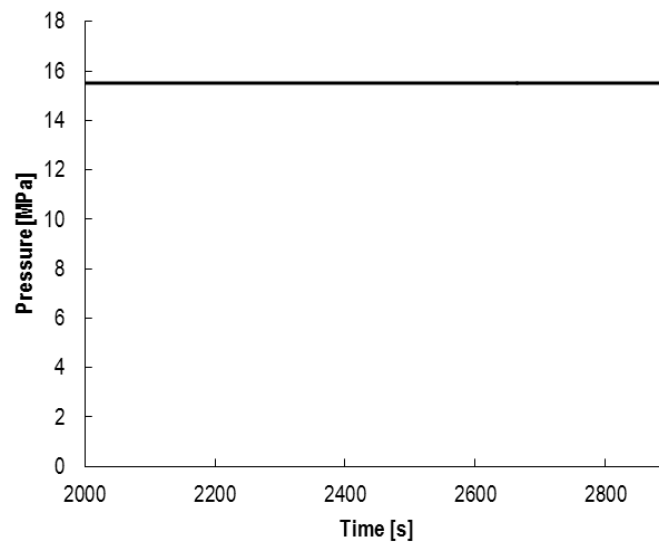


**Figure 4-11. Pressurizer pressure for full arc admission without compensation**
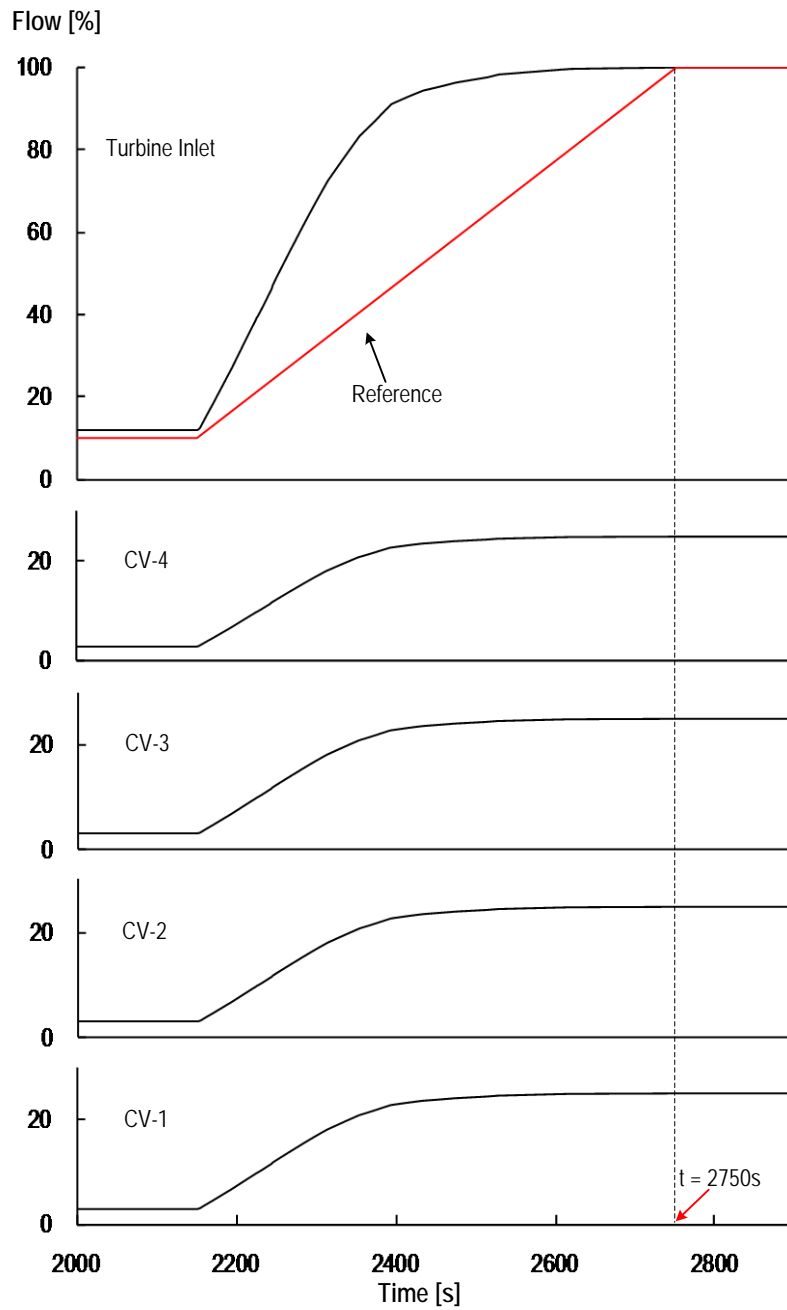
**Figure 4-12. Steam flow for full arc admission without compensation**
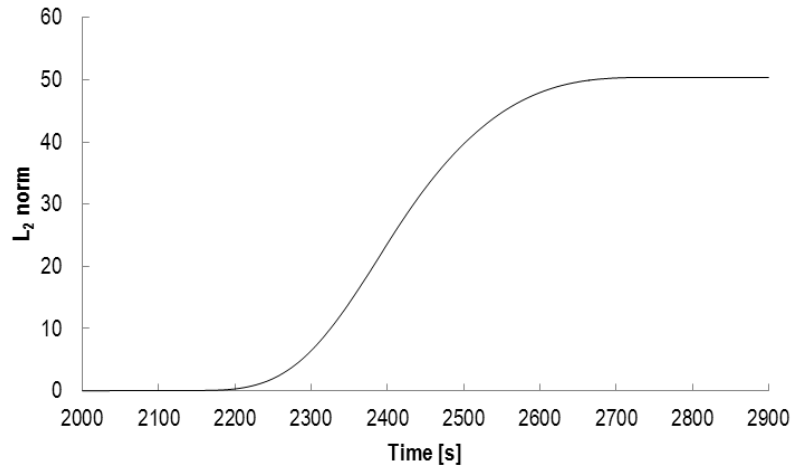
**Figure 4-13. Transient error of full arc admission without compensation**

A feedback compensation mechanism is used for the full arc admission with compensation. Thus the compensator is put on the feedback path of each control valve stem position control system as shown in Figure 4-14. As aforementioned, this compensator has a similar characteristic with the control valve flow characteristic. In simulation, the stem position of all the control valves start to be changed at $t = 2150$ s with power output reference rate 9% pu/min. Figure 4-15 shows the steam flow of each control valve and turbine inlet. Compared to Figure 4-12, Figure 4-15 implies that the compensation can improve the system response to be linear and the transient error can significantly be reduced to be $J_T \simeq 0.84$, as depicted in Figure 4-16.
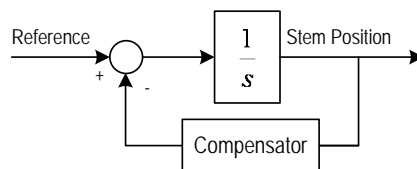


**Figure 4-14. Compensation control system model for control valves**
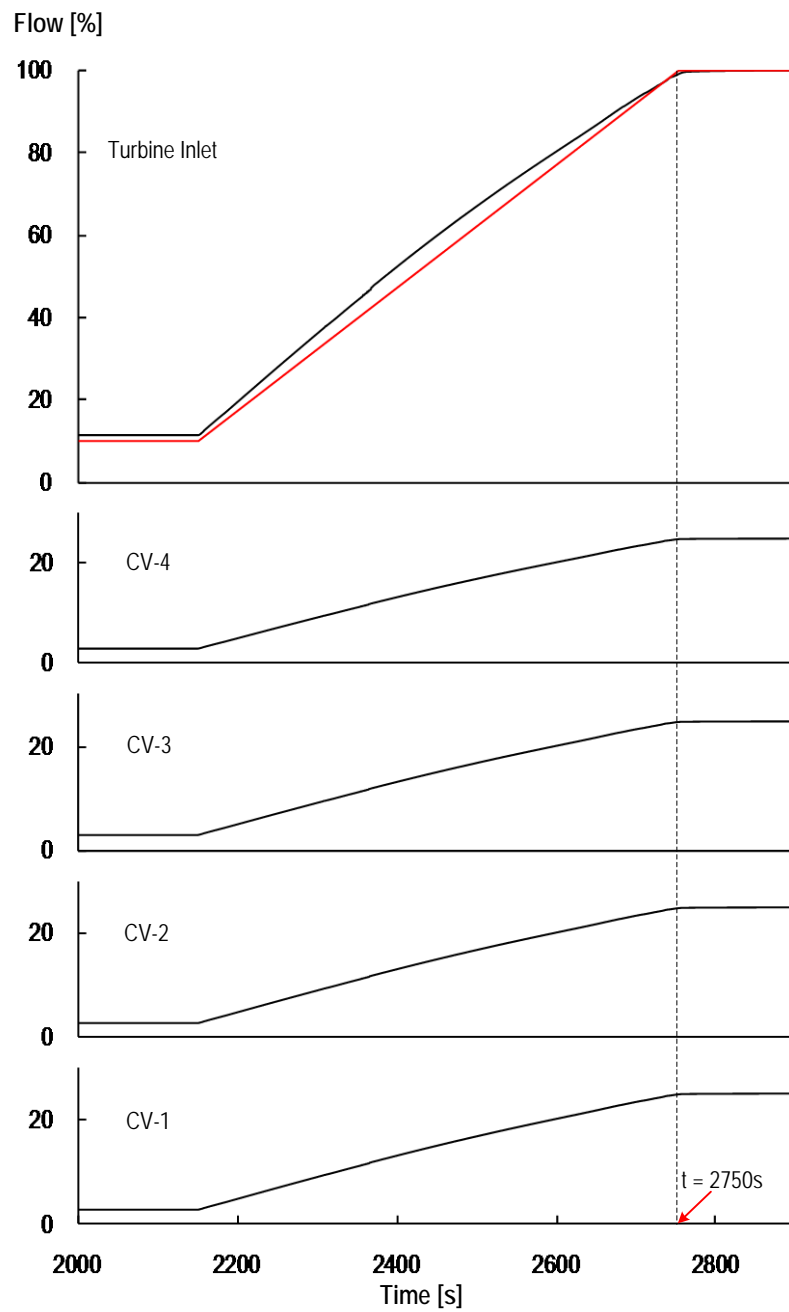
**Figure 4-15. Steam flow for full arc admission with compensation**
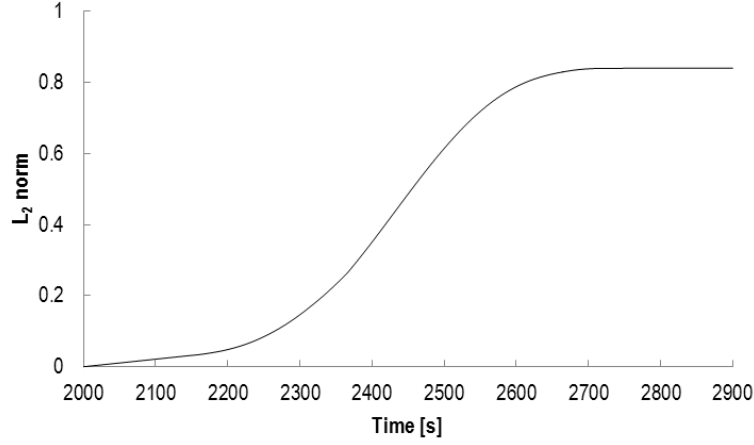
**Figure 4-16. Transient error of full arc admission with compensation**

Differently from the full arc admission in which all the valves are opened simultaneously, the valves are opened sequentially or some of them are opened together and the other(s) is/are opened individually in the partial arc admission. In this analysis two kinds of partial arc admission scenarios are analyzed. The first assumes that all valves are opened fully sequentially or in the following sequence: CV-1➔ CV-2 ➔ CV-3 ➔ CV-4. Figure 4-17 and 4-18 and also Figure 4-19 and 4-20 present the MARS simulation results of this scenario without compensation and with compensation, respectively. In this simulation, the power output reference rate is kept constant at 9% pu/min. The stem position of CV-1, CV-2, CV-3, and CV-4 start to be changed at $t = 2150$ s, $t = 2320$ s, $t = 2490$ s, and $t = 2660$ s, respectively. The CV-1, CV-2, CV-3, and CV-4 are fully opened at $t = 2300$ s, $t = 2470$ s, t = 2640 s, and $t = 2810$ s, respectively. Figure 4-17 shows the detailed flow of each control valve and turbine inlet by this scenario. This figure shows that the steam flow characteristic is not linear. The convergence to this reference signal is achieved with transient error $J_T \simeq 4.50$, as shown in Figure 4-18. Albeit the transient error is reduced to 91% of the full arc admission transient error, the nonlinearity characteristic persists.

103
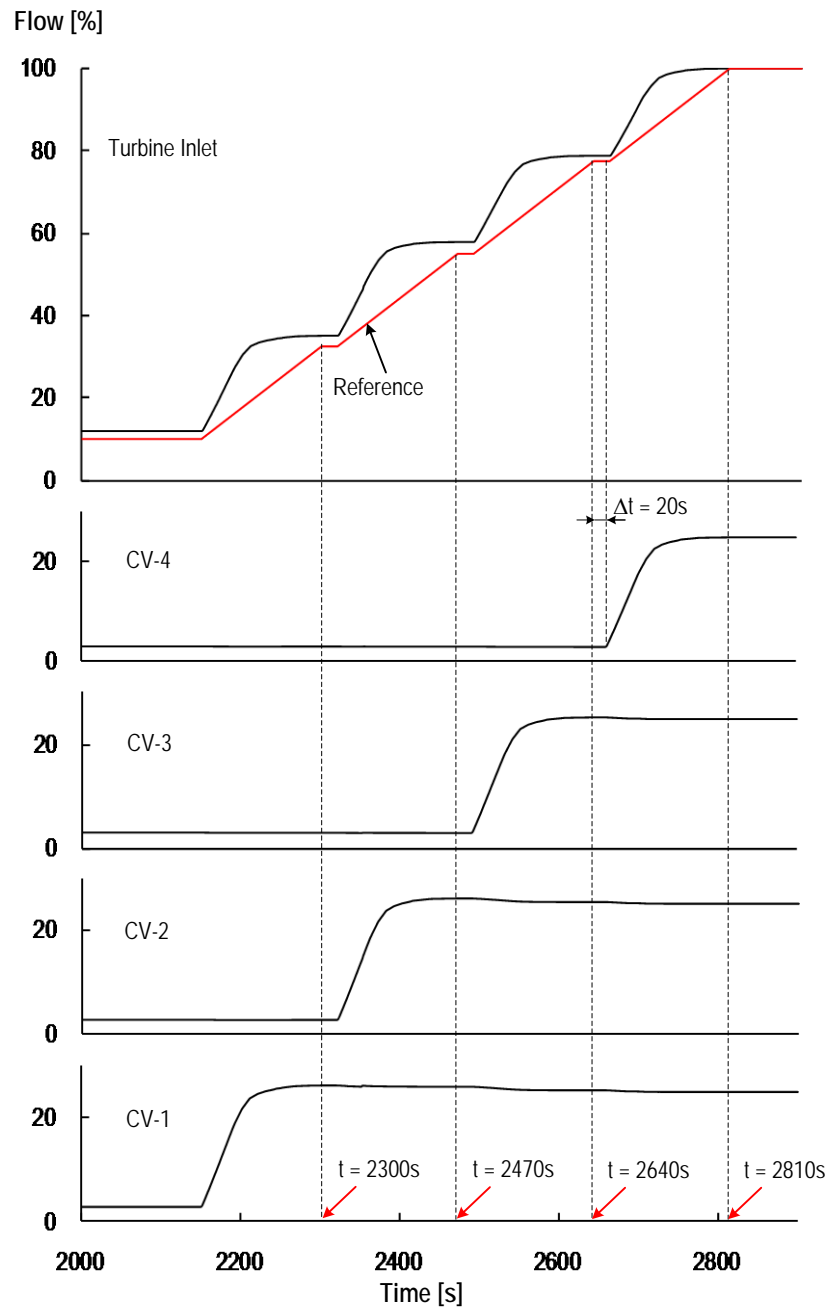
**Figure 4-17. Steam flow for not compensated fully-partial arc admission**
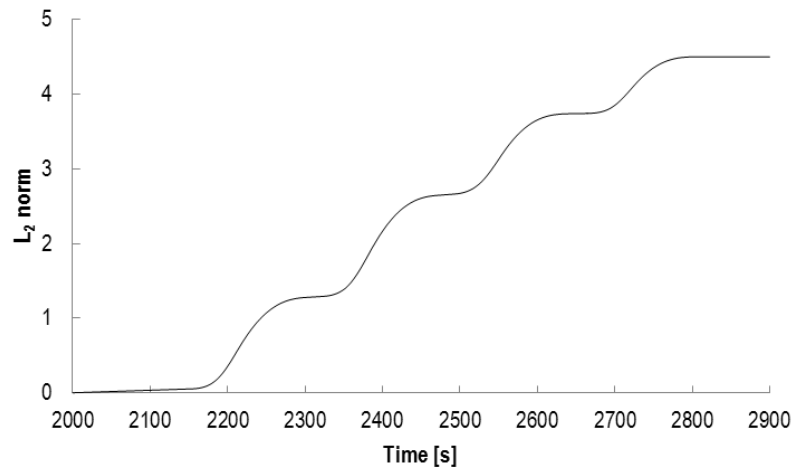
**Figure 4-18. Transient error of not compensated fully-partial arc admission**
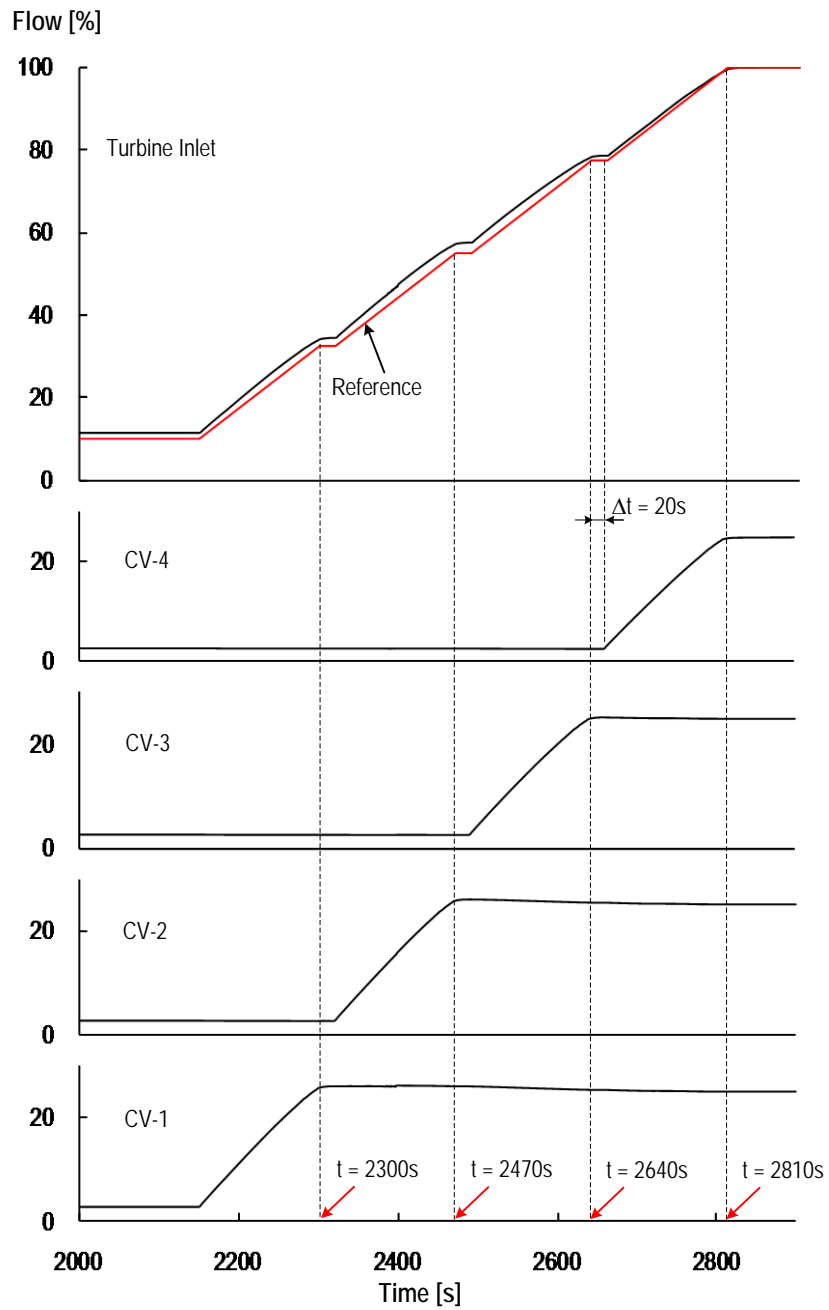
**Figure 4-19. Steam flow for fully-partial arc admission with compensation**
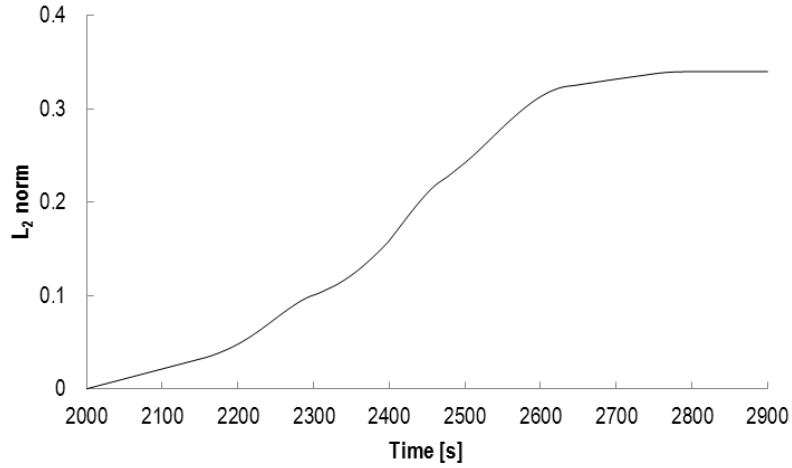
**Figure 4-20. Transient error of fully-partial arc admission with compensation**

By using the same scenario, the fully partial arc admission with compensation is illustrated in Figure 4-19 and 4-20. The feedback compensation mechanism is adopted in this analysis. Figure 4-19 depicts the steam flow in each control valve and turbine inlet. Compared to Figure 4-17, Figure 4-19 confirms that the compensation can improve the system response to be linear and the transient tracking error can be suppressed to $J_T \simeq 0.34$, as depicted in Figure 4-20.

The second scenario of the partial arc admission uses different power output reference rates for each admission to accommodate for the multiple power reference change rates option which is also commonly equipped in the commercial steam turbine governor systems (Choi et al., 2009; Wang and Guo, 2009). In this scenario, the sequence of the valves opening is CV-1, CV-2 ➔ CV-3 ➔ CV-4. The stem positions of CV-1 and CV-2 are changed from $t = 2150$ s to $t = 2375$ s by the power output reference rate 6% pu/min. CV-3 start to be changed at $t = 2550$ s by the power output reference rate 9% pu/min. From $t = 2375$ s to $t = 2550$ s and from $t = 2700$ s to $t = 2750$ s, there are no changes in the reference signal or the

107

reference is in the step reference mode. The stem of the last control valve CV-4 is lifted from $t = 2750$ s to $t = 2858$ s to follow the power output reference rate 12.5% pu/min. Figure 4-21 through 4-23 demonstrate the detail steam flow in each control valve and turbine inlet by this scenario without compensation and with compensation, respectively. Figure 4-21 shows that the flow characteristic is not linear. The convergence to reference signal is achieved with transient error $J_T \simeq$ 7.92 as shown in Figure 4-22. By using compensation, the transient error $J_T$ can be reduced to 0.45 or $5.74 \times 10^{-2}$ times much smaller, as shown in Figure 4-24.
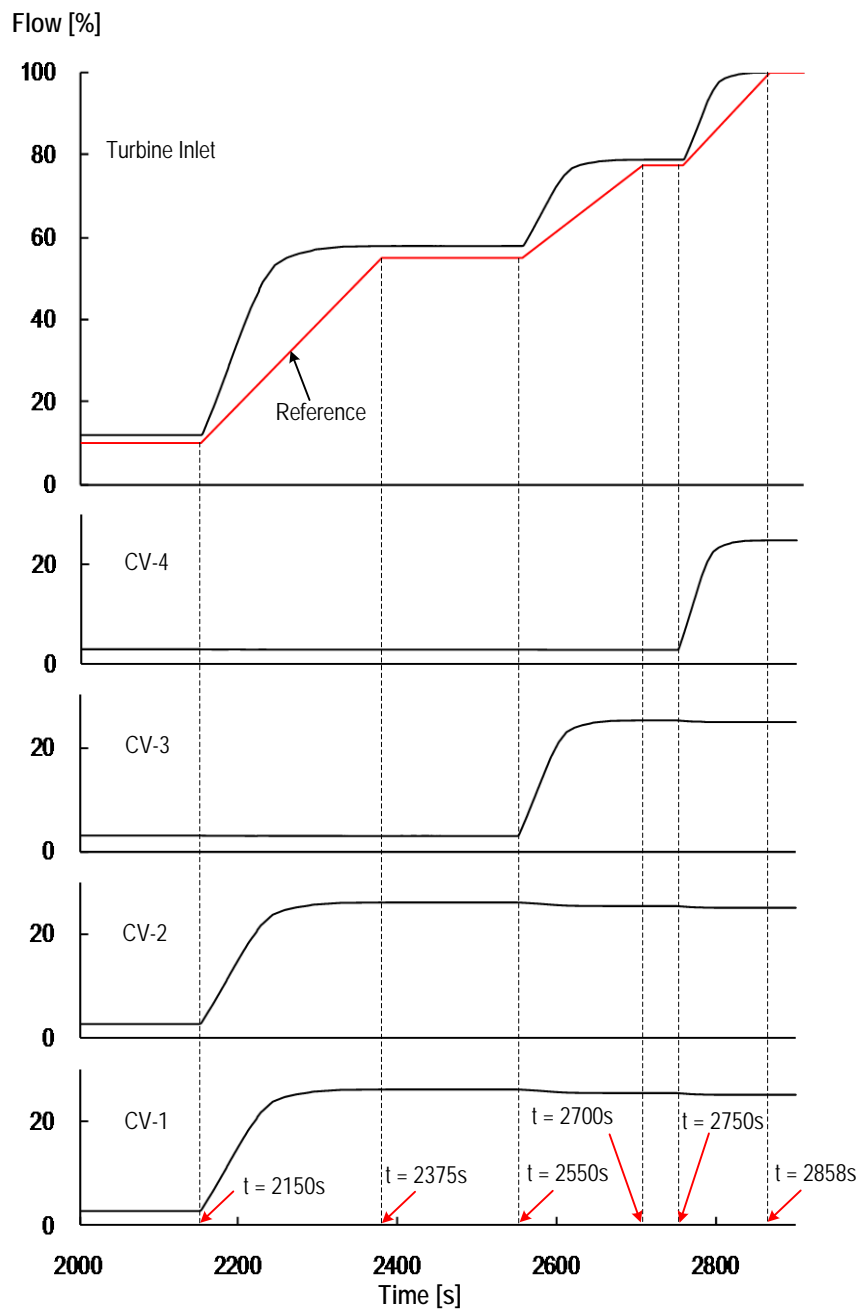
**Figure 4-21. Steam flow for not compensated partly-partial arc admission**
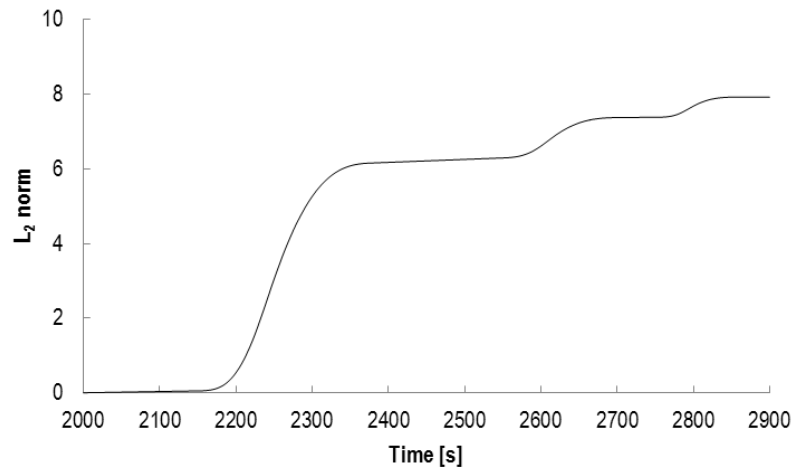
**Figure 4-22. Transient error of not compensated partly-partial arc admission**
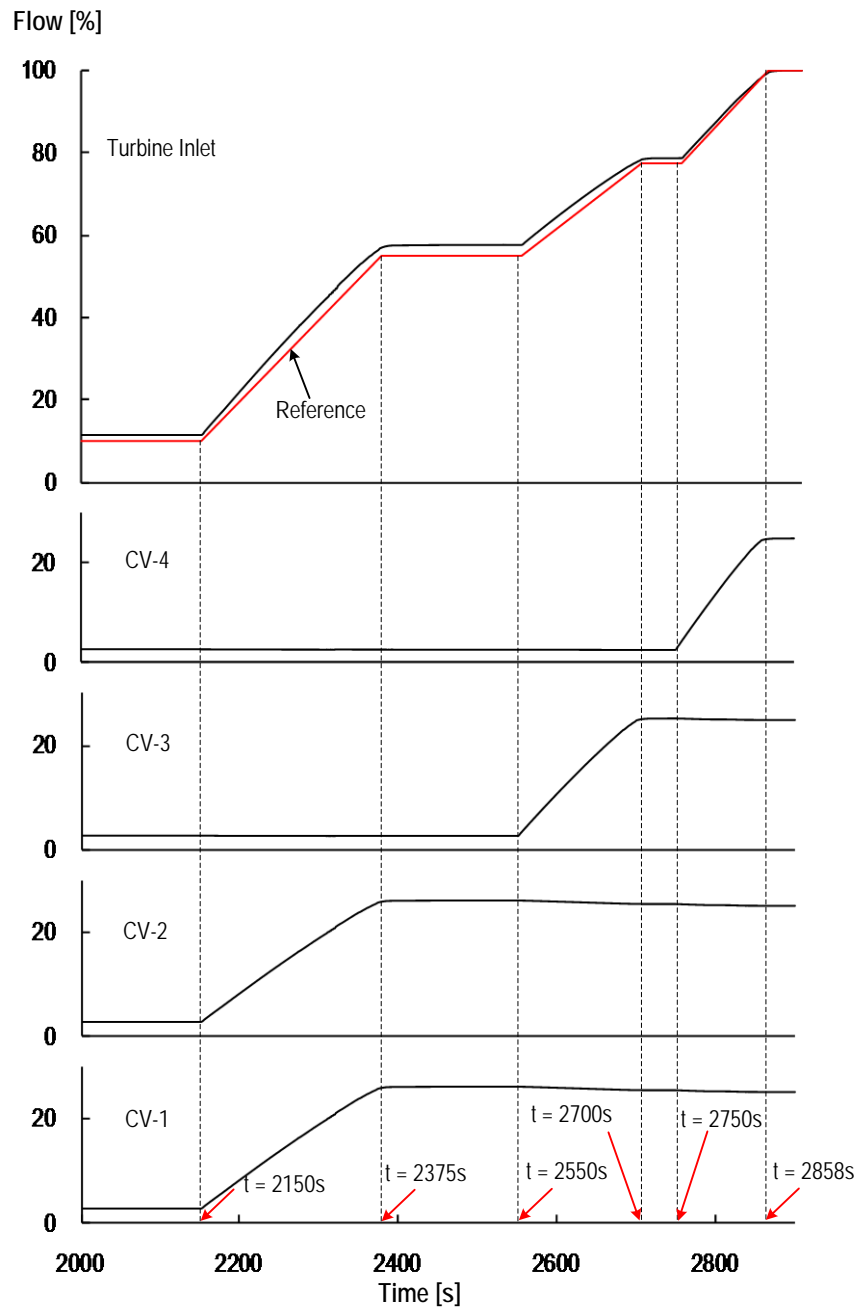
**Figure 4-23. Steam flow for partly-partial arc admission with compensation**

111
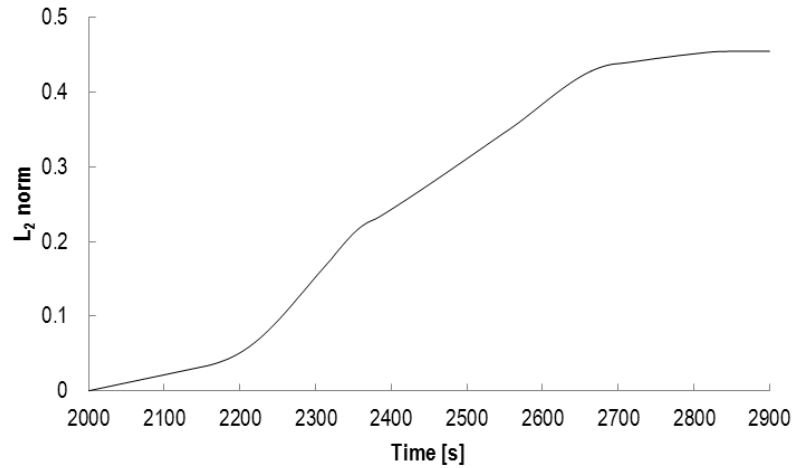
**Figure 4-24. Transient error of partly-partial arc admission with compensation**

### 4.4.2. Compensation Sensitivity Analysis

Various compensators are adopted to analyze the compensation sensitivity to total flow on the turbine inlet side which is proportional to the output power. As mentioned in the previous sub-chapter, the compensator transfer function can be obtained from the control valve transfer function. Figure 4-25 shows the normalized input and output of the compensators. The 100% compensation, 110% compensation and 90% compensation represent 0%, +10% and -10% offsets on the compensator, respectively. The full arc admission and fully partial arc admission are chosen as reference scenarios in this analysis.

112
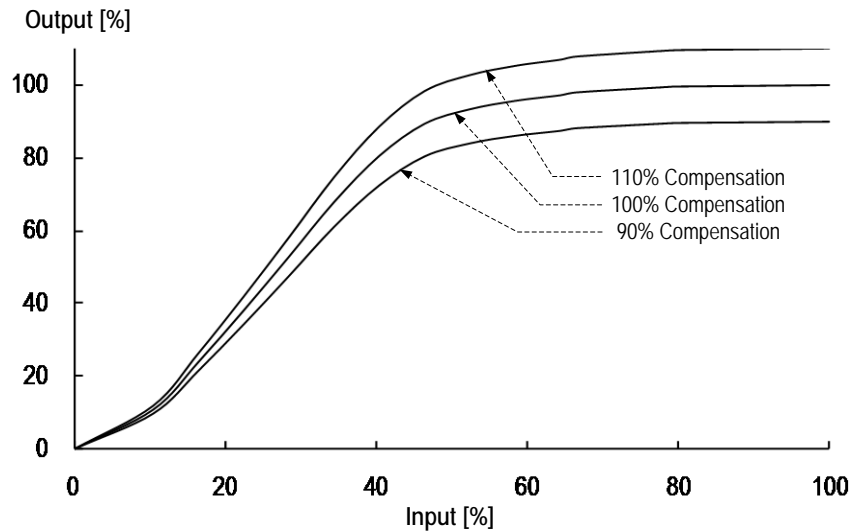
**Figure 4-25. Nonlinearity characteristic compensators**

An offset on the compensator may generate additional tracking error and steady state offset as illustrated in Figure 4-26 and 4-27. The full arc admission is more sensitive to negative offset of the compensator compared to the partial arc admission as described in Table 4-1 and 4-2. Due to under-compensation, a negative 10% offset on the compensator will increase the tracking error by 5.82 and 3.24 times in the full arc and partial arc admission, respectively. But these tracking errors are still much smaller, viz. 0.10 and 0.24 times the original systems without compensation. In terms of steady state error, a positive offset on the compensator will generate a negative offset on the output power due to its over-compensation. Both admission scenarios have the same sensitivity from this point of view. In the full power operation, a positive 10% offset on the compensator reduces the steady state output by 7.50% in the full arc admission and partial arc admission. Practically, all of these errors can be minimized by an accurate and precise model of the valve. Thus, the compensator can be designed exactly the same as the actual valve without any offsets.

113
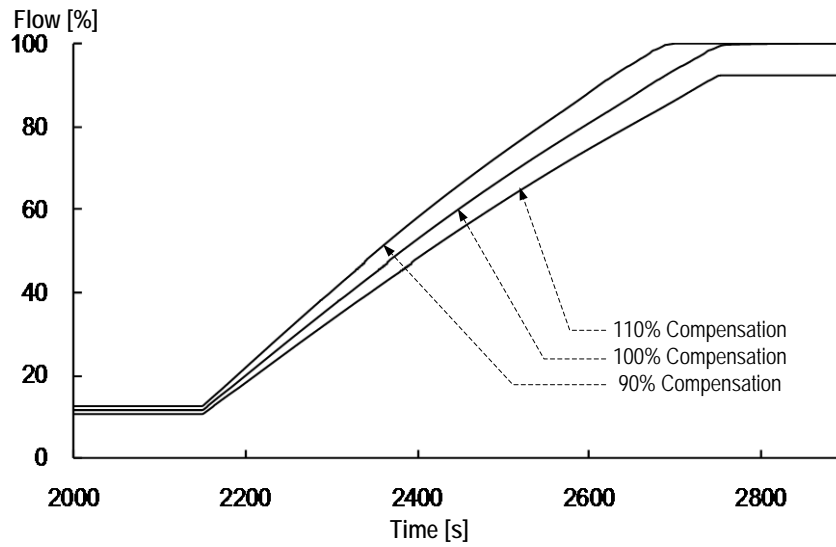
**Figure 4-26. Steam flow for full arc admission with various compensations**
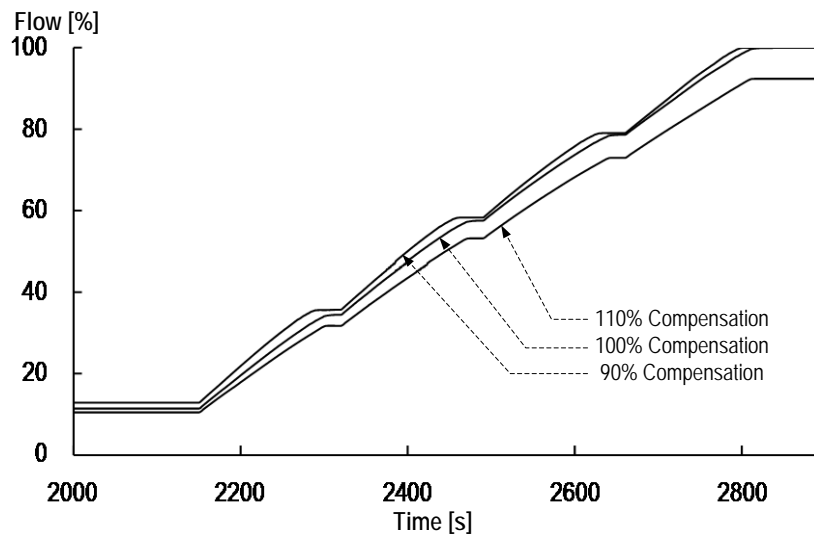


**Figure 4-27. Steam flow for fully-partial arc admission with various compensations**

114

**Table 4-1. Compensation sensitivity in full arc admission**

| Compensation | Tracking Error ($J_T$) | Steady State Error [%] | |
|---|---|---|---|
| | | 10% Power | 100% Power |
| Without Compensation | 50.40 | +1.84 | 0.00 |
| 100% Compensation | 0.84 | +1.46 | 0.00 |
| 110% Compensation | 1.33 | +0.47 | -7.50 |
| 90% Compensation | 4.89 | +2.68 | 0.00 |

**Table 4-2. Compensation sensitivity in partial arc admission**

| Compensation | Tracking Error ($J_T$) | Steady State Error [%] | |
|---|---|---|---|
| | | 10% Power | 100% Power |
| Without Compensation | 4.50 | +1.85 | 0.00 |
| 100% Compensation | 0.34 | +1.46 | 0.00 |
| 110% Compensation | 1.22 | +0.47 | -7.50 |
| 90% Compensation | 1.10 | +2.68 | 0.00 |

### 4.4.3. Power Flow Analysis

The Matlab Simulink software is adopted to analyze the electrical power part. To make a linked computational analysis with the MARS code, the turbine output data of the MARS code is customized to be compatible with the required input data of the Matlab Simulink synchronous machine component with a mechanical input. The nominal power and frequency of generator are 1219 MVA and 60 Hz, respectively. This generator is connected to a grid system which is represented as an infinite bus via a three-phase, two-winding, Y/D, 22kV/345kV transformer as shown in Figure 4-28. The power delivered by the generator to grid system can be obtained by controlling the excitation system of the generator.
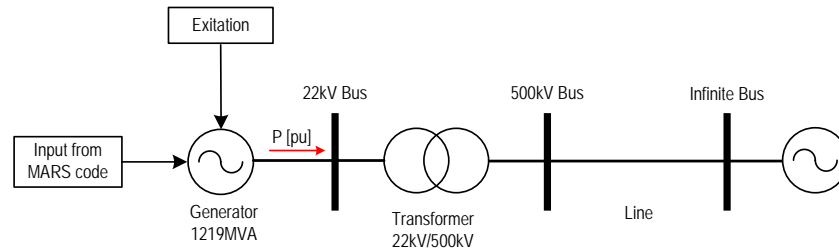
**Figure 4-28. Power flow analysis scheme**

Figure 4-29 through 4-31 show the power delivered by the generator in the full arc and partial arc admissions without and with compensation, respectively. Due to the nonlinearity characteristic of the control valves of the steam turbine, the power delivered by the generator to grid system is nonlinear, whereas the reference is linear. These conditions can be improved by using the nonlinear characteristic compensation as shown in Figure 4-29 through 4-31. These figures signify that the nonlinearity phenomena can appreciably be reduced.
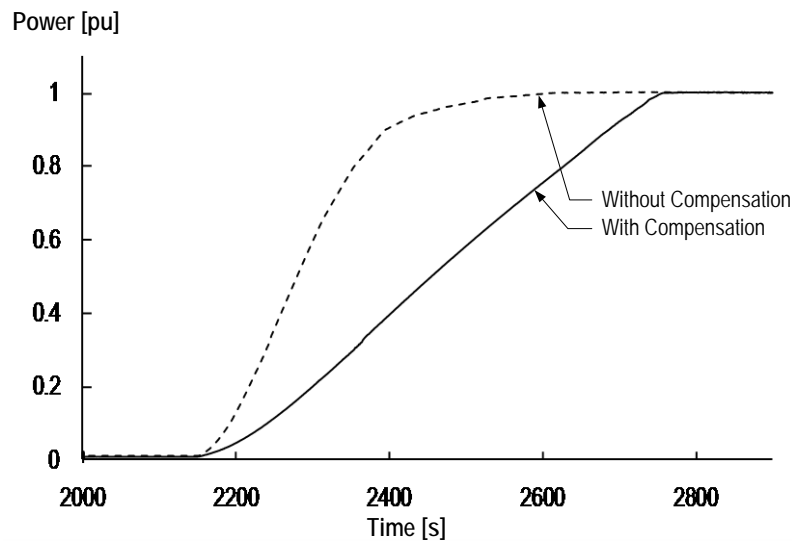


**Figure 4-29. Generator power output for full arc admission**
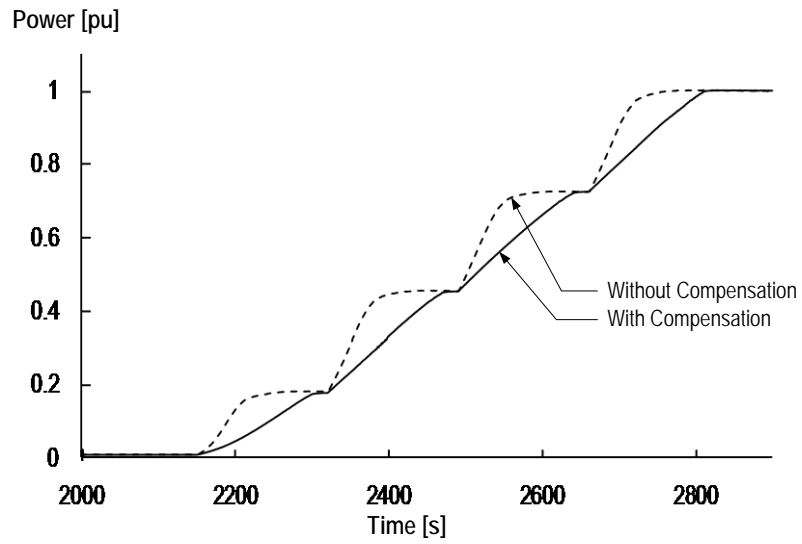
**Figure 4-30. Generator power output for fully partial arc admission**
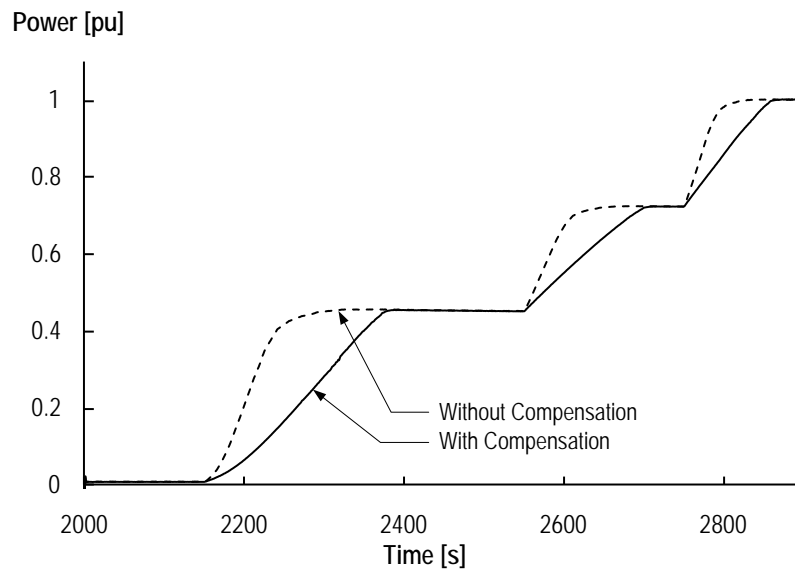


**Figure 4-31. Generator power output for not fully partial arc admission**

117

## 4.5. Experimental Validation

An experimental test was performed to validate the compensation method. Figure 4-32 shows the experiment scheme to corroborate the proposed compensation concept. In this experiment the compressed air is used as working fluid instead of the high pressure steam. A pneumatic actuator type of control valve is chosen as the main control valve. The valve stem position is measured by using a linear type positioner transmitter with a current output 4-20 mA. An analog-to-digital converter is used to convert the output current of the positioner transmitter to a digital signal form. This digital signal is used as the main feedback information for the main control system in a personal computer (PC). A simple proportional integrator type controller is selected to control the position of valve stem. All the control and data acquisition systems, including the nonlinearity characteristic compensator, are written in the LabVIEW software. Moreover, a digital-to-analog converter is used to convert the control reference signal from the PC to current (4-20 mA) as input to the linear type positioner of the control valve.
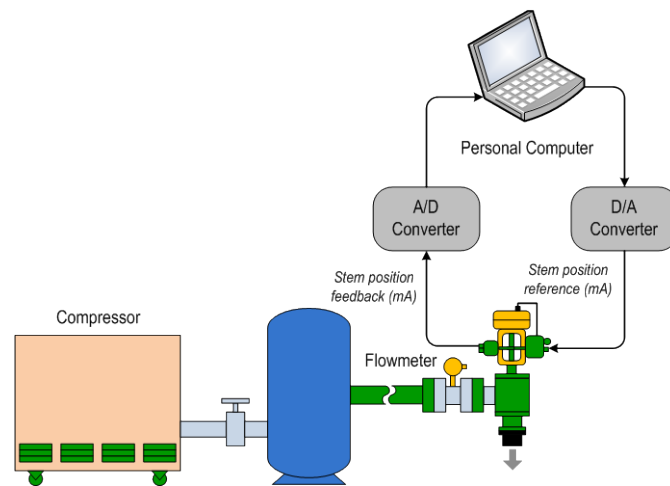


**Figure 4-32. Experiment scheme**

The compensator function depends on the flow characteristic of the control valve as aforementioned. An open test loop is run to obtain this characteristic curve. Figure 4-33 shows the nonlinear flow characteristic of control valve in this experiment. The curve demonstrates that the control valve also has about 10% inherently nonlinear deadband characteristic. This deadband causes a delayed response on the flow characteristic curve.

The compensator is designed based on the flow characteristic curve. A closed loop control system with feedforward and feedback compensation is adopted for the experiment to illustrate the effectiveness of the compensation mechanism. Figure 4-34 and 4-35 illustrate the flow characteristic with the feedforward and feedback compensation, respectively. Note that the compensation mechanism can readily linearize the nonlinear flow characteristic.

Using the similar method as mentioned in the previous sub-chapter, it can be obtained the transient error $J_T$ are 14.18, 0.063, and 0.044, for the case without compensation, with feedforward compensation, and feedback compensation, respectively, as illustrated in Figure 4-36.
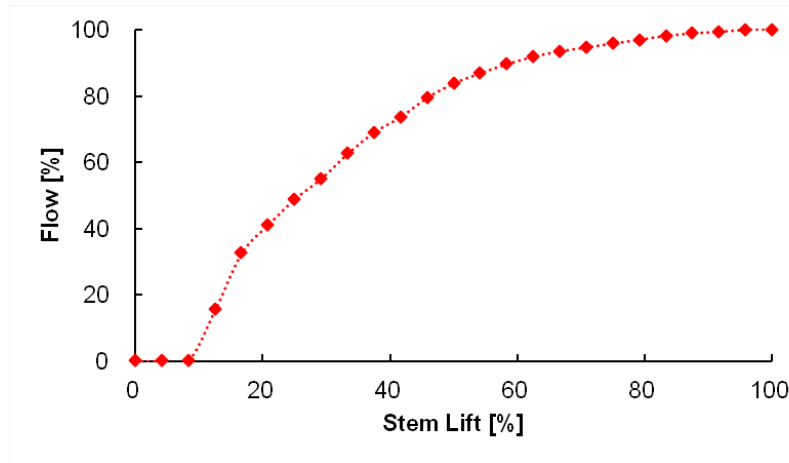


**Figure 4-33. Valve flow characteristics**
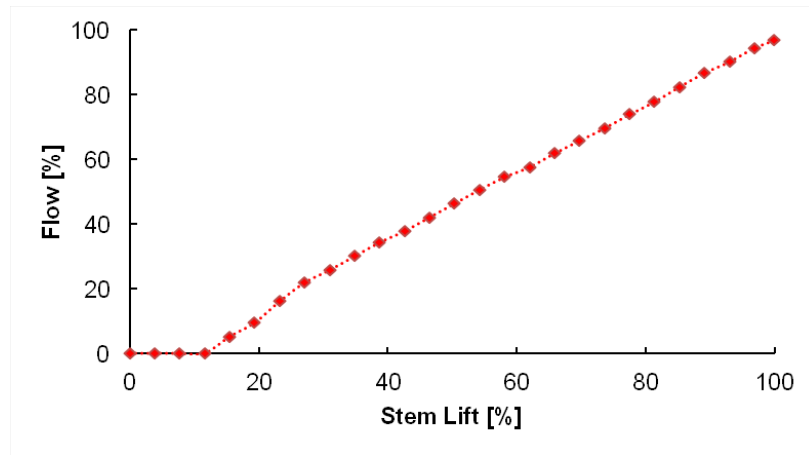
**Figure 4-34. Flow characteristic with feedback compensation**
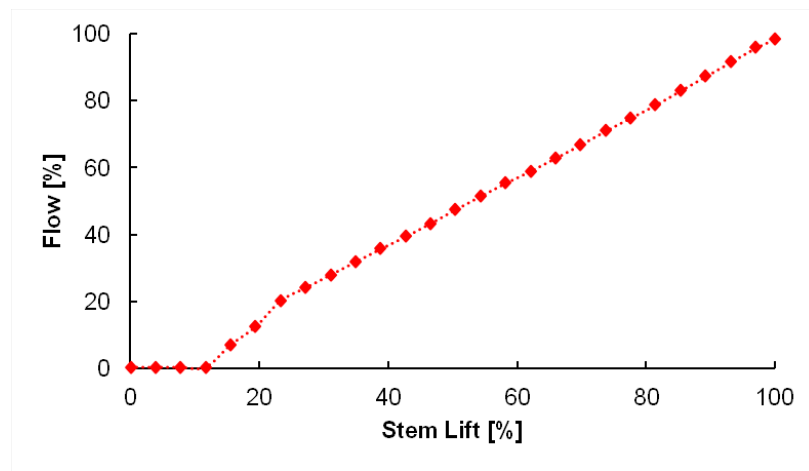


**Figure 4-35. Flow characteristic with feedforward compensation**
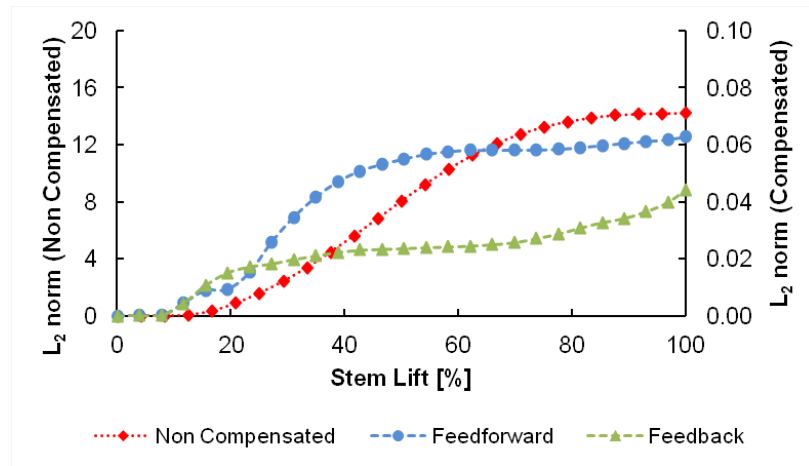
**Figure 4-36. Tracking error**

# 5. OTHER APPLICATIONS

## 5.1. Introduction

In the final decade of the 20$^{th}$ century, the European fusion programme which covered a series of studies on safety, environmental and economic potential of fusion power presented that fusion power has attractive inherent safety and environmental features to address global climate change and gain public acceptance. Also, in term of cost, it is likely to be comparable with that from other environmentally responsible electricity generation resources (Maisonnier et al., 2006). These study results have encouraged many researchers for further investigating to realize the utilization of fusion reactor for electricity generation. Moreover, under the assumption of successful International Thermonuclear Experimental Reactor (ITER), as the largest current fusion reactor prototype, it will be needed to prepare a concrete concept of the commercial demonstration fusion power plant DEMO (Konishi et al., 2002). The DEMO ultimately aims to demonstrate the electricity production feasibility based on fusion power.

Albeit the electricity generation has been as the major concern in nuclear power investigations for long periods, the development of nuclear reactor can be inseparable from the role of marine propulsion researches. In the history of reactor technology, marine nuclear propulsion systems had encouraged many researchers to focus on small nuclear reactor. The development of small reactors began in the early 1950s for naval propulsion as power sources for nuclear submarines. Over the years, several countries have been continuously working on the development of SMRs (Vujić et al., 2012). There have been many hundreds of smaller reactors built both for naval use (up to 190 MW thermal) and as neutron sources, yielding enormous expertise in the engineering of small units. The International Atomic Energy Agency (IAEA) defines 'small' as under 300 MWe (Hoffelner et al., 2011).

Moreover, As one of leaders in nuclear technology for marine applications, Lead–Bismuth Eutectic-cooled reactors were developed and built in the Soviet Union as naval submarine propulsion reactors and supporting land prototypes (Cinotti et al., 2011; Sienicki, 2012).

The recent R&D results point to advantages of nuclear power propulsion for marine applications with a long period of time without refueling on the ocean such as military surface ship, submarine, ice breaker, and high performance cargo vessel, just to name a few. The work on nuclear propulsion system had started in the 1940s and the first test reactor started up in 1953 (Pocock, 1970). Generally, the nuclear propulsion system adopted the conventional direct drive turbines as its propulsion system. A main turbine is used as the prime mover to drive propeller directly via shafts and a reduction gear system in the conventional system. An electric propulsion system offers a relatively straightforward method of cross connecting shafts so as to alleviate the load running of the prime mover when the vessel operates at a reduced speed. High efficiency and compactness are the other important requirements as well in the ship applications. Therefore, an integrated nuclear electric propulsion system lends itself to the best choice to meet these requirements.

In this chapter, study on two different applications of MOBIS power conversion system viz. fusion reactor DEMO and marine propulsion system is discussed. These applications may represent the application of MOBIS for a high power electricity and non electricity utilization in the term of its end connected-load.

## 5.2. Fusion Reactor

The conceptual design of MOBIS may be utilized for another reactor type as well such as fusion reactor. In this chapter, a MOBIS conceptual design is applied for DEMO fusion reactor. The helium-cooled blanket concepts are currently

considered in power plant conceptual study for DEMO. For these plant models, a He-cooled diverter design was investigated as well (Medrano et al., 2007). Table 5-1 lists the parameters of the primary heat transport system (PHTS) for the HCLL model AB. The blanket provides 81.5% of the total thermal power with coolant temperatures from 560 K to 773 K. A more respectable coolant is provided by the divertor that delivers only 18.5% of total thermal power with coolant temperatures from 795 K to 990 K. Both these coolants are coupled to the power conversion system as part of MOBIS.

**Table 5-1. PHTS parameters of DEMO** (Medrano et al., 2007)

| | |
|---|---|
| Fusion power [MW] | 4290 |
| Thermal power to PHTS [MW] | 5145 |
| Total thermal power [MW] | 5509 |
| Thermal power from blanket [MW] | 4219 |
| Thermal power from blanket blower [MW] | 273 |
| Thermal power from diverter [MW] | 926 |
| Thermal power from diverter blower [MW] | 91 |
| Inlet coolant temperature of blanket [K] | 560 |
| Outlet coolant temperature of blanket [K] | 773 |
| Inlet coolant temperature of diverter [K] | 795 |
| Outlet coolant temperature of diverter [K] | 990 |

Several power conversion scenarios have been proposed for the DEMO fusion reactor by Medrano et al. (2007). The supercritical Brayton cycle power conversion system turns out to be a prevailing option from the thermal efficiency point of view. It is expected that the Brayton cycle has higher thermal efficiency than the commercial Rankine cycle (Halimi and Suh, 2010b). Further, the volume of the

whole cycle is expected to shrink by adoption of a supercritical fluid which has higher density than gases. Also needed is optimization of the power conversion system. The footprint of the power plant can consequently be minimized. The cycle thermal efficiency is dictated by arrangement of the components. Therefore, the power conversion system must necessarily be optimized. Considering all of these aspects, an analysis code is being developed to analyze the cycle design and to apply the supercritical driven Brayton cycle to fusion reactor power conversion system as part of MOBIS. This system is based on the recompression Brayton cycle, which basically similar with what is discussed in the previous chapter, as depicted in Figure 5-1. In this cycle the flow is branched into a pre-cooler and a recompressing compressor. Only a fraction of fluid is cooled by the pre-cooler to be compressed in a main compressor. The pinchpoint problem can be prevented by this mechanism. Another feature of this cycle is elimination of the pump, whereby the pump cavitation problem due to supercritical to subcritical phase change can be avoided. S-$CO_2$ is adopted for working fluid of the power conversion system because of its easy acquisition, high density and low chemical reactivity. The output power of the turbine is regulated by control valves. The pressure drop in the control valves is not taken into account in this study to render the problem more tractable.
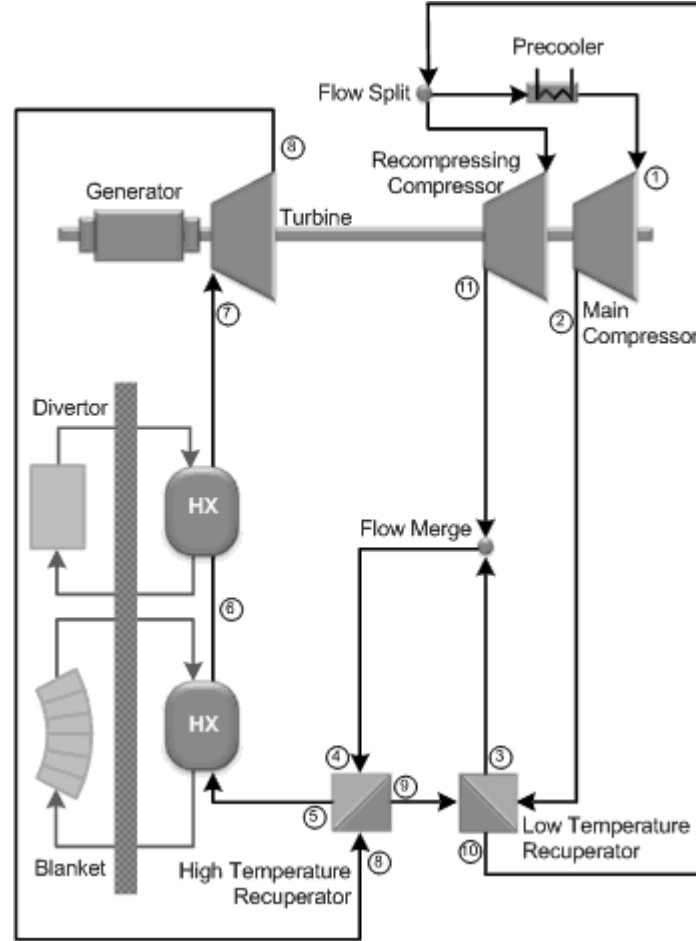
**Figure 5-1. S-CO₂ recompression cycle layout for fusion reactor**

Referring to Figure 5-1, for all the state thermodynamic property calculations, the required thermal power is estimated by using the mass and energy balance equations at the heat exchanger, low temperature recuperator (LTR), and high temperature recuperator (HTR) as follows

$$Q = m_{total} \ (h_7 - h_5) \qquad (5\text{-}1)$$

$$m_r \ (h_3 - h_2) = (h_9 - h_{10}) \qquad (5\text{-}2)$$

$$h_5 - h_4 = h_8 - h_9 \tag{5-3}$$

$$h_4 = m_r h_3 + (1 - m_r)h_{11} \tag{5-4}$$

where $m_{total}$ is the total mass flow rate of S-CO$_2$, $m_r$ is the mass flow separation fraction to LTR, $Q$ is the reactor power, $h$ is the enthalpy, and the subscripted numerals refer to the points of state in Figure 5-1.

The isentropic efficiency of the turbine and compressor, and the effectiveness of the HTR and LTR are proposed to reduce the number of unknown parameters as follows

$$\eta_{turbine} = \frac{h_7 - h_8}{h_7 - h_{8s}} \tag{5-5}$$

$$\eta_{comp\ \#1} = \frac{h_{2s} - h_1}{h_2 - h_1} \tag{5-6}$$

$$\eta_{comp\ \#2} = \frac{h_{11s} - h_{10}}{h_{11} - h_{10}} \tag{5-7}$$

$$\varepsilon_{HTR} = \frac{T_8 - T_9}{T_8 - T_4} \tag{5-8}$$

$$\varepsilon_{LTR} = \frac{T_9 - T_{10}}{T_9 - T_2} \tag{5-9}$$

where subscript $s$ represents the isentropic process, $\eta_{turbine}$ is the turbine efficiency, $\eta_{comp\ \#1}$ and $\eta_{comp\ \#2}$ are the main and the recompression compressor efficiency, and $\varepsilon_{HTR}$ and $\varepsilon_{LTR}$ are the effectiveness of HTR and LTR. The net work and thermal efficiency are calculated as follows

$$W_{net} = m_{total}(h_7 - h_8) - m_{total}\,m_r(h_2 - h_1) - m_{total}(1 - m_r)(h_{11} - h_{10})$$

$$\tag{5-10}$$

$$\eta_{thermal} = \frac{W_{net}}{Q} \qquad\qquad\qquad\qquad (5\text{-}11)$$

where $W_{net}$ is the net generated power, and $\eta_{thermal}$ is the thermal thermal efficiency.

Two kinds of power conversion system layout, recompression cycle without reheating and recompression cycle with reheating, are selected for the computational analysis in this study. The PHTS of DEMO model AB in Table 5-1 is used as the reference. Table 5-2 lists the general input parameters for the two simulations.

**Table 5-2. Input parameters for DEMO**

| | |
|---|---|
| Turbine efficiency [%] | 93 |
| Compressor efficiency [%] | 88 |
| Low temperature recuperator effectiveness [%] | 93 |
| High temperature recuperator effectiveness [%] | 95 |
| Turbine inlet temperature [K] | 683.15 |
| Maximum pressure [MPa] | 20 |
| Minimum temperature [K] | 304.4 |

### 5.2.1. Recompression Cycle without Reheating

The standard recompression cycle without reheating is illustrated in Figure 5-1.For this simulation, the mass flow fraction is set equal to 63%. Considering the maximum coolant temperature of DEMO PHTS model and the critical point of $CO_2$, the maximum temperature and minimum enthalpy are chosen to be 683.15 K and 360.01 kJ/kg-K, respectively, as the boundary conditions. The pressure drop in HTR and LTR on both sides is assumed to be 0.05 MPa. Moreover, the pressure loss in the heat exchangers is set equal to 0.2 MPa on the $CO_2$ side.

Table 5-3 and Figure 5-2 present the state properties and the *T-s* diagram of the simulation result, respectively. The numerals refer to the points as illustrated in Figure 5-1. Note that the coolant is heated up from point 5 to point 6 by the blanket PHTS. By considering the PHTS of divertor, the coolant temperature can be increased from point 6 to point 7. The thermal efficiency and net generated power are 42.44 % and 2,183 MW, respectively. The total mass flow rate is 35,103 kg/s splitting into 22,115 kg/s and 12,988 kg/s.

**Table 5-3. Recompression Brayton cycle calculation results**

| No. | Pressure [MPa] | Temperature [K] | Entropy [J/kg-K] | Enthalpy [kJ/kg] |
|-----|------|--------|---------|--------|
| 1 | 7.40 | 304.40 | 1524.71 | 360.01 |
| 2 | 20.00 | 357.45 | 1528.54 | 387.41 |
| 3 | 19.95 | 460.08 | 2007.89 | 579.57 |
| 4 | 19.95 | 458.81 | 2003.93 | 577.75 |
| 5 | 19.90 | 556.19 | 2259.28 | 706.46 |
| 6 | 19.70 | 659.66 | 2472.23 | 834.42 |
| 7 | 19.50 | 683.15 | 2517.32 | 863.39 |
| 8 | 7.55 | 578.77 | 2530.83 | 760.14 |
| 9 | 7.50 | 464.25 | 2284.25 | 631.44 |
| 10 | 7.45 | 362.79 | 1990.12 | 510.38 |
| 11 | 19.95 | 456.66 | 1997.17 | 574.66 |
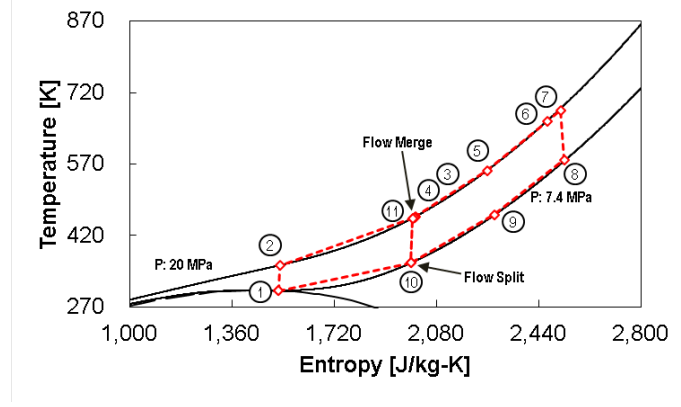
**Figure 5-2.** *T-s* diagram of S-CO$_2$ recompression cycle without reheating

### 5.2.2. Recompression Cycle with Reheating

To enhance the cycle thermal efficiency, the recompression S-CO$_2$ cycle with reheating is considered in this analysis. The reheating concept is widely used in almost all the current steam cycle (Zhao and Peterson, 2008). This concept can help improve the efficiency by increasing the turbine power output through introduction of reheater and low pressure (LP) turbine after the high pressure (HP) turbine (Sarkar and Bhattacharyya, 2009). The recompression S-CO$_2$ cycle with reheating layout for DEMO is shown in Figure 5-3. The inlet temperature of both turbines is assumed to be identical. By manipulating Eqs. (5-1) and (5-10), the required thermal power and net work of the cycle are obtained as follows.

$$Q = m_{total} \left[ (h_7 - h_5) + (h_{10} - h_8) \right] \tag{5-12}$$

$$W_{net} = m_{total} \left[ (h_7 - h_8) + (h_{10} - h_{11}) - m_r(h_2 - h_1) - (1 - m_r)(h_{14} - h_{13}) \right]$$

$$\tag{5-13}$$

130

**Figure 5-3. S-CO₂ recompression cycle with reheating layout**

By using similar data with the system without reheating, Figure 5-4 presents the variation of cycle thermal efficiency and turbine and compressor work. There is no significant effect on the main and recompressing compressor work, whereas HP and LP turbine work output have a contrasting trend in terms of the intermediate pressure effect. Thus, the existing intermediate pressure leads to an optimum thermal efficiency. Based on the optimization result, the intermediate pressure is set equal to 13.325 MPa with the mass flow fraction 63%.

**Figure 5-4. Intermediate pressure optimization**

Figure 5-5 illustrates the *T-s* diagram of the recompressing cycle with reheating. As discussed in the previous case, the coolant is heated up from point 5 to point 6 and from point 6 to point 7 by the blanket and diverter PHTS, respectively. But by adopting the reheating concept, the flow exiting the HP turbine (point 8) is reheated to maximum cycle temperature (point 10) through the blanket and diverter PHTS and then expanded to point 11 through the LP turbine. In this cycle, the HP turbine and LP turbine work are 1,411 MW and 2,229 MW, respectively. This result can enhance the net power of the recompression cycle without reheating by 1.56% to 2,217 MW, and the thermal efficiency of 43.1% can be attained.
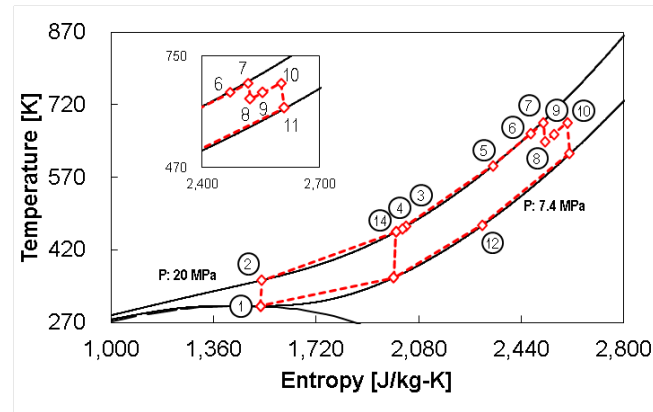
**Figure 5-5.** *T-s* diagram of S-CO$_2$ recompression cycle with reheating

## 5.3. Marine Propulsion System

For a long time, nuclear propulsion ships have relied on proven pressurized-water nuclear propulsion system as illustrated in Figure 5-6. Based on literatures, it has been about forty years since nuclear powered merchant ships were seriously discussed in the naval architecture community. But recent developments in commercial shipping include bigger, faster, and more powerful ships, where nuclear propulsion may be an option worth considering (Vergara and McKesson, 2002).

For power conversion cycle in nuclear marine application, a direct Brayton cycle was studied as one alternative for design of a marine nuclear power plant (Gathy, 1967). This study adopted a gas–cooled reactor, gas turbines and a waste-heat boiler which were incorporated to provide heat energy, propulsive power and auxiliary system, respectively. It concluded that compared to the conventional steam plant, the nuclear plant is more compact in term of area, volume, and also weight.

133
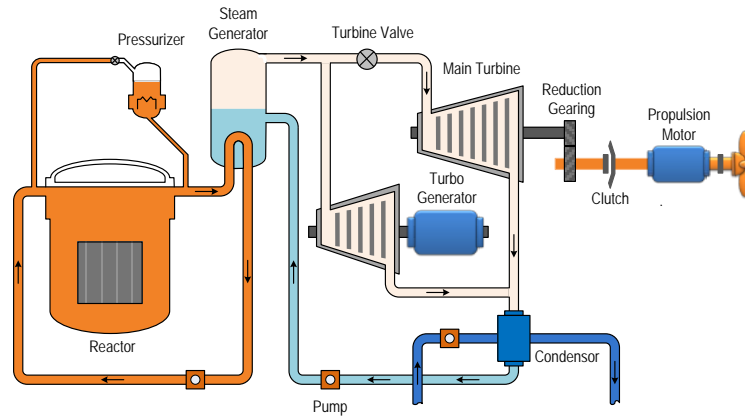
**Figure 5-6 Typical Pressurized-Water Naval Nuclear propulsion system**

The Naval Application Vessel Integral System (NAVIS) adopts a different propulsion system. The general scheme of NAVIS is shown in Figure 5-7. It is designed to suit the requirement of a compact, simple, safe and innovative integral fast reactor system. It is powered by BORIS as the main power source. As presented in Chapter 2, BORIS is being developed as a general multipurpose small modular reactor. It is being designed to generate 10 MW of electricity for at least twenty consecutive years without refueling and also to meet the Generation IV Nuclear Energy System goals of sustainability, safety, reliability, and economics.

Considering the efficiency and compactness, NAVIS adopted a Brayton cycle MOBIS with supercritical fluid which has higher density than gases as working fluid. For the propulsion part, NEPA has three foremost parts: power generating and distributing system, power electronic converter, and electric propulsion motor, as described in Figure 5-7. A High Temperature Superconductor (HTS) motor is selected as the propulsion motor to attain much higher in term of efficiency. The motor is driven by a natural commutation power electronics converter motor drive system which consists of a rectifier and an inverter. Consequently, the motor drive

system does not require a complex and costly force commutating control circuits.

The rectifier which works to convert the standard alternating current (AC) generated by the generator to a direct current (DC) form. To do this task, it is equipped with six thyristor power electronics switches. By adopting this rectifier type, the output current of rectifier can be controlled easily by controlling the firing angle value of rectifier. Whereas the inverter has a function in the opposite way with rectifier. It is designed to convert the DC form to a variable AC based on the desired motor speed signal control. Both of these converters are connected each other via a DC filter to minimize the power harmonics of the system.
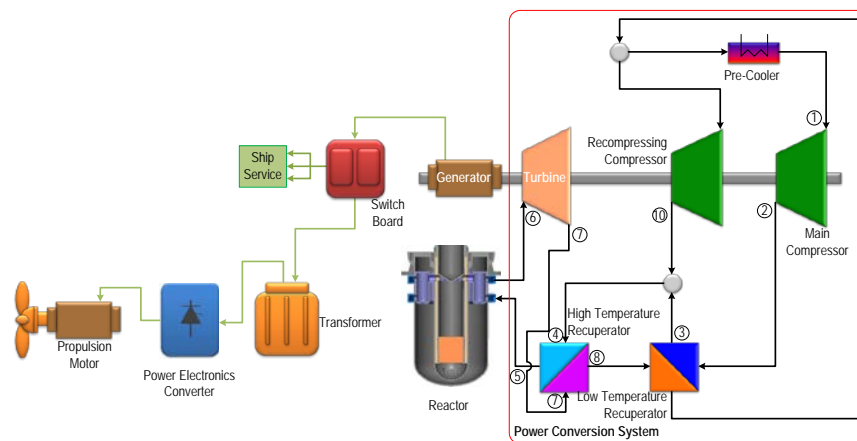


**Figure 5-7. Naval Application Vessel Integral System (NAVIS).**

### 5.3.1. Propulsion System

The propulsion system NEPA can be schematically elaborated as shown in Figure 5-8. This electric propulsion system utilizes two main control loops to generate the control signal for driving the propulsion motor. The outer loop is a speed loop control part which works based on controlling the error between the outermost reference signal, speed reference, and the actual speed which can be obtained from the available speed sensor. Then, this speed loop will generate a reference signal as

the reference for the inner (current) loop. Based on the error value between the current reference and the actual current, the current controller can generate the firing angle value as the control signal for all of the rectifier power electronics switches. Meanwhile the firing angle of inverter is also controlled by referring the current reference signal and the actual speed from the speed sensor. This controlling process can be done by using gate signals that are based on the cosine comparator firing the control strategy. Particularly, it can be easily defined as follows

$$c_a(\theta) = \cos\theta \tag{5-14}$$

$$c_b(\theta) = \cos\left(\theta - \frac{2\pi}{3}\right) \tag{5-15}$$

$$c_c(\theta) = \cos\left(\theta + \frac{2\pi}{3}\right) \tag{5-16}$$

The switching control strategy for the inverter is

$$T_1: \big(c_c(\theta) < c_a(\theta)\big) \cdot \big(c_c(\theta) < c_b(\theta)\big) \tag{5-17}$$

$$T_2: \big(c_a(\theta) > c_b(\theta)\big) \cdot \big(c_a(\theta) > c_c(\theta)\big) \tag{5-18}$$

$$T_3: \big(c_b(\theta) < c_a(\theta)\big) \cdot \big(c_b(\theta) < c_c(\theta)\big) \tag{5-19}$$

$$T_4: \big(c_c(\theta) > c_a(\theta)\big) \cdot \big(c_c(\theta) > c_b(\theta)\big) \tag{5-20}$$

$$T_5: \big(c_a(\theta) < c_b(\theta)\big) \cdot \big(c_a(\theta) < c_c(\theta)\big) \tag{5-21}$$

$$T_6: \big(c_b(\theta) > c_a(\theta)\big) \cdot \big(c_b(\theta) > c_c(\theta)\big)$$

$$\tag{5-22}$$
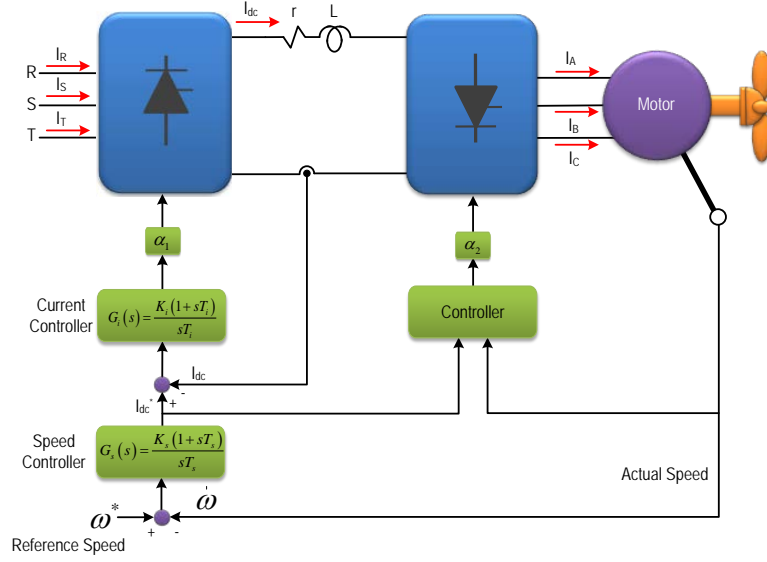
**Figure 5-8. Propulsion motor drive**

Furthermore, NEPA considers to attain the higher efficiency by adopting a four-pole, three-phase HTS synchronous motor as the propulsion motor. To deal with the complicated magnetic coupling between the three-phase variables, a transformation of the three-phase windings to orthogonal axis *d-q* winding is adopted for motor modeling, as described in Figure 5-9. By using this transformation, the motor can be expressed as

$$u_{ds} = R_s i_{ds} + \frac{d}{dt} \lambda_{ds} - \omega_r \lambda_{qs} \qquad (5\text{-}23)$$

$$u_{qs} = R_s i_{qs} + \frac{d}{dt} \lambda_{qs} + \omega_r \lambda_{ds} \qquad (5\text{-}24)$$

$$\lambda_{ds} = \Lambda_{ds} i_{ds} + \Lambda_{dm} i_f' \qquad (5\text{-}25)$$

137

$$\lambda_{qs} = \Lambda_{qs}\, i_{qs} \tag{5-26}$$

where

$$i_f' = \frac{2}{3}\frac{Nw_{ws}}{Nw_{wf}}\, i_f$$

The electromagnetic torque can be written as

$$T_e = \frac{3}{2}\left(\frac{P}{2}\right)\left(\lambda_{ds}\, i_{qs} - \lambda_{qs}\, i_{ds}\right) \tag{5-27}$$
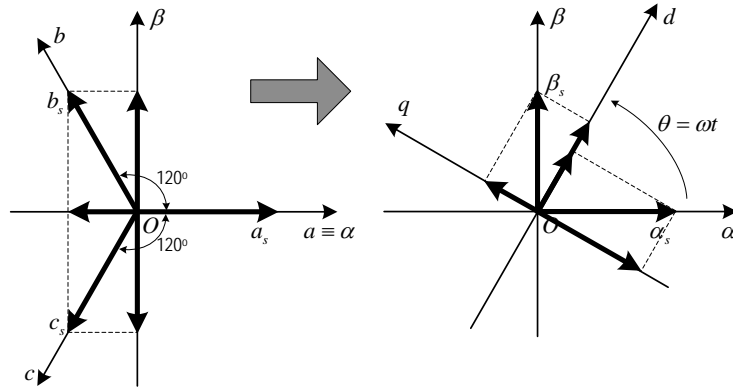


**Figure 5-9. Transformation of three-phase to rotating coordinate system**

### 5.3.2. Dynamic Simulation

To simulate the propulsion system, a four pole synchronous HTS motor with parameters as listed in Table 5-4 is selected in this study. As the controllers, simple proportional integrator (PI) controllers are chosen to control the speed and current. The constant values of the PI controller are $K_s = 0.1$, $K_i = 0.05$, $T_s = 2/s$ and $T_i = 0.3/s$.

Figure 5-10 shows the dc output current of rectifier ($I_{dc}$) and the inverter ac output current ($I_A$, $I_B$, and $I_C$). The ac output current of the inverter is a square waveform instead of a sinusoidal waveform. The peak to peak value of this current equals to the magnitude of the rectifier dc output current.

To illustrate the dynamic response of the control system, a step-down and step-up speed reference is applied as shown in Figure 5-11. In this simulation, the 0.2 step-down reference signal is applied at $t = 18$ s and the system gives a response without overshooting. At $t = 24$ s, the reference is stepped up by 0.3 times and the system responds quite well without overshooting as well.

**Table 5-4. Propulsion Motor**

| | |
|---|---|
| Nominal Power [MW] | 4 |
| Rated Phase Voltage [V] | 2400 |
| Rated Speed [rpm] | 230 |
| Frequency at Rated Speed [Hz] | 11.5 |
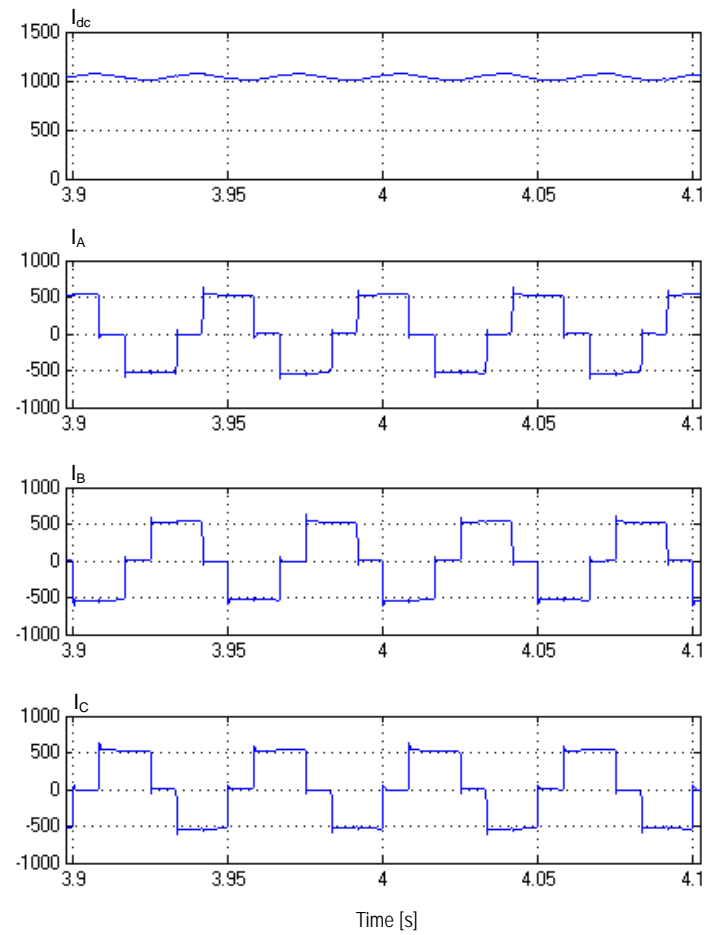
**Figure 5-10. Steady state dc-ac currents waveform of converters**
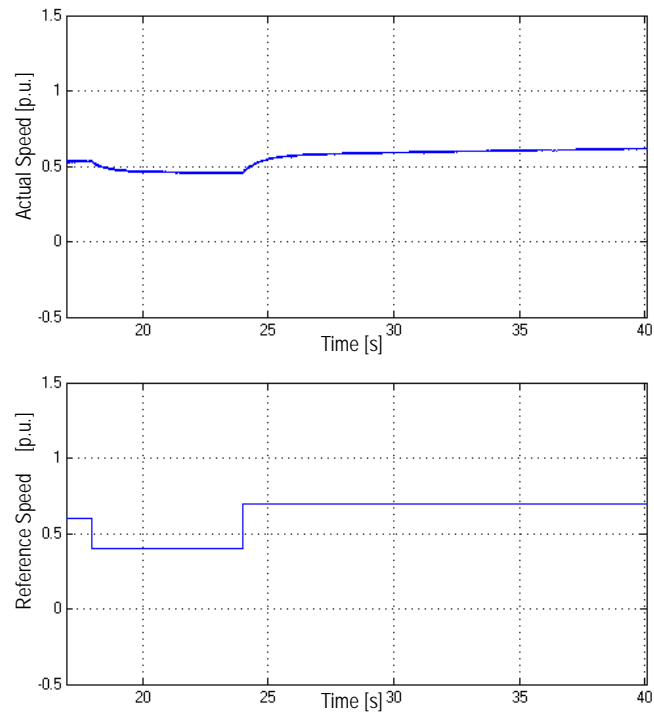
**Figure 5-11. Dynamic response**

# 6. CONCLUSIONS AND FUTURE WORK

## 6.1. Conclusions

A high efficiency power conversion system is the main goal of this research. To realize this goal, an S-CO$_2$ recompression Brayton cycle was adopted to get benefit from the CO$_2$ physical properties change near its critical point to enhance the thermal efficiency. To improve the thermal efficiency and system performance, the combined valve and also the compensation of valve nonlinearity characteristic were analyzed. Both of these improvement methods can be adopted for the commercial steam Rankine cycle or another supercritical cycle such as the S-CO$_2$ recompression Brayton cycle which is one of prospective candidates for next generation nuclear reactors.

Moreover, the works and accomplishments of this research can be listed as follows

1.  A computational analysis has been performed on the S-CO$_2$ Brayton cycle power conversion system for small modular reactor type BORIS and fusion reactor DEMO. The OSCA code was developed to analyze the cycle design by applying the S-CO$_2$ driven Brayton cycle to BORIS as well DEMO as part of MOBIS. By considering the piping system pressure drop, a 42.50% efficiency can be attained for the system driven by BORIS.

    In the preliminary design of fusion reactor power conversion system, the HCLL model AB of DEMO was used as reference. The computational analysis result showed that a thermal efficiency of 42.44 % is obtained by adopting the recompression S-CO$_2$ Brayton cycle. By adding the reheating concept, some 0.66% additional benefits can be achieved in terms of the cycle thermal efficiency.

2.  The computational and experimental work has been done for the combined stop and control valve system. The flow coefficient of the combined valve was calculated by CFX as part of the in-house CARA analysis and CARO experiment. The computational results are in good agreement with the experimental ones. Application of the combined valve to commercial steam turbine system was examined computationally by adopting the obtained flow coefficient results. The computational analysis demonstrated that the efficiency can be improved by 1.27% compared against the conventional system by taking on the combined valve. The combined valve is found to not only reduce the pressure loss but also minimize the footprint of the turbine system. Moreover, the combined valve was also computationally analyzed for the prospective $S\text{-}CO_2$ recompression Brayton cycle MOBIS. By applying this combined valve to MOBIS, the efficiency of power conversion system can be improved from 41.58% to be 42.01%. This improvement may be much higher in the power conversion system with higher output power.

3.  The computational analysis VELA has been presented for nonlinearity characteristic compensation of the steam turbine control valve. The standard analysis code MARS was utilized to obtain more accurate simulations in the thermalhydraulic point of view without sacrificing the control engineering aspects. Three different scenarios of Ulchin Units 3&4 have been analyzed by considering the control valves opening sequence mechanism and the change rate of output power reference. The computational results demonstrate that the nonlinearity characteristic compensation can notably suppress the transient errors by more than 90% for all the cases studied.

## 6.2. Future Work

There are some important issues which still not covered in this work such as transient analysis of power conversion system, compensation of another inherent valve nonlinearity characteristic and integration of power conversion system and electrical system. Considering their crucial aspects, it is suggested to take them into account as the future work of this research.

### 6.2.1. Extended Transient Analysis

The current OSCA was developed as steady state analysis code. Although it can be utilized as design tool, it is still not applicable to simulate the transient phenomena in recompression Brayton cycle with S-CO$_2$ as working fluid. In the future work, it is necessary to upgrade the code for dealing with transient scenarios. For this purpose, additional analysis on the system components will be carried out to obtain characteristics under transient environment.

### 6.2.2. Compensation of Stiction Nonlinearity Characteristic

As discussed in previous chapter, valves have vital function to control the power conversion cycle. Unfortunately, the valves carry another inherent static friction (stiction) nonlinearity characteristics (Clark et al., 2004). Also, industrial surveys indicated that 20~30% of all the control loops oscillate due to valve problem caused by this nonlinear characteristic.

According to the Instrument Society of America (ISA), stiction is defined as the resistance to the start of motion, usually measured as the difference between the driving values required to overcome static friction upscale and downscale. In a control valve, stiction exists when the static friction exceeds the dynamic friction inside the valve.

A simple relationship between the valve input (controller output) and the valve output (valve position) is shown in Figure 6-1. The dashed line denotes the equilibrium states. In these states, total forces on the diaphragm are balance. The input and output of valve change in an ideal situation along this line without any friction.

In the case a friction arises, the relationship of valve input and output is disturbed. As shown in Figure 6-1, the relationship of input-output of a valve that suffering from stiction is described by the solid line. It consists of four main parts i.e. deadband, stickband, slipjump, and the moving phase. For example, the valve comes to rest or changes the position at point A, the valve sticks. If the input of the valve (the controller output) overcomes the valve deadband and the valve stickband, AB and BC respectively, the valve jumps to a new position (D) and continue to move. The valve may stick again in between points D and E due to a very low or zero velocity.
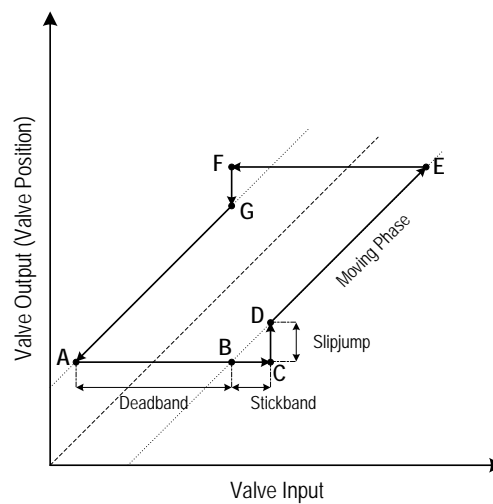


Figure 6-1. Relationship between input and output of a valve

145

Considering this inherent nonlinear characteristic, the compensation of stiction characteristic is necessary to be investigated in next research.

### 6.2.3. Coupled Power Conversion System and Electric Propulsion System Simulation

The current analysis of NAVIS is still relied on separated OSCA code and another commercial power electronics analysis software to analyze the power conversion system and electric propulsion system, respectively. By upgrading the capability of OSCA code for transient analysis in the same platform with the electric propulsion system analysis software, the dynamic analysis of both system can be simultaneously performed.

# NOMENCLATURE

| | | |
|---|---|---|
| $A$ | : area | [m$^2$] |
| $b$ | : impeller width | [m] |
| $b^*$ | : ratio of vaneless diffuser inlet width to impeller exit width | |
| $C_f$ | : skin friction coefficient | |
| $C_p$ | : specific heat | [J/kg K] |
| $D$ | : diameter | [m] |
| $D_s$ | : specific diameter | [m] |
| $D_f$ | : diffusion factor | |
| $D_{hyd}$ | : impeller average hydraulic diameter | [m] |
| $d$ | : pipe diameter | [m] |
| $e$ | : error | |
| $f$ | : friction factor | [m/s] |
| $G$ | : transfer function | |
| $h$ | : enthalpy | [J/kg] |
| $i$ | : current | [A] |
| $J_T$ | : transient tracking error | |
| $K_i$ | : proportional constant of current controller | |
| $K_s$ | : proportional constant of speed controller | |
| $L$ | : pipe length | [m] |
| $L_b$ | : impeller flow length | [m] |

| $L_\theta$ | : impeller meridional length | [m] |
| $m$ | : mass flow rate | [kg/s] |
| $N$ | : number of channel | |
| $NC$ | : number of curves in one channel | |
| $NP$ | : number of ducts in parallel | |
| $NS$ | : number of duct sections in series | |
| $N_s$ | : specific speed | [rpm] |
| $Nw$ | : number of winding | |
| Nu | : Nusselt number | |
| $P$ | : number of poles | |
| Pr | : Prandtl number | |
| $Q$ | : reactor power | [MWt] |
| $R$ | : resistance | [ohm] |
| Re | : Reynold number | |
| $r$ | : radius | [m] |
| $T$ | : temperature | [K] |
| $T_i$ | : integrator time constant of current controller | [s$^{-1}$] |
| $T_s$ | : integrator time constant of speed controller | [s$^{-1}$] |
| $t$ | : time | [s] |
| $U$ | : tangential impeller speed | [m/s] |
| $u$ | : voltage | [V] |
| $v$ | : specific volume | [m$^3$/kg] |

| $W_{net}$ | : net power | [MW] |
|---|---|---|
| $Z$ | : number of blades | |
| $z$ | : compressibility factor | |

*Greek Letter*

| $\alpha$ | : absolute flow angle | [deg] |
|---|---|---|
| $\Delta$ | : delta | |
| $\eta$ | : efficiency | |
| $\varepsilon$ | : effectiveness | |
| $\gamma$ | : specific heat ratio | |
| $\Lambda$ | : inductance | [H] |
| $\lambda$ | : magnetic flux | [Vs] |
| $\mu$ | : dynamic viscosity | [Pa s] |
| $\rho$ | : density | [kg/m$^3$] |
| $\psi$ | : uncertainty | |
| $\omega$ | : angular velocity | [rad/s] |
| $\xi$ | : form loss | |

*Subscripts*

| $ds$ | : direct axes |
|---|---|
| $h$ | : hydraulic |
| $LMTD$ | : log mean temperature difference |

149

*m1m* : meridional direction at impeller inlet

*qs* : quadrature axes

*r* : split ratio

*s* : isentropic process

*rc* : recirculation

*u* : tangential direction

*wf* : field winding

*ws* : stator winding

# REFERENCES

Aguiar, A.P., Hespanha, J.P., Kokotović, P.V., 2008. Performance limitations in reference tracking and path following for nonlinear systems. Automatica 44, 598-610.

Amirante, R., Del Vescovo, G., Lippolis, A., 2006. Evaluation of the flow forces on an open centre directional control valve by means of a computational fluid dynamic analysis. Energy Convers. Manage. 47, 1748-1760.

Aragón-Camarasa, G., Aragón-González, G., Canales-Palma, A., León-Galicia, A., 2009. Experimental determination of the flow capacity coefficient for control valves of process. Lat. Am. Appl. Res. 39, 57-63.

Araki, T., Kuwashima, H., 1984. Combined valve, US Patent, Patent No. 4481776, US.

Aungier, R., 1995. Mean streamline aerodynamic performance analysis of centrifugal compressors. J. Turbomach. 117, 360.

Balje, O.E., 1981. Turbomachines: A guide to design selection and theory. Wiley & Sons, Inc.

Barinberg, G., Valamin, A., Kultyshev, A., Ivanovskii, A., Sakhnin, Y., 2011. New draft projects of steam turbines for combined-cycle plants. Therm. Eng. 58, 15-20.

Bentivoglio, F., Tauveron, N., Geffraye, G., Gentner, H., 2008. Validation of the CATHARE2 code against experimental data from Brayton-cycle plants. Nucl. Eng. Des. 238, 3145-3159.

Boss, M., 1996. Steam turbines for STAG combined-cycle power systems GE Power Generation Turbine   Technology Reference Library GER-3582D.

Byerly, R., 1973. Dynamic models for steam and hydro turbines in power system studies. IEEE Trans. Power Appar. Syst., 1904-1915.

Callan, P.C., 1963. Electric compensation of valve flow nonlinearities in large steam turbine, The American Society of Mechanical Engineering Winter Annual Meeting, Philadelphia, PA, US.

Chang, Y.I., Konomura, M., Pinto, P.L., 2007. A case for small modular fast reactor. J. Nucl. Sci. Technol. 44, 264-269.

Chase, D.L., Kenhoe, P.T., GE combined-cycle product line and performance. GE Power Generation Turbine Technology Reference Library GER-3574G.

Chen, L.-G., Zheng, J.-L., Sun, F.-R., Wu, C., 2003. Power, power density and efficiency optimization for a closed cycle helium turbine nuclear power plant. Energy Convers. Manage. 44, 2393-2401.

Choi, I.-K., Kim, J.-A., Jeong, C.-K., Woo, J.-H., Choi, J.-Y., Son, G., 2009. Development of a digital turbine control system in a nuclear power plant. Int. J. Control, Autom. Syst. 7, 67-73.

Cinotti, L., Smith, C.F., Sekimoto, H., Mansani, L., Reale, M., Sienicki, J.J., 2011. Lead-cooled system design and challenges in the frame of Generation IV International Forum. J. Nucl. Mater. 415, 245-253.

Clark, R., Holstrom, J., Ravelo, W., Sekula, B., 2004. Turbine steam valve diagnostic testing. EPRI, Palo Alto, CA, US.

Clark, R.B., Jensen, J.K., Miyayashiki, H.M., Ofuji, T., 1999. Combined valve configuration for steam cycle units, US Patent, Patent No. 5870896, US.

Conrad, O., Raif, K., Wessels, M., 1980. The calculation of performance maps for centrifugal compressors with vane-island diffusers, 25th ASME Annual

International Gas Turbine Conference and 22nd ASME Annual Fluids Engineering Conference on Performance Prediction of Centrifugal Pumps and Compressors, New Orleans, LA, pp. 135-147.

Coppage, J., Dallenbach, F., Eichenberger, J., Hlavaka, G., Knoernschild, E., Vanke, N., 1956. Study of supersonic radial compressors for refrigeration and pressurization systems. AiResearch Mfg. Co., Los Angeles. WADC-TR-55-257.

Daily, J.W., Nece, R.E., 1960. Chamber dimension effects on induced flow and frictional resistance of enclosed rotating disks. J. Basic Eng. 82, 217.

De Pauw, D.J.W., Vanrolleghem, P.A., 2006. Practical aspects of sensitivity function approximation for dynamic models. Math. Comput. Modell. Dyn. Syst. 12, 395-414.

Dostal, V., 2004. A supercritical carbon dioxide cycle for next generation nuclear reactors. Massachusetts Institute of Technology.

Dostal, V., Hejzlar, P., Driscoll, M.J., 2006a. High-performance supercritical carbon dioxide cycle for next-generation nuclear reactors. Nucl. Technol. 154, 265-282.

Dostal, V., Hejzlar, P., Driscoll, M.J., 2006b. The supercritical carbon dioxide power cycle: Comparison to other advanced power cycles. Nucl. Technol. 154, 283-301.

Eggenberger, M.A., Ipsen, P.G., Schenectady, N.Y., Troutman, P.H., 1968. Full arc-partial arc transfer system for electrohydraulic turbine control, US Patent, Patent No. 3403892, US.

Eggenberger, M.A., Troutman, P.H., Callan, P.C., Schenectady, N.Y., 1963. Turbine control system, US Patent, Patent No. 3097488, US.

EPRI, 2006. Introduction to nuclear plant steam turbine control systems.

Fu, W.-S., Ger, J.-S., 1998. A concise method for determining a valve flow coefficient of a valve under compressible gas flow. Exp. Therm. Fluid Sci. 18, 307-313.

Fujii, H., Kimura, T., Segawa, K., 2007. A high-efficiency steam turbine utilizing optimized reaction blades. Hitachi Review 56, 104-108.

Fuller, R., Preuss, J., Noall, J., 2012. Turbomachinery for supercritical CO2 power cycles, ASME Turbo Expo, Copenhagen, Denmark.

Gathy, B.S., 1967. Design of A Marine Nuclear Power Plant Utilizing The Direct Brayton Cycle. Nav. Eng. J. 79, 887-895.

Gerdes, R., Padfield, R., Suter, F., 2003. Valve arrangement for a power plant, US Patent, Patent No. 6638014 B2, US.

Grace, A., Frawley, P., 2011. Experimental parametric equation for the prediction of valve coefficient (Cv) for choke valve trims. Int. J. Pres. Ves. Pip. 88, 109-118.

Halimi, B., Suh, K.Y., 2010a. Control engineering of steam turbine valve, The 8th International Topical Meeting on Nuclear Thermal Hydraulics, Operation and Safety (NUTHOS-8), Shanghai, China.

Halimi, B., Suh, K.Y., 2010b. Engineering design of supercritical Brayton cycle, The 8th International Topical Meeting on Nuclear Reactor Thermal Hydraulics, Operation and Safety (NUTHOS), Shanghai, China.

Hassan, F.F., Balasubramanian, R., Bhatti, T.S., 1999. Fast valving scheme using parallel valves for transient stability improvement. IEE Proc.-Gener. Transm. Distrib, pp. 330-336.

Hejzlar, P., Dostal, V., Driscoll, M., Dumaz, P., Poullennec, G., Alpy, N., 2006a.

Assessment of gas cooled fast reactor with indirect supercritical CO2 cycle. Nucl. Eng. Technol. 38, 109-118.

Hejzlar, P., Driscoll, M., Gong, Y., Kao, S., 2006b. Supercritical CO2 Brayton Cycle for Medium Power Applications. MIT-ANP-PR-117, MIT.

Hesselgreaves, J.E., 2001. Compact heat exchangers: Selection, design, and operation. Pergamon Pr.

Hoffelner, W., Bratton, R., Mehta, H., Hasegawa, K., Morton, D.K., 2011. New Generation Reactors. ASME Press.

Holcomb, D.E., Peretz, F.J., Qualls, A., 2011. Advanced high temperature reactor systems and economics analysis. ORNL/TM-2011/364, Oak Ridge National Laboratory, Oak Ridge, TN (September 2011).

Holman, J., 2001. Experimental methods for engineers. McGraw-Hill, New York.

Hountalas, D.T., Mavropoulos, G.C., Katsanos, C., Knecht, W., 2012. Improvement of bottoming thermal efficiency and heat rejection for HD truck applications by utilization of EGR and CAC heat. Energy Convers. Manage. 53, 19-32.

IEC, I.E.C., 1998. Industrial-process control valves – Part 2-1: Flow-capacity-sizing equations for fluid flow under installed conditions.

Ishiyama, S., Muto, Y., Kato, Y., Nishio, S., Hayashi, T., Nomoto, Y., 2008. Study of steam, helium and supercritical CO2 turbine power generations in prototype fusion power reactor. Prog. Nucl. Energy 50, 325-332.

Ishizuka, T., Kato, Y., Muto, Y., Nikitin, K., Ngo, T., 2006. Thermal-hydraulic characteristics of a printed circuit heat exchanger in a supercritical CO2 loop. Bulletin-Research Laboratory for Nuclear Reactors 30, 109.

Jansen, W., 1967. A method for calculating the flow in a centrifugal impeller when

entropy gradients are present, Royal Society Conference on Internal Aerodynamics (Turbomachinery), pp. 133-146.

Jensen, J.K., Schenectady, N.Y., 1969. Electrohydraulic control with throttle pressure compensator, USA Patent, Patent No. 3572958, US.

Jeong, W.S., 2010. Optimization study on supercritical carbon dioxide Brayton cycle for small modular reactor, Department of Energy Systems Engineering. Seoul National University.

Johnson, G.A., 2011. Power conversion system evaluation for the next generation nuclear plant. Nucl. Technol. 175, 371-387.

Johnston, J.P., Dean Jr., R.C., 1966. Losses in vaneless diffusers of centrifugal compressors and pumps. Analysis, Experiment, and Design. Trans. ASME, J. Eng. Power 88, 49-62.

Johnston, T., Levy, W., Rumbold, S., 2001. Application of printed circuit heat exchanger technology within heterogeneous catalytic reactors, American Institute of Chemical Engineers Annual Meeting. American Institute of Chemical Engineers, Reno, NV, US.

KAERI, 2006a. MARS code manual volume I: Code structure, system models, and solution methods. Korea Atomic Energy Research Institute, Daejeon, Korea.

KAERI, 2006b. MARS code manual volume II: Input requirements. Korea Atomic Energy Research Institute, Daejeon, Korea.

KAERI, 2006c. MARS code manual volume IV: Developmental assessment report. Korea Atomic Energy Research Institute, Daejeon, Korea.

Kang, S.G., Gu, J.Y., Suh, K.Y., 2008. Linearization of valve flow nonlinearities for large steam turbines, The 6th Japan–Korea Symposium on Nuclear Thermal

Hydraulics and Safety (NTHAS), Okinawa, Japan.

Kang, S.G., Gu, J.Y., Suh, K.Y., 2009. Control adaptive linearized analysis for gas turbine system, The 17th International Conference on Nuclear Engineering (ICONE), Brussels, Belgium.

Kang, S.G., Suh, K.Y., 2009. Linearization of valve flow characteristics for steam turbine control, The 13th International Topical Meeting on Nuclear Reactor Thermal Hydraulics (NURETH), Kanazawa City, Ishikawa Prefecture, Japan.

KEPCO, 1996. Ulchin units 3&4 final safety analysis report. Korea Electric Power Corporation, Seoul, Korea.

Kim, K.S., Suh, K.Y., 2009. Linearized valve flow characteristics for steam turbine control, The American Nuclear Society Winter Meeting, Washington, DC, US.

Konishi, S., Nishio, S., Tobita, K., 2002. DEMO plant design beyond ITER. Fusion Eng. Des. 63–64, 11-17.

Koster, A., Matzner, H.D., Nicholsi, D.R., 2003. PBMR design for the future. Nucl. Eng. Des. 222, 231-245.

Lee, S.G., 1988. Turbine control system, ISL Winter Workshop.

Leĭzerovich, A.S., 2008. Steam turbines for modern fossil-fuel power plants. The Fairmont Press, Inc.

Lemmon, E.W., Huber, M.L., McLinden, M.O., 2002. NIST Reference Fluid Thermodynamic and Transport Properties–REFPROP. NIST standard reference database 23.

Lemmon, E.W., McLinden, M.O., Huber, M.L., 2007. REFPROP: Reference fluid thermodynamic and transport properties. NIST standard reference database 23.

Linares, J.I., Herranz, L.E., Moratilla, B.Y., Serrano, I.P., 2011. Power conversion systems based on Brayton cycles for fusion reactors. Fusion Eng. Des. 86, 2735-2738.

Long, C., Guan, J., 2011. A method for determining valve coefficient and resistance coefficient for predicting gas flowrate. Exp. Therm. Fluid Sci. 35, 1162-1168.

Ma, Z., Turchi, C., 2011. Advanced supercritical carbon dioxide power cycle configurations for use in concentrating solar power systems, Supercritical CO2 Power Cycle Symposium, Boulder, Colorado.

Maisonnier, D., Campbell, D., Cook, I., Di Pace, L., Giancarli, L., Hayward, J., Li Puma, A., Medrano, M., Norajitra, P., Roccella, M., 2007. Power plant conceptual studies in Europe. Nucl. Fusion 47, 1524-1532.

Maisonnier, D., Cook, I., Pierre, S., Lorenzo, B., Luigi, D.P., Luciano, G., Prachai, N., Aldo, P., 2006. DEMO and fusion power plant conceptual studies in Europe. Fusion Eng. Des. 81, 1123-1130.

Malang, S., Schnauder, H., Tillack, M.S., 1998. Combination of a self-cooled liquid metal breeder blanket with a gas turbine power conversion system. Fusion Eng. Des. 41, 561-567.

Medrano, M., Puente, D., Arenaza, E., Herrazti, B., Paule, A., Branas, B., Orden, A., Dominguez, M., Stainsby, R., Maisonnier, D., Sardain, P., 2007. Power conversion cycles study for He-cooled reactor concepts for DEMO. Fusion Eng. Des. 82, 2689-2695.

Mello, F.P.D., Anderson, P., Doudna, J., Fish, J.H., Hamm, P.A.L., Hammons, T.J., Hurley, J.D., Kundur, P., Schulz, R., Tandy, G., Taylor, C.W., Youkins, T., 1991. Dynamic models for fossil fueled steam units in power system studies. IEEE Trans. Power Syst. 6, 753-761.

Moisseytsev, A., Sienicki, J.J., 2006. Development of a plant dynamics computer code for analysis of a supercritical carbon dioxide Brayton cycle energy converter coupled to a natural circulation lead-cooled fast reactor. ANL-06/27, Argonne National Laboratory (ANL).

Moisseytsev, A., Sienicki, J.J., 2008. Transient accident analysis of a supercritical carbon dioxide Brayton cycle energy converter coupled to an autonomous lead-cooled fast reactor. Nucl. Eng. Des. 238, 2094-2105.

Nikitin, K., Kato, Y., Ngo, L., 2006. Printed circuit heat exchanger thermal–hydraulic performance in supercritical CO2 experimental loop. Int. J. Refrig. 29, 807-814.

Oberle, A., 1974. Combined emergency stop and governor valve for controlling fluid flow to a turbo-machine, US Patent, Patent No. 3809126, US.

Oberle, A., 1978. Combined stop and control valve, US Patent, Patent No. 4114652, US.

Oh, C., 2005. Brayton cycle for high temperature gas-cooled reactors. Nucl. Technol. 149.

Oh, C.H., Barner, R., Davis, C., Sherman, S., 2006. Evaluation of working fluids in an indirect combined cycle in a very high temperature gas-cooled reactor. Nucl. Technol. 156, 1-10.

Patel, R., Bhatti, T., Kothari, D., 2002. MATLAB/Simulink-based transient stability analysis of a multimachine power system. International Journal of Electrical Engineering Education 39, 320-336.

Patel, T.S.B.D.P.K.R., 2001. Improvement of power system transient stability using fast valving: A review. Electr. Pow. Comp. Syst. 29, 927-938.

Pirouzmand, A., Halimi, B., Suh, K.Y., 2010. Engineering of control valve mass flow rate in steam turbine system, The 7th International Conference on Flow Dynamics, Sendai, Japan.

Pocock, R.F., 1970. Nuclear ship propulsion. Ian Allan Ltd., UK.

Polyzakis, A.L., Koroneos, C., Xydis, G., 2008. Optimum gas turbine cycle for combined cycle power plant. Energy Convers. Manage. 49, 551-563.

Pra, F., Tochon, P., Mauget, C., Fokkens, J., Willemsen, S., 2008. Promising designs of compact heat exchangers for modular HTRs using the Brayton cycle. Nucl. Eng.Des. 238, 3160-3173.

Rodgers, C., 1979. Specific speed and efficiency of centrifugal impellers. Performance prediction of centrifugal pumps and compressors, 191-200.

Sarkar, J., Bhattacharyya, S., 2009. Optimization of recompression S-CO2 power cycle with reheating. Energy Convers. Manage. 50, 1939-1945.

Schoder, K., Hasanovic, A., Feliachi, A., 2003. PAT: a power analysis toolbox for MATLAB/Simulink. IEEE Trans. Power Syst. 18, 42-47.

Seong, S.H., Lee, T.H., Kim, S.O., 2009. Development of a simplified model for analyzing the performance of KALIMER-600 coupled with a supercritical carbon dioxide Brayton energy conversion cycle. Nucl. Eng. Technol. 41, 785-796.

Sienicki, J., 2012. Lead-Cooled Fast Reactors Fast Spectrum Reactors, in: Waltar, A.E., Todd, D.R., Tsvetkov, P.V. (Eds.). Springer US, pp. 513-532.

Son, H.M., Halimi, B., Suh, K.Y., 2011. Quick design method for lead cooled battery-reactor BORIS, ASME 2011 Small Modular Reactors Symposium, Washington, DC, US.

Son, H.M., Suh, K.Y., 2011. Evolutionary design of reactor vessel assembly for

liquid metal cooled battery. Prog. Nucl. Energy 53, 825-830.

Stanitz, J.D., 1952. One-dimensional compressible flow in vaneless diffusers of radial-and mixed-flow centrifugal compressors, including effects of friction, heat transfer and area change, NACA TN 2610.

Steenburgh, J.H., Clark, R.B., Porteous, N.D., 2003. Combined stop and control valve for supplying steam, US Patent, Patent No. 6655409 B1, US.

Suh, K.Y., Halimi, B., Kim, K.S., 2010. Linearized power engineering for small modular reactors, The 25th KAIF/KNS Annual Conference, Seoul, Korea.

Tovornik, B., Donlagic, D., Muskinja, N., 1989. Intelligent control valve, CompEuro'89. VLSI and Computer Peripherals: VLSI and Microelectronic Applications in Intelligent Peripherals and their Interconnection Networks, Hamburg, Germany, pp. 3/48-51.

Trinh, T.Q., 2009. Dynamic response of the supercritical CO2 Brayton recompression cycle to various system transients. Massachusetts Institute of Technology.

Turchi, C.S., 2009. Supercritical CO2 for application in concentrating solar power systems, Supercritical CO2 Power Cycle Symposium Troy, NY, US.

Vergara, J.A., McKesson, C.B., 2002. Nuclear propulsion in high-performance cargo vessels. Mar. Technol. 39, pp. 1-11.

Vujić, J., Bergmann, R.M., Škoda, R., Miletić, M., 2012. Small modular reactors: Simpler, safer, cheaper? Energy 45, 288–295.

Wang, Z., Guo, S., 2009. Research on maintenance optimization for steam turbine digital electro-hydraulic control system, Third International Symposium on Intelligent Information Technology Application. IEEE, China, pp. 345-348.

White, F.M., 2003. Fluid Mechanics. 5th. Boston: McGraw-Hill Book Company.

Wong, C.P.C., McQuillan, B.W., Schleicher, R.W., Cheng, E.T., 1995. Evaluation of US DEMO helium-cooled blanket options, 16th IEEE/NPSS Symposium Fusion Engineering. IEEE, San Diego, CA pp. 1145-1150.

Wu, Y., 2008. Conceptual design of the China fusion power plant FDS-II. Fusion Eng. Des. 83, 1683-1689.

Yamaguchi, H., Zhang, X.R., Fujima, K., Enomoto, M., Sawada, N., 2006. Solar energy powered Rankine cycle using supercritical CO2. Appl. Therm. Eng. 26, 2345-2354.

Yoo, Y.H., Suh, K.Y., 2011. Engineering analysis of mass flow rate for turbine system control and design. Nucl. Eng. Des. 241, 4061-4078.

Yoon, H.J., Ahn, Y., Lee, J.I., Addad, Y., 2012. Potential advantages of coupling supercritical CO2 Brayton cycle to water cooled small and medium size reactor. Nucl. Eng. Des. 245, 223-232.

Younger, A.H., 2004. Natural gas processing principles and technology - part I. University of Calgary.

Zaryankin, A.E., Zaryankin, V.A., Simonov, B.P., 2003. Several ways of improving the efficiency of the flow paths for steam turbines. Therm. Eng. 50, 442-448.

Zhang, X.R., Yamaguchi, H., Uneno, D., Fujima, K., Enomoto, M., Sawada, N., 2006. Analysis of a novel solar energy-powered Rankine cycle for combined power and heat generation using supercritical carbon dioxide. Renewable Energy 31, 1839-1854.

Zhao, H., Peterson, P.F., 2008. Multiple reheat helium Brayton cycles for sodium cooled fast reactors. Nucl. Eng. Des. 238, 1535-1546.

Zikanov, O., 2010. Essential computational fluid dynamics. John Wiley & Sons Inc.

# Appendix B: Output of Cycle Code

## B1. Cycle with Stop Valve and Control Valve

B1.1 Properties of each point

| No | Pressure [MPa] | | dP [kPa] | Temperature [K] | | Entropy [J/kg-K] | | Enthalpy [kJ/kg] | |
|---|---|---|---|---|---|---|---|---|---|
| | Input | Output | | Input | Output | Input | Output | Input | Output |
| 1 | 7.45 | 7.41 | 44.73 | 304.77 | 304.77 | 1524 | 1524 | 360 | 360 |
| 2 | 20.00 | 19.96 | 37.93 | 358.30 | 358.24 | 1535 | 1535 | 390 | 390 |
| 3 | 19.96 | 19.95 | 10.88 | 465.68 | 465.65 | 2025 | 2025 | 587 | 587 |
| 4 | 19.96 | 19.95 | 19.24 | 463.38 | 463.34 | 2018 | 2018 | 584 | 584 |
| 5 | 19.94 | 19.91 | 21.50 | 655.54 | 655.46 | 2462 | 2462 | 829 | 829 |
| 6 | 19.71 | 19.69 | 15.16 | 813.15 | 813.09 | 2729 | 2729 | 1023 | 1023 |
| 7 | 19.34 | 19.34 | 3.12 | 810.24 | 810.24 | 2729 | 2729 | 1020 | 1020 |
| 8 | 7.78 | 7.75 | 35.01 | 699.39 | 699.67 | 2742 | 2743 | 898 | 899 |
| 9 | 7.73 | 7.67 | 59.44 | 484.74 | 484.55 | 2326 | 2327 | 654 | 654 |
| 10 | 7.66 | 7.54 | 120.68 | 367.69 | 367.69 | 1999 | 2001 | 515 | 515 |
| 11 | 7.54 | 7.49 | 55.04 | 367.69 | 367.49 | 2004 | 2006 | 516 | 516 |
| 12 | 7.54 | 7.54 | 2.61 | 367.69 | 367.67 | 2004 | 2004 | 516 | 516 |
| 13 | 19.97 | 19.96 | 2.38 | 463.38 | 463.38 | 2018 | 2018 | 584 | 584 |

B1.2 Pressure Drop of Pipe Section

| No. | Section | Pressure Drop [kPa] | No. | Section | Pressure Drop [kPa] |
|---|---|---|---|---|---|
| 1 | 1 | 0.0512 | 8 | 1 | 26.9198 |
| | 2 | 8.9087 | | 2 | 2.9114 |
| | 3 | 0.2062 | | 3 | 4.5847 |
| | 4 | 35.5672 | | 4 | 0.5954 |
| 2 | 1 | 35.9943 | 9 | 1 | 0.4034 |
| | 2 | 0.5041 | | 2 | 3.0054 |
| | 3 | 1.4348 | | 3 | 1.9085 |
| 3 | 1 | 3.0292 | | 4 | 39.8933 |
| | 2 | 0.5711 | | 5 | 1.8638 |
| | 3 | 7.2819 | | 6 | 11.7301 |
| 4 | 1 | 11.6684 | | 7 | 0.6343 |
| | 2 | 1.1541 | 10 | 1 | 0.4127 |
| | 3 | 6.4133 | | 2 | 3.099 |
| 5 | 1 | 0.3882 | | 3 | 1.2126 |
| | 2 | 1.9262 | | 4 | 115.9595 |
| | 3 | 9.8538 | 11 | 1 | 29.1812 |
| | 4 | 0.6786 | | 2 | 0.5772 |
| | 5 | 8.6551 | | 3 | 24.4303 |
| 6 | 1 | 11.2045 | | 4 | 0.8465 |
| | 2 | 0.8786 | 12 | 1 | 2.6111 |
| | 3 | 3.0771 | 13 | 1 | 2.3807 |
| 7 | 1 | 3.121 | | | |

## B2. Cycle with Combined Valve

### B2.1 Properties of each point

| No. | Pressure [MPa] Input | Output | dP [kPa] | Temperature [K] Input | Output | Entropy [J/kg-K] Input | Output | Enthalpy [kJ/kg] Input | Output |
|---|---|---|---|---|---|---|---|---|---|
| 1 | 7.45 | 7.41 | 45.40 | 304.77 | 304.77 | 1524 | 1524 | 360 | 360 |
| 2 | 20.00 | 19.96 | 38.50 | 358.30 | 358.24 | 1535 | 1535 | 390 | 390 |
| 3 | 19.96 | 19.95 | 11.27 | 470.85 | 470.82 | 2040 | 2040 | 595 | 595 |
| 4 | 19.95 | 19.93 | 19.84 | 467.22 | 467.18 | 2030 | 2030 | 590 | 590 |
| 5 | 19.92 | 19.90 | 21.97 | 658.88 | 658.80 | 2468 | 2468 | 833 | 833 |
| 6 | 19.52 | 19.50 | 15.53 | 813.15 | 813.09 | 2731 | 2731 | 1023 | 1023 |
| 7 | 19.32 | 19.32 | 3.18 | 811.58 | 811.58 | 2731 | 2731 | 1021 | 1021 |
| 8 | 7.77 | 7.74 | 35.64 | 700.61 | 700.90 | 2744 | 2745 | 900 | 900 |
| 9 | 7.72 | 7.66 | 60.81 | 487.19 | 487.00 | 2332 | 2333 | 657 | 657 |
| 10 | 7.65 | 7.53 | 121.48 | 365.93 | 365.93 | 1993 | 1995 | 513 | 513 |
| 11 | 7.53 | 7.47 | 55.41 | 365.93 | 365.73 | 1998 | 2000 | 514 | 514 |
| 12 | 7.53 | 7.53 | 2.63 | 365.93 | 365.92 | 1998 | 1998 | 514 | 514 |
| 13 | 19.96 | 19.96 | 2.40 | 461.77 | 461.77 | 2013 | 2013 | 582 | 582 |

B2.2 Pressure Drop of Pipe Section

| No. | Section | Pressure Drop [kPa] | No. | Section | Pressure Drop [kPa] |
|---|---|---|---|---|---|
| 1 | 1 | 0.0519 | 8 | 1 | 27.4035 |
| | 2 | 9.0409 | | 2 | 2.9637 |
| | 3 | 0.2093 | | 3 | 4.667 |
| | 4 | 36.0949 | | 4 | 0.6061 |
| 2 | 1 | 36.5293 | 9 | 1 | 0.4127 |
| | 2 | 0.5116 | | 2 | 3.0745 |
| | 3 | 1.4561 | | 3 | 1.9523 |
| 3 | 1 | 3.1382 | | 4 | 40.8105 |
| | 2 | 0.5916 | | 5 | 1.9066 |
| | 3 | 7.544 | | 6 | 11.9997 |
| 4 | 1 | 12.0377 | | 7 | 0.6489 |
| | 2 | 1.1906 | 10 | 1 | 0.4154 |
| | 3 | 6.6163 | | 2 | 3.1194 |
| 5 | 1 | 0.3967 | | 3 | 1.2206 |
| | 2 | 1.9685 | | 4 | 116.7251 |
| | 3 | 10.0701 | 11 | 1 | 29.3824 |
| | 4 | 0.6935 | | 2 | 0.5812 |
| | 5 | 8.845 | | 3 | 24.5987 |
| 6 | 1 | 11.4771 | | 4 | 0.8523 |
| | 2 | 0.9 | 12 | 1 | 2.6291 |
| | 3 | 3.152 | 13 | 1 | 2.4012 |
| 7 | 1 | 3.1766 | | | |

# Appendix C: Nonlinearity Compensation Code Input

## C1. Valve Data

```
*------------------------------------------------------------------------*
* C972: turbine Stop valve 1
*------------------------------------------------------------------------*
*
9720000 tcval valve
*
*          from         to          A          for.K    rev.K
9720101  970010000  976000000  0.2949      16.910    16.748     000000    *
A=3.1744ft^2
*            mass-l mass-v
9720201 1 0.0      1593.10 0.0
*
9720300 trpvlv
9720301 750
*
*------------------------------------------------------------------------*
* C973: turbine Stop valve 2
*------------------------------------------------------------------------*
*
9730000 tcval valve
*
*          from         to          A          for.K    rev.K
9730101  970010000  977000000  0.2949      16.910    16.748     000000    *
A=3.1744ft^2
*            mass-l mass-v
```

9730201 1 0.0        1593.10 0.0

*

9730300 trpvlv

9730301 750

*

*------------------------------------------------------------------------------*

* C974: turbine Stop valve 3

*------------------------------------------------------------------------------*

*

9740000 tcval valve

*

*          from        to          A          for.K      rev.K

9740101  970010000  978000000  0.2949      16.910    16.748     000000     *

A=3.1744ft^2

*               mass-l mass-v

9740201 1 0.0        1593.10 0.0

*

9740300 trpvlv

9740301 750

*

*------------------------------------------------------------------------------*

* C975: turbine Stop valve 4

*------------------------------------------------------------------------------*

*

9750000 tcval valve

*

*          from        to          A          for.K      rev.K

9750101  970010000  979000000  0.2949      16.910    16.748     000000     *

A=3.1744ft^2

```
*              mass-l mass-v
9750201 1 0.0      1593.10 0.0
*
9750300 trpvlv
9750301 750
*
*-------------------------------------------------------------------------------*
*   976:   ST1 to CV1
*-------------------------------------------------------------------------------*
*
9760000    cv-in    snglvol
9760101    1.1    0.373    0.0    0.0   0.0    0.0    1.18e-6    0.0    00
9760200    2          55.95e5          1.0
*
*-------------------------------------------------------------------------------*
*   977:   ST2 to CV2
*-------------------------------------------------------------------------------*
*
9770000    cv-in    snglvol
9770101    1.1    0.373    0.0    0.0   0.0    0.0    1.18e-6    0.0    00
9770200    2          55.95e5          1.0
*
*-------------------------------------------------------------------------------*
*   978:   ST3 to CV3
*-------------------------------------------------------------------------------*
*
9780000    cv-in    snglvol
9780101    1.1    0.373    0.0    0.0   0.0    0.0    1.18e-6    0.0    00
9780200    2          55.95e5          1.0
```

```
*
*-----------------------------------------------------------------------*
*   979:   ST4 to CV4
*-----------------------------------------------------------------------*
*
9790000    cv-in    snglvol
9790101    1.1    0.373    0.0    0.0    0.0    0.0    1.18e-6    0.0    00
9790200    2           55.95e5           1.0
*
*-----------------------------------------------------------------------*
* C980: turbine Control Valve 1
*-----------------------------------------------------------------------*
9800000 CV1 valve
*         from         to         A         for.K    rev.K
9800101 976010000 984000000 0.2452    16.910    16.748    000000
*             mass-l mass-v
9800201 1 0.0 1593.10 0.0
*
9800300 srvvlv
*         Control_Var_number    Valve_Table_num
9800301 305
*9810400
*Table entries w1       w2        w3
9800401   0.0         0.0         0.0
9800402   0.104       106.0       106.0
9800403   0.164       236.0       236.0
9800404   0.224       376.0       376.0
9800405   0.284       522.0       522.0
9800406   0.344       672.0       672.0
```

9800407   0.404   797.0   797.0

9800408   0.464   885.0   885.0

9800409   0.524   924.0   924.0

9800410   0.584   947.0   947.0

9800411   0.644   962.0   962.0

9800412   0.665   970.0   970.0

9800413   0.782   984.0   984.0

9800414   0.8   986.0   986.0

9800415   0.9   988.0   988.0

9800416   1.0   990.0   990.0

*

*----------------------------------------------------------------------------*

* C981: turbine Control Valve 2

*----------------------------------------------------------------------------*

9810000 CV1 valve

*         from         to         A         for.K     rev.K

9810101 977010000 984000000 0.2452     16.910   16.748    000000

*          mass-l mass-v

9810201 1 0.0 1593.10 0.0

*

9810300 srvvlv

*         Control_Var_number    Valve_Table_num

9810301 312

*9810400

*Table entries w1      w2      w3

9810401   0.0       0.0       0.0

9810402   0.104   106.0   106.0

9810403   0.164   236.0   236.0

9810404   0.224   376.0   376.0

9810405  0.284    522.0    522.0

9810406  0.344    672.0    672.0

9810407  0.404    797.0    797.0

9810408  0.464    885.0    885.0

9810409  0.524    924.0    924.0

9810410  0.584    947.0    947.0

9810411  0.644    962.0    962.0

9810412  0.665    970.0    970.0

9810413  0.782    984.0    984.0

9810414  0.8      986.0    986.0

9810415  0.9      988.30   988.30

9810416  1.0      990.0    990.0

*

*---------------------------------------------------------------------------*

* C982: turbine Control Valve 3

*---------------------------------------------------------------------------*

9820000 CV1 valve

*        from         to         A         for.K     rev.K

9820101 978010000 984000000 0.2452    16.910   16.748   000000

*            mass-l mass-v

9820201 1 0.0 1593.10 0.0

*

9820300 srvvlv

*        Control_Var_number    Valve_Table_num

9820301 322

*9810400

*Table entries w1      w2       w3

9820401  0.0         0.0       0.0

9820402  0.104     106.0     106.0

9820403    0.164    236.0    236.0

9820404    0.224    376.0    376.0

9820405    0.284    522.0    522.0

9820406    0.344    672.0    672.0

9820407    0.404    797.0    797.0

9820408    0.464    885.0    885.0

9820409    0.524    924.0    924.0

9820410    0.584    947.0    947.0

9820411    0.644    962.0    962.0

9820412    0.665    970.0    970.0

9820413    0.782    984.0    984.0

9820414    0.8      986.0    986.0

9820415    0.9      988.30   988.30

9820416    1.0      990.0    990.0

*

*---------------------------------------------------------------------------*

* C983: turbine Control Valve 4

*---------------------------------------------------------------------------*

9830000 CV1 valve

*          from        to          A          for.K      rev.K

9830101 979010000 984000000 0.2452     16.910    16.748    000000

*               mass-l mass-v

9830201 1 0.0 1593.10 0.0

*

9830300 srvvlv

*          Control_Var_number    Valve_Table_num

9830301 332

*9810400

*Table entries w1        w2        w3

```
9830401   0.0         0.0      0.0
9830402   0.104      106.0    106.0
9830403   0.164      236.0    236.0
9830404   0.224      376.0    376.0
9830405   0.284      522.0    522.0
9830406   0.344      672.0    672.0
9830407   0.404      797.0    797.0
9830408   0.464      885.0    885.0
9830409   0.524      924.0    924.0
9830410   0.584      947.0    947.0
9830411   0.644      962.0    962.0
9830412   0.665      970.0    970.0
9830413   0.782      984.0    984.0
9830414   0.8        986.0    986.0
9830415   0.9        988.30   988.30
9830416   1.0        990.0    990.0
```
*------------------------------------------------------------------------------*

## C2. Governor System and Compensator

*------------------------------------------------------------------------------*
* CV300 Control valve system
*------------------------------------------------------------------------------*
20530100 contv constant 1.0
20530200 governor   integral 1.0 0.0 0 3 0.0 2900.0
20530201 cntrlvar 301
*           name        type       scaling     initial     intial value flag
20530300   refer     function    1.0          0.1            0
20530301   cntrlvar   302          050   * general table #50
20530400 erro sum 1.0 0 1 0

20530401 0   1.0 cntrlvar 303 -1.0 cntrlvar 306

20530500 governor   integral 1.0 0.0 0 3 0.0 1.0

20530501 cntrlvar 304

| * | name | type | scaling | initial | intial value flag |
|---|------|------|---------|---------|-------------------|
| 20530600 | refer | function | 1.0 | 0.0 | 0 |

20530601   cntrlvar   305      070   * general table #70

*CV 2

| * | name | type | scaling | initial | intial value flag |
|---|------|------|---------|---------|-------------------|
| 20531000 | refer2 | function | 1.0 | 0.1 | 0 |

20531001   cntrlvar   302      050   * general table #50

20531100 erro2 sum 1.0 0 1 0

20531101 0   1.0 cntrlvar 310 -1.0 cntrlvar 313

20531200 governr2   integral 1.0 0.0 0 3 0.0 1.0

20531201 cntrlvar 311

| * | name | type | scaling | initial | intial value flag |
|---|------|------|---------|---------|-------------------|
| 20531300 | refer | function | 1.0 | 0.0 | 0 |

20531301   cntrlvar   312      070   * general table #70

*CV 3

| * | name | type | scaling | initial | intial value flag |
|---|------|------|---------|---------|-------------------|
| 20532000 | refer3 | function | 1.0 | 0.1 | 0 |

20532001   cntrlvar   302      050   * general table #50

20532100   erro3 sum 1.0 0 1 0

20532101 0   1.0 cntrlvar 320 -1.0 cntrlvar 323

20532200 governr3   integral 1.0 0.0 0 3 0.0 1.0

20532201 cntrlvar 321

| * | name | type | scaling | initial | intial value flag |
|---|------|------|---------|---------|-------------------|
| 20532300 | refer | function | 1.0 | 0.0 | 0 |

20532301   cntrlvar   322      070   * general table #70

*CV 4

```
*          name         type      scaling    initial   intial value flag
20533000   refer4   function   1.0        0.1          0
20533001   cntrlvar   302       050    * general table #50
20533100 erro4 sum 1.0 0 1 0
20533101 0    1.0 cntrlvar 330 -1.0 cntrlvar 333
20533200 governr4    integral 1.0 0.0 0 3 0.0 1.0
20533201 cntrlvar 331
*          name         type      scaling    initial   intial value flag
20533300   refer    function   1.0        0.0          0
20533301   cntrlvar   332       070    * general table #70
*
*------------------------------------------------------------------------*
*------------------------------------------------------------------------*
*     A111.      General      Table      Data      for      Control
*
*------------------------------------------------------------------------*
*
*    genaral table C1: Control for   CV
*
20205000         reac-t
*
*     Time              Value
*      (s)              (pu)
20205001      0.0   0.1000
20205002   2150.0   0.1000
20205003   2162.0   0.1180
20205004   2174.0   0.1360
20205005   2186.0   0.1540
20205006   2198.0   0.1720
```

| | | |
|---|---|---|
| 20205007 | 2210.0 | 0.1900 |
| 20205008 | 2222.0 | 0.2080 |
| 20205009 | 2234.0 | 0.2260 |
| 20205010 | 2246.0 | 0.2440 |
| 20205011 | 2258.0 | 0.2620 |
| 20205012 | 2270.0 | 0.2800 |
| 20205013 | 2282.0 | 0.2980 |
| 20205014 | 2294.0 | 0.3160 |
| 20205015 | 2306.0 | 0.3340 |
| 20205016 | 2318.0 | 0.3520 |
| 20205017 | 2330.0 | 0.3700 |
| 20205018 | 2342.0 | 0.3880 |
| 20205019 | 2354.0 | 0.4060 |
| 20205020 | 2366.0 | 0.4240 |
| 20205021 | 2378.0 | 0.4420 |
| 20205022 | 2390.0 | 0.4600 |
| 20205023 | 2402.0 | 0.4780 |
| 20205024 | 2414.0 | 0.4960 |
| 20205025 | 2426.0 | 0.5140 |
| 20205026 | 2438.0 | 0.5320 |
| 20205027 | 2450.0 | 0.5500 |
| 20205028 | 2462.0 | 0.5680 |
| 20205029 | 2474.0 | 0.5860 |
| 20205030 | 2486.0 | 0.6040 |
| 20205031 | 2498.0 | 0.6220 |
| 20205032 | 2510.0 | 0.6400 |
| 20205033 | 2522.0 | 0.6580 |
| 20205034 | 2534.0 | 0.6760 |
| 20205035 | 2546.0 | 0.6940 |

20205036    2558.0    0.7120
20205037    2570.0    0.7300
20205038    2582.0    0.7480
20205039    2594.0    0.7660
20205040    2606.0    0.7840
20205041    2618.0    0.8020
20205042    2630.0    0.8200
20205043    2642.0    0.8380
20205044    2654.0    0.8560
20205045    2666.0    0.8740
20205046    2678.0    0.8920
20205047    2690.0    0.9100
20205048    2702.0    0.9280
20205049    2714.0    0.9460
20205050    2726.0    0.9640
20205051    2738.0    0.9820
20205052    2750.0    1.0000
20205053    2900.0    1.0000


*---------------------------------------------------------------------------*
*    genaral table C1: Nonlinearity Compensator
*---------------------------------------------------------------------------*
20207000          reac-t
*
*      Time              Value
*       (s)              (pu)
*
20207001    0.0      0.0
20207002    0.104    0.1076

```
20207003  0.164  0.2386
20207004  0.224  0.3801
20207005  0.284  0.5279
20207006  0.344  0.6786
20207007  0.404  0.8055
20207008  0.464  0.8937
20207009  0.524  0.9336
20207010  0.584  0.9566
20207011  0.644  0.9720
20207012  0.665  0.9798
20207013  0.782  0.9943
20207014  0.800  0.9960
20207015  0.900  0.9980
20207016  1.000  1.0000
20207017  2.000  1.0000
*
*---------------------------------------------------------------------------*
```

# Publication List

## Journal Paper

1. Halimi, B., Kim, S.H., Suh, K.Y., 2013. Engineering of combined valve flow for power conversion system. Energy Convers. Manage. 65, 448-455.

2. Halimi, B., Suh, K.Y., 2012. Computational analysis of supercritical $CO_2$ Brayton cycle power conversion system for fusion reactor. Energy Convers. Manage. 63, 38-43.

3. Halimi, B., Suh, K.Y., 2012. Engineering nonlinearity characteristic compensation for commercial steam turbine control valve using linked MARS code and Matlab Simulink. Nucl. Eng. Des. 243, 360-370.

## International Conference Paper

1. B. Halimi, K.Y. Suh, 2012. Programmable ac power supply for simulating power transient expected in fusion reactor. International Congress on Advances in Nuclear Power Plants (ICAPP), Chicago, IL, US, June 24-28.

2. B. Halimi, K.Y. Suh, 2012. Computational analysis of controlled power source for fusion reactor decay heat power experimental application. 18th Pacific Basin Nuclear Conference (PBNC), Busan, Korea, March 18-23.

3. B. Halimi, S.H. Kim, K.Y. Suh, 2012. Flow coefficient of combined valve with supercritical $CO_2$ flow. 8th KSME-JSME Thermal and Fluids Engineering Conference (TFEC), Incheon, Korea, March 18-21.

4. B. Halimi, S.H. Nam, K.Y. Suh, 2011. Engineering of nuclear thermal propulsion system for space application. American Nuclear Society Winter

Meeting, Washington, DC, US, October 30-November 3.

5.  B. Halimi, K.Y. Suh, 2011. Engineering of nuclear electric propulsion system for marine application. American Nuclear Society Winter Meeting, Washington, DC, US, October 30-November 3.

6.  H.M. Son, B. Halimi, K.Y. Suh, 2011. Quick design method for lead cooled battery-reactor BORIS. ASME 2011 Small Modular Reactors Symposium, Washington, DC, US, September 28-30.

7.  B. Halimi, K.Y. Suh, 2011. Computational analysis of supercritical $CO_2$ Brayton cycle power conversion system for fusion reactor. $10^{th}$ International Conference on Sustainable Energy Technologies, Istanbul, Turkey, September 4-7.

8.  B. Halimi, S.H. Kim, K.Y. Suh, 2011. Computational analysis of combined valve for steam turbine system control. $8^{th}$ International Conference on Heat Transfer, Fluid Mechanics and Thermodynamics (HEFAT), Pointe Aux Piments, Mauritius, July 11-13.

9.  B. Halimi, S.H. Kim, K.Y. Suh, 2011. Engineering of combined valve mass flow rate for steam turbine system. American Nuclear Society Annual Meeting, Hollywood, FL, US, June 26-30.

10. B. Halimi, K.Y. Suh, 2011. Engineering of nuclear electric propulsion system. $19^{th}$ International Conference on Nuclear Engineering (ICONE), Chiba, Japan, May 16-19.

11. B. Halimi, K.Y. Suh, 2011. Modeling of artificial stiction in steam turbine control valve. International Congress on Advances in Nuclear Power Plants (ICAPP), Nice, France, May 2-5.

12. B. Halimi, K.Y. Suh, 2010. Computational analysis of steam turbine control valve stiction on power system dynamic stability. 7th Japan-Korea Symposium on Nuclear Thermal Hydraulics and Safety (NTHAS), Chuncheon, Korea, November 14 – 17.

13. B. Halimi, S. H. Kim, A. Pirouzmand, K.Y. Suh, 2010. Engineering design of combined valve for supercritical $CO_2$ Brayton ccle fusion reactor power conversion system. 19th Topical Meeting on the Technology of Fusion Energy, Las Vegas, NV, US, November 7-11.

14. A. Pirouzmand, B. Halimi, K.Y. Suh, 2010. Engineering of control valve mass flow rate in steam turbine system. 7th International Conference on Flow Dynamics (ICFD), Sendai, Japan, November 1-3.

15. B. Halimi, A. Pirouzmand, K.Y. Suh, 2010. Engineering of nolinearity characteristic compensation for turbine control valve. 7th International Conference on Flow Dynamics (ICFD), Sendai, Japan, November 1-3.

16. B. Halimi, K.Y. Suh, 2010. Control engineering of steam turbine valve. 8th International Topical Meeting on Nuclear Reactor Thermal Hydraulics, Operation and Safety (NUTHOS), Shanghai, China, October 10-14.

17. B. Halimi, K.Y. Suh, 2010. Engineering design of supercritical Brayton cycle. 8th International Topical Meeting on Nuclear Reactor Thermal Hydraulics, Operation and Safety (NUTHOS), Shanghai, China, October 10-14.

18. B. Halimi, K.Y. Suh, 2010. Dynamic control of nuclear electric propulsion system. 8th International Topical Meeting on Nuclear Reactor Thermal Hydraulics, Operation and Safety (NUTHOS), Shanghai, China, October 10-14.

19. B. Halimi, K.Y. Suh, 2010. Analysis of nonlinearities compensation for control valves. International Congress on Advances in Nuclear Power Plants (ICAPP),

San Diego, CA, US, June 13-17.

20. K.Y. Suh, B. Halimi, K.S. Kim, 2010. Linearized Power Engineering for Small Modular Reactors. 25th KAIF/KNS Annual Conference, Seoul, Korea, April 14-16.

21. B. Halimi, K.Y. Suh, 2009. Filter Computation for Nuclear Power Plant Failure Detection. American Nuclear Society Winter Meeting, Washington, DC, US, November 15-19.

22. B. Halimi, K.Y. Suh, 2008. A concept of instrumentation failure detection for nuclear power plant monitoring system. 16th Pacific Basin Nuclear Conference (PBNC), Aomori, Japan, October 13-18.

23. B. Halimi, Kune Y. Suh, 2008. Application of nonlinear filter to failure detection in nuclear power plant instrumentation. 7th International Topical Meeting on Nuclear Reactor Thermal Hydraulics, Operation and Safety (NUTHOS), Seoul, Korea, October 5-9.

24. B. Halimi, K.Y. Suh, 2008. A concept of failure detection in nuclear power plant instrumentation. 16th International Conference on Nuclear Engineering (ICONE), Orlando, FL, US, May 11-15.

25. N.H. Kim, B. Halimi, K.Y. Suh, 2007. Conceptual Design of Naval Application Vessel Integral System. American Nuclear Society Winter Meeting, Washington, DC, US, November 11-15.

## Domestic Conference Paper

1. B. Halimi, H.M. Son, K.Y. Suh, 2012. Power monitoring for transient supercritical power conversion system experiment. Korean Nuclear Society Spring Meeting, Jeju, Korea, May 17-18.

2. B. Halimi, K.Y. Suh, 2011. Computational analysis of controlled power source for transient fusion reactor power conversion. Korean Nuclear Society Autumn Meeting, Gyeongju, Korea, October 27-28.

3. B. Halimi, Sang G. Park, K.Y. Suh, 2011. Control engineering of controlled power supply for transient condition experiment. Korean Nuclear Society Spring Meeting, Taebaek, Korea, May 26-27.

4. B. Halimi, K.Y. Suh, 2010. Steam turbine control valve stiction effect on power system stability. Korean Nuclear Society Autumn Meeting, Jeju, Korea, October 21-22.

5. B. Halimi, K.Y. Suh, 2010. Compensation of control valves nonlinearities in flow control systems. Korean Nuclear Society Spring Meeting, Pyeongchang, Korea, May 27-28.

6. B. Halimi, K.Y. Suh, 2009. Extended Kalman filter computation for nuclear power plant failure detection. Korean Nuclear Society Autumn Meeting, Gyeongju, Korea, October 29-30.

7. B. Halimi, K.Y. Suh, 2009. Modeling of nuclear electric propulsion system for naval application. Korean Nuclear Society Autumn Meeting, Gyeongju, Korea, October 29-30.

8. B. Halimi, K.Y. Suh, 2009. Conceptual design of electrical propulsion system for nuclear operated vessel adventure. Korean Nuclear Society Spring Meeting,

Jeju, Korea, May 22.

9.  B. Halimi, K.Y. Suh, 2008. A concept of instrumentation failure detection for nuclear power plant. Korean Nuclear Society Autumn Meeting, Pyeongchang, Korea, October 30-31.

10. B. Halimi, T.W. Kim, H.M. Son, K.Y. Suh, 2008. Design concept of propulsion system for nuclear operated vessel adventurer. Korean Nuclear Society Spring Meeting, Gyeongju, Korea, May 29-30.